Feature-based Modeling for Industrial Processes in the Context of Digital Twins

by

Jiangzhuo Ren

A thesis submitted in partial fulfillment of the requirements for the degree of

Doctor of Philosophy

Department of Mechanical Engineering

University of Alberta

Abstract

Industrial process modeling is currently undergoing a fundamental transformation, leading towards interconnected closed-loop twins of models, i.e., the parametrically-controlled real-world physics model, and its corresponding digitalized virtual system model. However, with the application of advanced manufacturing technologies to industrial processes, the digitalized modeling of the physics phenomena becomes the obstruction to realizing this transformation. Thus, this research proposes a semantic conceptual framework for industrial process modeling in the context of digital twins. Based on a hierarchical structure of digital twins, this framework modularizes the modeling process in terms of the semantic information modules of physics in the real-world phenomena and clarifies inter-module associations and near-real-time data processing so that the time-sensitive phenomenon information objects distributed on virtually-separated sub-level physics models can be supported for representing the real-world process comprehensively. Advanced feature concept is adopted to construct the digital models as the basic compositions of any virtual industrial process. The related feature definitions are extended in this work so that the common characteristics in the concept of digital twins could be generically and concisely represented.

The high-velocity oxygen-fuel (HVOF) thermal spraying process is used as an example to demonstrate the modeling methods in the framework. Firstly, the partial feature concepts are implemented to develop a core multiple-view and yet integrated model template covering numerical modeling, numerical analysis, and parameter optimization, where the simulation intent can be associated with the optimization intent. This template models the physicochemical phenomena existing in the HVOF nozzle. Further, the WC-12Co coating properties are optimized. The final experimental verification indicates the proposed framework can generate positive effects on the real world. Secondly, a parametrically controlled model for simulating the coating thickness in HVOF processes is developed based on a hierarchically multiple-model integration method. The effects of the commonly used operating parameters, particle properties and size range, and spray path on the coating thickness distribution are taken into account, which shows excellent comprehensiveness. Meanwhile, the comparison between the experiment results and simulation results indicates that the modeling method can properly mirror the real scenario on the virtual side and predict the coating distribution with a small error. Thirdly, the digital model of a prototyped HVOF coating process system has been constructed to validate the phenomenon synchronization. The data from the nozzle trajectory, the flame and the in-flight particle behavior, and the transient thermal performance of the coating layer and substrate are synchronously incorporated for simulating the transient phenomena of the substrate component temperature and coating thickness distribution on the substrate surface. The final simulation result validates that the feature-based digital model is able to timely reflect the real-world scenario on the virtual side.

Preface

This thesis is an original work by Jiangzhuo Ren, and the research is performed under the supervision of Dr. Yongsheng Ma and Dr. Rafiq Ahmad. Some parts of this thesis have been published by or submitted to the journals listed below:

1. J. Ren, T. Zhou, Y. Rong, Y. Ma, and R. Ahmad (2022) "Feature-based modeling for industrial processes in the context of digital twins: A case study of HVOF process", *Advanced Engineering Informatics* 51:101486. (Chapter 3 and Chapter 6). (I was responsible for conceptualization, literature review, model construction, and writing of the original manuscript; T. Zhou assisted with coding and model construction; Y. Rong was responsible for research sources; Y. Ma and R. Ahmad were the principal investigators and supervisors on this research)
2. J. Ren, G. Zhang, Y. Rong, Y. Ma (2021) "A feature-based model for optimizing HVOF process by combining numerical simulation with experimental verification", *Journal of Manufacturing Processes* 64:224-238. (Chapter 4) (I was responsible for the conceptualization, literature review, model construction, and writing of the original manuscript; G. Zhang assisted with the experimental work; Y. Rong was responsible for research sources; Y. Ma was the principal investigator and supervisor on this research.)
3. J. Ren, R. Ahmad, G. Zhang, Y. Rong, Y. Ma (2021) "A Parametric simulation model for HVOF coating thickness control", *The International Journal of Advanced Manufacturing Technology* 116:293-314. (Chapter 5) (I was responsible for the conceptualization, literature review, model construction, and writing of the original manuscript; R. Ahmad supervised this research; G. Zhang assisted with the experimental work; Y. Rong was responsible for research sources; Y. Ma was the principal investigator and supervisor on the research.)

4. J. Ren and Y. Ma (2020) “A feature-based physical-geometric model for dynamic effect in HVOF thermal spray process”, *Computer-Aided Design & Applications* 17(3):561-574. (Chapter 6) (I was responsible for the conceptualization, literature review, model construction, and writing of the original manuscript; Y. Ma was the principal investigator and supervisor on the research.)

5. J. Ren, Y. Rong, Y. Ma (2021) “Comparison of the renormalization group and the realizable k-ε turbulence models for dynamic performance of HVOF process with a coupled two-stage CAE method”, *Computer-Aided Design & Applications* 18(1):117-129. (Chapter 6) (I was responsible for the conceptualization, literature review, model construction, and writing of the original manuscript; Y. Rong was responsible for research sources; Y. Ma was the principal investigator and supervisor on the research.)

Acknowledgments

First, I would sincerely thank my supervisor, Dr. Yongsheng Ma, and my co-supervisor, Dr. Rafiq Ahmad, for their valuable guidance, unconditional support, and ongoing encouragement. Without their help, this work would not be possible. Also, I would like to thank my supervisory committee member, Dr. Andrew Martin, for his advice, expertise, and support.

I would like to express my gratitude to China Scholarship Council (CSC 201808180001) and NSERC (RGPIN 5641 Ma and RGPIN-2020-03956) for their financial support.

My thanks also go to my colleagues from Dr. Ma's group and the LIMDA lab, who contribute to a friendly research environment. They are more than colleagues; they are friends and families.

Last but not least, I appreciate the support from my parents. Without their encouragement, I would not complete this journey.

Table of Contents

List of Tables

List of Figures

List of Abbreviations

DT	Digital Twin
HVOF	High-velocity Oxygen-fuel thermal spraying
CAD	Computer-aided Design
CAE	Computer-aided Engineering
FEA	Finite Element Analysis
CFD	Computational Fluid Dynamics
MBD	Multibody Dynamics
AI	Artificial Intelligence
DTI	Digital Twin Instance
DTC	Digital Twin Class
FDM	Feature-based Digital Model
DOE	Design of Experiment
RBF	Radial Basis Function
RSM	Response Surface Method
CCD	Central Composite Design
ANOVA	Analysis of Variance
MAE	Absolute Error

RMSE	Root Mean Squared Error
CCC	Circumscribed Central Composition Design
SEM	Scanning Electron Microscope
CMD	Count Mean Diameter
SLPM	Standard Liter per Minute
NRMSE	Normalized Root-mean-square Error
RNG	Renormalization Group

Chapter 1: Introduction

1.1 Background

1.1.1 Digital Twins in Industry

An increasing level of interest in research has been on *digital twins* (DTs) of industrial processes within a reality background of the digital industry over the recent years. Digital twins of industrial processes refer to two mutually synchronized and coexisted information models, one controls real-time industrial processes with interactional data transmissions and on-site data analysis while the other model carries out model-based simulation and optimization, and creates intelligence to provide timely and useful feedback to the real-world process, so that these two collaborative models can generate positive impacts on all aspects of an ideal state of the industry [1–3].

So far, the research works related to DT technologies can be divided into two domains, the conceptual and the realization ones. The conceptual domain displays the futuristic goal of the framework, which requires technical and communal advancements to reach reality or is not easily achievable at present [4]. So, in this domain, emerging technologies are used to construct different frameworks for a futuristic industry, while the difficulties of applying the current industrial processes into the conceptual frameworks are largely ignored.

In contrast, the realization domain research works are generally based on the capabilities of existing tools as the common goal is to deliver promising benefits in the industry as soon as possible. For example, in the manufacturing sector of the past decades, many computer-aided tools have been developed from a specifically-restricted control code to a sophisticated platform, these available tools form the foundations for the realization domain. However, with the higher data sharing and collaboration requirements within the current rapidly-evolving digital ecosystem, their applications in the networked manufacturing process control and simulation are more and more challenging.

1.1.2 Industrial HVOF Thermal Spray Process

High-velocity oxygen-fuel (HVOF) deposition is a thermal spraying technology used to protect or improve the surface performance of workpiece substrate [5]. It is a complex physicochemical process [6]. As shown on the left side of Figure 1.1, during the process, the thoroughly mixed fuel-oxygen gases (typically hydrocarbon and oxygen) and micro particles are fed into the gun chamber, where a combustion reaction takes place, which, in turn, generates a hot sonic or supersonic multiphase gas stream. Within the stream, micro particles of metals, alloys, and/or ceramics are accelerated, heated, and ultimately deposited onto a substrate at high speeds to form a functional coating layer [7]. Due to the complicated phenomena, it is a non-trivial task to develop a digital model for representing the real-world process comprehensively, especially mirroring the real-world physicochemical phenomena on the virtual side. In the contemporary manufacturing industry, with the increasing demand for accurate coatings on component surfaces, robots or handling systems have been utilized to control the movement of the spray torch relative to the surfaces as depicted on the right side of Figure 1.1, which increases the difficulty.

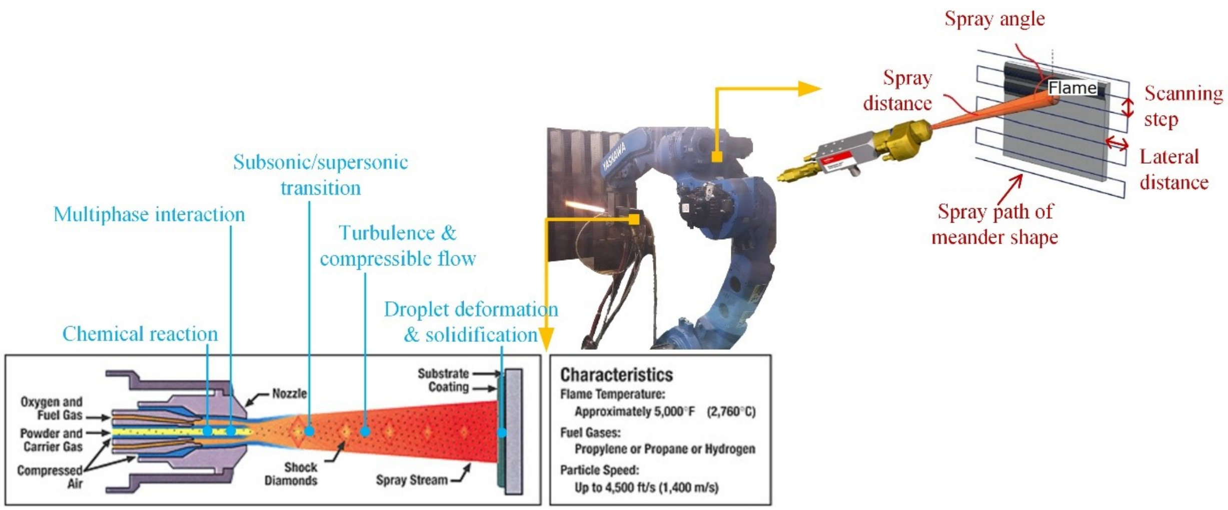

Figure 1.1 Industrial HVOF thermal spray process

1.2 Problem Statement

In the aspect of the conceptual domain of DTs, the major problems involved in this research are:

- The concept of DTs has been mature. However, there are still numerous challenges to implementing the concept in the industry. To the author's best knowledge, there has been published work on a systematic method of leveraging existing tools for realizing or partially realizing the concept.
- Generally, the previous studies about the framework or structure of DTs concerned the domains of DTs, requisite components, and technologies involved. To date, no consensus has been reached regarding a DT framework concerning the near real-time physics phenomenon and their control in industrial processes.

In the context of DTs, the challenges for utilizing the traditional modeling tools are:

- In real industrial processes, data formats differ from machine to machine, and the characteristic data structure from material to material; such situations force the repetitive modeling steps to generalize their solutions.
- The traditional model integration process does not pay special attention to the synchronization of phenomenon semantics, which makes real-virtual mirroring difficult.

1.3 Research Objectives

The objectives of this research are outlined as follow:

- **O1:** Develop a semantic conceptual framework for industrial process modeling in terms of the semantic information modules of physics in real-world phenomena.
- **O2:** Apply advanced feature technology in this framework and extend related feature definitions to represent the common characteristics generically and concisely in the concept of DTs.
- **O3:** Develop and prototype a method of constructing a digital counterpart (a series of digital models) of an HVOF coating process system for the sake of validation.
- **O4:** Achieve informed modeling validation, real-situation monitoring, and guided interactions for an HVOF coating system.

1.4 Research Methodology

To achieve the realization of the proposed framework, this research adopts the methodologies, advanced feature technology [8], computer-aided engineering [9], and multiple-response surface method [10].

- In the previous research works, *advanced feature technology* was widely used in product modeling to capture interdisciplinary entities as well as association relationships between different stages or domains of the whole product lifecycle [8]. In my research, it aims to develop a standardized model template that can guide the modeling process to cater to the trend of DTs in the industry by clarifying the model elements and organizing their functional relationships such that they are dependent, associated, and aggregated. Further, a multiple-view and closed-loop mechanism is constructed by using these elements and relationships.
- *Computer-aided engineering (CAE)* refers to the techniques of using computers and information technology to simulate the performance of a product in order to improve the design or facilitate engineering problems for various industries [11]. It mainly includes finite element analysis (FEA) [12], computational fluid dynamics (CFD) [13], multibody dynamics (MBD) [14], durability and optimization [15]. In this research, CAE works to understand complicated physics phenomena involved industrial processes on the virtual side with offline or online data processing.
- *Response surface method (RSM)* is a collection of mathematical and statistical techniques useful for the modeling and analysis of problems in which a response of interest is influenced by several variables and the objective is to optimize the response [10]. *Multiple-response surface method (MRS)* solves problems involved the analysis of several responses [10]. In the application of the proposed modeling method, multi-objective optimization was carried out by using MRS with desirability functions [10] under a feature-based environment for improving HVOF coating properties.

1.5 Thesis Outline

Chapter 1 provides the background of DTs in industry and industrial HVOF thermal spraying. The motivations of this research are summarized from the challenges from the implementation of existing simulation tools in the concept of DTs. A brief statement on the objectives of this research and the main methodologies used are also presented at the end of this chapter.

Chapter 2 is a general state of the art summary on the main topics covered in this thesis, including industrial process modeling in the view of DTs, advanced feature technology, and industrial HVOF process modeling.

Chapter 3 presents the proposed conceptual framework of feature-based modeling in a digital ecosystem. This chapter mainly introduces the proposed concepts in this thesis and the ideal collaborative environment. The realized functions in the proposed framework, multiple-view integration and closed-loop optimization, inter-module associations and intelligent physics solvers, and synchronization of physics phenomena, are separately introduced and validated by an industrial HVOF process in the subsequent chapters.

In Chapter 4, a core multiple-view and yet integrated model under the feature-based environment, covering numerical modeling, numerical analysis, and parameter optimization, is elucidated, where the simulation intent can be associated with the optimization intent. A prototype environment was developed to model the HVOF system configurations, working conditions, and then derive optimal process parameters. To validate the modeling method, an actual HVOF spray system depositing WC-12Co coating was modeled. The optimal process parameters generated by the model were implemented in the HVOF coating system and its coating properties were tested experimentally to verify the capacity of generating positive impacts on the real physics behavior.

Chapter 5 explains inter-module data processing so that the phenomenon information objects distributed on virtually separated sub-level physics models can be integrated for representing the real process comprehensively. In the validation part, a parametric simulation of the coating thickness in HVOF processes was constructed via the integration of a static in-flight behavior model, a rule-based coating growth model, and a predefined nozzle path. At the end of this chapter, to verify the developed model's effectiveness, four sets of operating parameters with a single straight path were experimentally implemented. The width and height of the bead-like shape coating were in good agreement with the simulated results. The normalized root-mean-square errors of the cross-section profile heights were around 10%.

Chapter 6 describes the capacity of synchronization of physics phenomena proposed in the framework. The feature concept for realizing this capacity, user-defined boundary condition, is validated by using HVOF processes. A digital model of an HVOF coating process system was constructed as the case study. The data from the nozzle trajectory, the flame and the in-flight particle behavior, and the transient thermal performance of the coating layer and substrate were synchronously incorporated for simulating the transient phenomena of the substrate component temperature and coating thickness distribution on the substrate surface. The final simulation result validates that the feature-based digital model is able to comprehensively reflect the real-world scenario on the virtual side, and it can also provide meaningful feedback to the real-world control.

Finally, Chapter 7 summarizes the work done in this thesis. The limitations and future works are also discussed.

Chapter 2: State of the Art

To lead the course of this research towards the objectives identified in the last chapter, this chapter reviews previous research works of three areas, industrial process modeling in the view of DTs (Section 2.1) for the objective of the proposed framework construction, feature technology (Section 2.2) for the information management in the framework, and industrial HVOF process modeling (Section 2.3) for the validation of the proposed ideas. The review of industrial process modeling in the view of DTs starts from the existing concepts and frameworks of DTs, and then looks into some examples of the DT models in the industry. The review of feature technology briefly gives feature modeling historical evolution first. Subsequently, feature interoperability and information consistency are discussed. As an industrial HVOF coating process is used as an example for validating the feature concepts and partial functions (especially process optimization) in the proposed framework, Section 2.3 reviews industrial HVOF processes from the aspect of process optimization firstly. The necessity of developing digital models for this process is also discussed by comparing different optimization strategies. Further, the numerical modeling of the flame and in-flight particle behavior and dynamic coating performance is reviewed. In this research, these models work as the foundations in the developed digital models for understanding the physics phenomena involved.

2.1 Industrial Process Modeling in the view of Digital Twins

2.1.1 Evolution of Digital Twins

DTs originate from the concept of using “twins”. It could date back to NASA’s Apollo program (National Aeronautics and Space Administration), where at least two identical space vehicles were built to allow mirroring the conditions of the space vehicle during the mission. The “twin” working on earth was used extensively for training during flight preparation and simulation for analysis during flight missions [16]. The first appearance of the DT was given by Grieves in his course on "product lifecycle management" in 2003 [17]. However, due to the technological limitations during its early development, the significance of DTs was underestimated. The first journal paper about how DTs worked for the aircraft structural life was published in 2011 [18]. In 2012, the definition of DTs was formalized by NASA. DTs have experienced exponential growth since then. Later, in 2014, the first white paper was published, which reflected the growth of DTs from one conceptual idea to numerous practical applications [17]. With more concerns on DTs, the concept was extended to many different industries beyond the aerospace industry. More recently, as could computing, big data, Internet of Things (IoT), and sensor technologies grew rapidly, the concept of DTs was further completed to leverage these emerging technologies [19]. Considering the current momentum, some researchers believed that the DT research would keep on the rapid growth in the next few years [2].

When the DT concept first appeared on Grieves's course in 2003, its preliminary form only contained three parts: physical product, virtual product, and their connections [17]. These became the basis for the following development. In 2021, this concept was revisited by NASA, which defined a DT as a multiphysics, multiscale, probabilistic, ultra-fidelity simulation that reflects the state of a corresponding twin based on the historical data, real-time sensor data, and the physical model in a timely manner [20]. With the extension of the concept to different areas, the meaning of DTs was more concrete, bringing some special notions such as the airframe DT and experimental DT [21,22]. For example, in the experimental DT, a DT should focus on simulation containing models of its data (the geometrical model of a part, the material of a part, …), its functionality (motion analysis, structural analysis, …), and its communication interfaces [22,23].

On the basis of the early efforts, Tao et al. [19] gave a more complete concept, as shown in Figure 2.1, including five dimensions: physical part, virtual part, connection, data, and service. In their definition, DTs referred to evolved models with high fidelity, continuous interactions between physical and virtual spaces and fused data converging those two spaces.

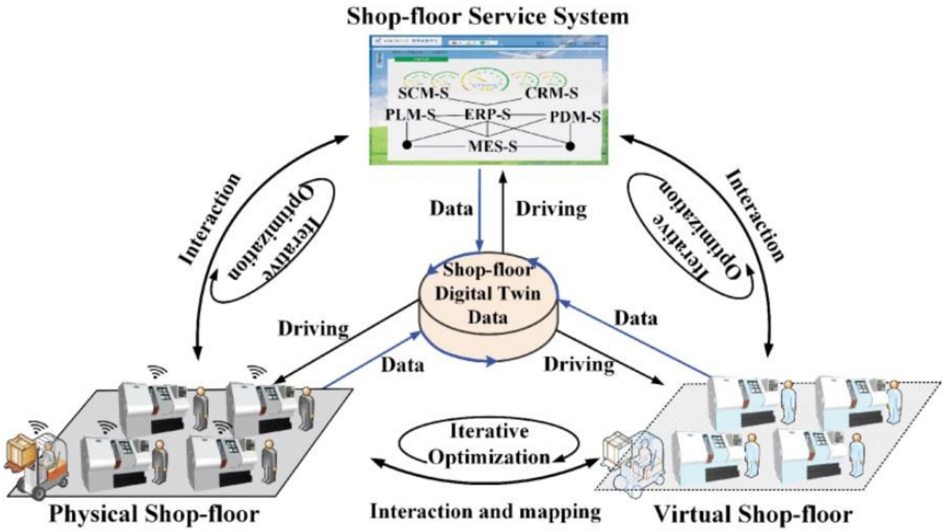

Figure 2.1 Conceptual model of DTs [19,24].

2.1.2 Existing Frameworks of Digital Twins

Much research about the framework of DTs focused on two main objectives. One is the identification of the requisite components and technologies requested by DTs and mutual supports among these elements. For example, at the infancy of DTs, a preliminary framework of DTs only contained three parts: physical product, virtual product, and the connections [17]. Gabor et al. [25] proposed that the main part of DTs was a special simulation with other assisted elements, such as expert knowledge and real data. With the concept's extension, Tao et al. [26,27] presented enabling technologies for a fully functional DT, as shown in Figure 2.2, and emphasized that DTs were the concept relevant to the entire product lifecycle, covering the characteristics, behaviors and performance in the course of manufacturing, use, Maintenance, Repair & Overhaul (MRO), disposal, and other operations of the physical entities, as well as, their corresponding mirror images and mapping in the virtual space. Based on the earlier literature, Autiosalo and his colleagues [4] identified the common characteristics of DTs, e.g. identifier, coupling, computation, artificial intelligence (AI), virtual reality (VR) and so on. They demonstrated the roles of these characteristics in DTs and correlations between them. For example, VR is a branch of computer graphics. It makes the user immersed in a responsive virtual world, which provides an effective interaction between the virtual space and physical space. Besides, they proposed two different data connections, a grid-style structure for a DT with a small number of features, and a star-style structure for a DT with a great number of features.

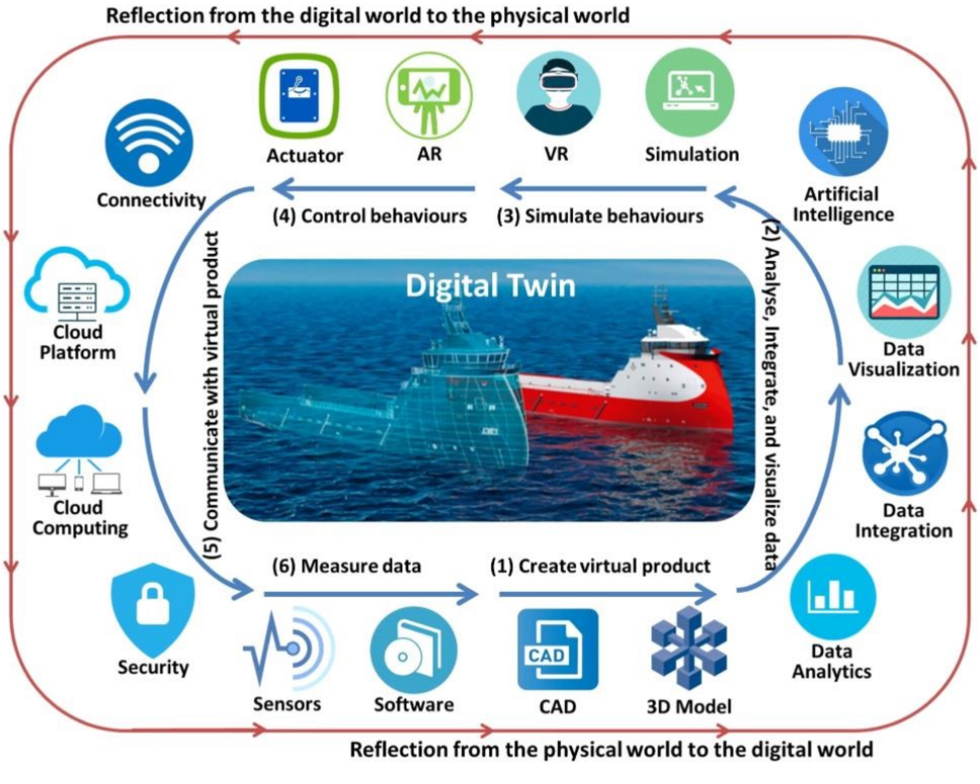

Figure 2.2 Enabling technology of DTs [26].

Another is the structure for applying the DT concept. Schroeder et al. [28] developed a DT modeling architecture including five layers, device layer, user interface layer, web service layer, query layer, and data repository layer. Erkoyuncu et al. [29] developed a DT design framework that uses ontologies to enable co-evolution with complex engineering systems by capturing data in terms of variety, velocity, and volume across the asset life-cycle. Schluse et al. [23] provided a general structure that combines DTs with model-based systems engineering (MBSE) and simulation technology for a variety of different applications from development over optimization, verification, user interfaces, and training, up to the realization of intelligent systems.

Generally, the previous studies about the framework or structure of DTs concerned the domains of DTs, requisite components, and technologies involved. To date, no consensus has been reached regarding the physics phenomenon modeling in a DT framework, e.g., heat transfer, solidification, residual stress, and so on.

2.1.3 Realization of Digital Twins in Industry

Looking into the application level, Schroeder et al. [30] used AutomationML to develop a DT of an industrial valve. This DT concentrated on the operation monitoring of the industrial valve via data acquisition. Moreno et al. [31] constructed a DT for a sheet metal punching machine with the consideration of movements, machining operations, and connectivity with robotic arms. Tao et al. [26] collected data from the entire bicycle lifecycle and then constructed the virtual counterpart via the collection to form a DT for the bicycle. Their application work concentrated on using big data and the constructed DT to redesign the bicycle. In summary, these works primarily focused on data fusion, interaction and collaboration, and service.

Regarding the field concerned in my research, DTs of physics phenomena, their applications were relatively limited. At the early stage of this concept, Tuegel et al. [18] proposed a conceptual model of how the DT could be used for predicting the life of aircraft structure. They first presented that each type of physics should have a separate model. These models can be computational fluid dynamics (CFD) models, structural dynamics models (SDM), thermodynamic models, and other material state evolution models. With the DT concept, these models would be integrated into a single unified model where the physics involved would be seamlessly linked. Iglesias and his colleagues [32] used three complementary simulation tools and experimental measurements to establish a DT application of a JET divertor. An overall workflow scheme for their integration was depicted in their publication. They highlighted that the integration of tools tackling different specific phases is important to provide the needed functionality of a model. Soderberg et al. [33] proposed a DT setup method for increased quality of welded components, which comprehensively includes information model, the welding simulation, the selective assembly and virtual matching. Hierarchical information flows down was developed to represent the way how the top product characteristics affect the subsequent variations. They emphasized the importance of variation propagation in a DT. Built on previous models of 3D printing machines, DebRoy et al. [34] developed DTs of 3D printing machines containing major physics phenomena involved in 3D printing. They provided a perspective of the current status and research needs for the main building blocks of a first-generation DT of AM from the viewpoints of researchers from several organizations. From the relevant applications for physics phenomena, several points can be summarized as follows: (1) a virtual model toward a digital-twin environment needs integration of different sub-level models with synchronized phases or phenomena [32–34]; (2) currently most applications of DTs involved physics phenomena were built on traditional models and assisted by

IoT, experimental measurement, artificial intelligence, and radio frequency identification (RFID) [32–35]; (3) the virtual models tend to be flexible, automatic, and intelligent to derive solutions for the real system [13,36,37].

Hence, the conceptual framework proposed in my research pays special attention to the DT modeling of the physics phenomena in an industrial process through adopting existing CAE tools. It describes an industrial process on the virtual side from the perspective of involved physics phenomena.

2.2 Feature-based Modeling

2.2.1 Evolution of Feature Definitions

Features have been developed for more than 40 years. In the traditional paradigm, features were only at a low level of geometrical shapes. Soon the initial geometrical level of features was associated with other types of engineering information. More recently, in objected-oriented programming, a feature was represented as a class with some attributes [38]. With the 40-year development, in general, they are viewed as modeling elements in CAx systems and used as representations of quantitative and qualitative data related to engineering intents. Shah and Mäntylä [38] gave a general description of features. They read features from two perspectives, on the one side as an "information cluster" for the integrated representation of engineering data, on the other side as "a physical constituent of a part".

So far, features have developed into a series of heterogeneous definitions according to their different applications and engineering intents, mainly including form feature, functional feature, CAE feature, and assembly feature [8]. They are briefly explored as follows.

In the infancy of feature technology, *form features* were geometric specifications according to repetitive shapes used for product development like hole, slot, pocket, boss, and chamfer [39]. These geometric entities were usually simple, primitive, or atomic geometries that could not be decomposed into any other smaller units [40]. In the early stage of product modeling, a major goal of these features was to continuously use repetitive modeling steps of components via describing similar geometric entities in a standard way [41].

With the development of concurrent engineering, purely geometric information could not satisfy the requirements of product designs. Therefore, *functional features* were developed and used in product designs to link different levels of product or system design. However, there are some different understandings about the function description subject to application scenarios. In design research specifically, it is widely accepted that a function is a relationship between input and output of energy, material, and information [42]. Schulte et al. [43] argued that if function information is embedded throughout the design process, it would be more valuable for design engineers. They believed that the functional features should be “a set of functional faces, which embody the active surface of a physical effect to meet the requirements of a certain design (sub-) function”. The main purpose of functional features is to keep on expressing the customer’s requirement from the conceptual design stage to subsequent design stages. In general, functional features contain both purposes of design objects such as support, stability, or strength and behaviors of the design objects, like movement, rotating, or picking up [44].

For the sake of the structural optimization of products, the physics behaviors of a product are usually analyzed by CAE tools. *CAE features* are used to represent the specific knowledge involved in this process. It is a common practice that the topologies of product models by CAD have to be converted to specific geometries for CAE [45]. Thus, CAE features were developed for this purpose. Typically, they adapt to a CAE environment via removing the details and reducing the dimension of a CAD model [46].

In a manufacturing stage, the fundamental function of machining features is used to represent volumes of raw material to be removed [47]. With further development, machining features are defined from a purely geometric perspective to an object with geometric and topological characteristics which are associated with their machining information (such as tools and operations) [48]. To improve the manufacturability of products, some researchers raised this feature by embedding extra attributes and constraints, such as enriched machining feature [49] and 2.5D machining feature [50].

In an assembly stage, assembly features are used in assembly modeling and assembly planning via defining relationships between two groups of parts that need to be related [51]. Assembly features are no longer at the geometrical level. They contain the notations of design intent, technical function, technological solution, and manufacturing process [52]. Although the definitions were not consistent in literature, all focused on the relations between components. Typically, the relationships comprise face connections, constraints, parameters, kinematic relations, and structural relationships. In general, assembly features are defined as an information carrier for assembly-specific information within modeling and planning [51]. At the application level, this concept could support an automatic virtual model construction for complex components or systems. More recently, some extensions to the traditional assembly feature allowed product architectures to constrain the modular design of assembly geometry. This extension formed a new feature, called the associative assembly design feature [53].

2.2.2 Feature Interoperability and Information Consistency

Although various feature concepts provide a concise and clear way to represent the knowledge and information involved in the production modeling, they always lead to other problems, especially interoperability problems. Interoperability is defined as the ability of two or more systems or components to exchange and use information [54]. From different modeling perspectives, the same geometric shape may represent different engineering information. For example, a through hole is specified as a functional feature if described from its functionality, but the same hole may be classified as a machining feature if the focus is on the operations of the hole realization. However, these features are not always independent of each other. Multiple views are always integrated for managing activities in a complex system or throughout the lifecycle of a product. In a feature-based modeling environment, features usually model the entities involved in each view. As the feature semantics is drastically determined by different stages, the interoperability issue arises when they are used in a multiple-view integration [55]. Thus, feature conversion plays a critical role in feature-based multiple-view modeling. To develop sophisticated mechanisms of feature conversion, some research works have been done to maintain information (or data structure) consistency and provide intelligent and intuitive functional support that minimizes the possibility of process errors among multiple views. They are briefly introduced as follows.

In the early publications, some researchers developed multiple-view integration architecture with one-way feature conversion. An original design view usually drives the other views (e.g., finite-element analysis view and manufacturing planning view) [56,57]. Later, Smit and Bronsvoort [58] emphasized that the feature-based multiple-view modeling paradigm should propagate the changes in a multi-directional manner. Bronsvoort and Noort [59] proposed a multiple-view feature modeling covering conceptual design, assembly design, part design, and part manufacturing planning. Each view contains a feature model specific for the corresponding phase. In their work, the consistency of different features is kept on the basis of the consistency conditions that have been defined between their elements, such as degrees of freedom between references on the components.

More recently, with the occurrence of some new feature concepts, like new functional feature [60], physics feature [61], CFD boundary feature [62], and so on, the feature technology has been able to model complex integration systems. Brunetti and Golob [63] introduced a conceptual feature-based integration system that can represent conceptual design information and support the evolution of product semantics along a product development process. Due to more factors considered in concurrent design and engineering, the original definition of functional feature proposed by Schulte [43] is unable to carry functional information and specific engineering knowledge for the subsequent modeling stages, Cheng and Ma [60,61] proposed a new functional feature-based CAD modeling framework to solve this problem, as shown in Figure 2.3. This modeling approach applies functional decomposition to break down an overly abstract function into several more detailed primitive functions that can guide designers to use abstract geometry features to construct robust CAD part models within a functional framework. Further, physics feature, in the form of named variables and a set of mathematical equations for understanding physics phenomena, was used in their work for obtaining the performance of products [61].

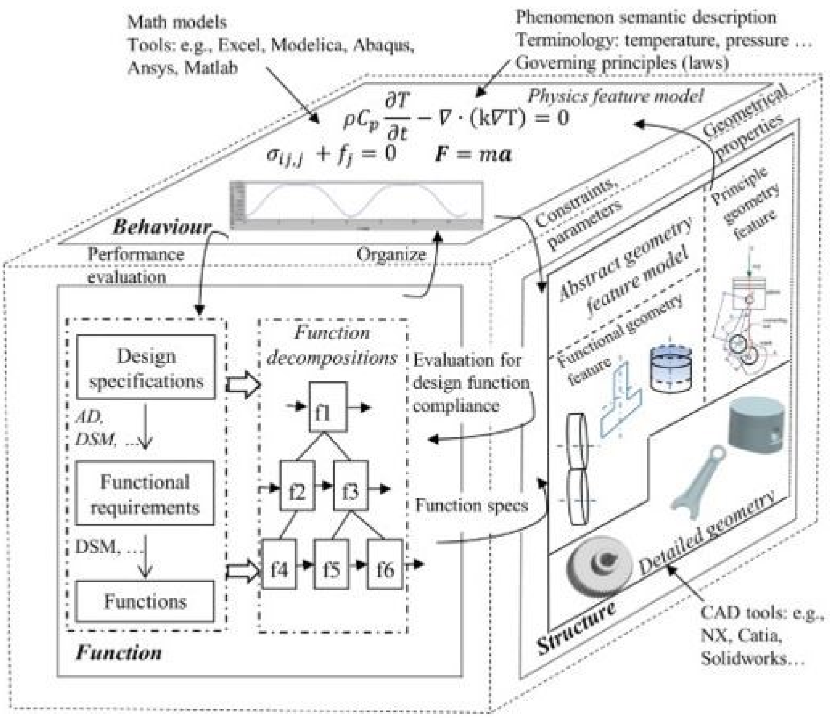

Figure 2.3 Functional feature modeling cube [61].

Looking into some applications in specific domains, Li et al. [64] proposed a feature-based CAD/CFD/optimization integration modeling method. Their method realized a seamless information transfer among CAD and CFD by clarifying the associations between the entities in CAD and CFD views, for instance, the functional fluid geometries are itemized as CFD boundary conditions like inlet and outlet. On the basis of this feature-based environment, to face the challenge from the emerging technologies, they developed an intelligent solver so that the knowledge from the CAD view can drive the physics feature to generate high-fidelity CFD models intelligently for the product development and industrial processes involved in fluids [13]. Besides, in order to fix the interoperability problem across mechanical and chemical engineering fields, Xie and Ma [65] developed an inter-domain functional feature. The associative relationships between the two domains were established by abstracting the design knowledge into the model constraints, such as design codes, expert rules, and numerical laws. These associations provide precise contextual information as well as convenient updates of functional mapping.

In summary, although feature technology has been mature enough in the area of system integration, its application in the digital ecosystem is in its relative infancy.

2.3 Industrial HVOF Process Modeling

The proposed framework in this research mainly services industrial processes. HVOF thermal spray process is selected to demonstrate the method because of its complexity. HVOF process optimization has remained a continuous challenge. As the developed digital model in Chapter 4 aims to provide optimal solutions to real-world operations, the previous strategies for optimizing the process are reviewed in this section (Section 2.3.1). To support the physics phenomenon simulation, this section also reviews the HVOF process numerical modeling in the past 20 years, which experienced two important periods, in-flight behavior modeling and dynamic coating process modeling. The in-flight behavior modeling focuses on understanding the physicochemical phenomenon of the combustion reaction, gas-flow dynamics, and in-flight particle behavior by using the CAE technique (Section 2.3.2). The dynamic coating process modeling concentrates on simulating the coating/substrate dynamic behavior during a robot-assisted thermal spray process (Section 2.3.3).

2.3.1 HVOF Process Optimization

According to the coating formation mechanism [66,67], the mechanical properties of the spray coating are significantly affected by the physical and chemical states of the in-flight particles, such as velocity, temperature, degree of melting, and oxidant contents. The in-flight particle behavior, however, is coupled with the gas dynamics, which are directly related to the process parameters, such as the gas flow rate, the fuel/oxygen ratio, spray distance, and other various operational conditions, like the spray system used and the fuel/oxidant types [68]. Because of the complexity of the process, exploring strategies for optimizing coating performance has remained a continuous challenge in the relevant research field. In the past two decades, generally, two approaches have been taken to optimize the HVOF process, numerical and experimental.

Experimental works focused on studying the effect of the critical process parameters on the coating properties based on statistical techniques; the 'best' operation parameter sets for specific coating properties can be obtained through various optimization methodologies. For example, Thiruvikraman et al. [67] conducted 32 sets of experiments to develop empirical relationships to maximize adhesion bond strength and lap shear bond strength of WC-CrC-Ni coatings by using a specific HVOF system. Vignesh et al. [69] used a similar method to generate the coating with minimum porosity and maximum hardness on 316 stainless steel, and Thermsuk and Surin [70] generated the coating with a maximum hardness, minimum porosity, maximum thickness, and minimum surface roughness on SUS 400 stainless steel. Based on experimental data, Praveen et al. [71] adopted the Taguchi method to optimize spray parameters for optimal erosion resistance by using their developed coating materials. In summary, this experimental approach usually needs a number of experiments to establish the effective impact relations produced by the process parameters that affect the specific coating properties. Although the experimental approach is reliable for a specific industrial scenario, it is expensive and time-consuming. In addition, the solution derived for one specific scenario may not be applicable to other scenarios where different configurations or parameters, (e.g., nozzle configuration, powder, or fuel type) are involved [72–74]. Hence, in the current imperative technology demanding context, the numerical analysis approach is of greater importance.

Another optimization strategy is based on the traditional numerical study. Typically, the numerical study approach focused on the fundamental modeling of the process, such as combustion, gas dynamics, and the in-flight particle behavior, and then the simple parametric analysis was usually applied to find out an optimum solution. With the rapid development of computer-aided engineering (CAE), computational fluid dynamics (CFD) simulation, as an important component of CAE, has reached a high level of sophistication, which makes parametric analysis of the process feasible. Some researchers aiming to explore the optimal operational setups have established different numerical models by using CFD. Li and Christofides [72] proposed a hybrid fundamental model for the physicochemical behaviors and revealed the effects of the chemical reaction on the in-flight behaviors of the particle-gas jet; an optimal equivalence ratio close to 1.2 for propylene-oxygen combustion is analyzed. Baik et al. [73] created a similar computational model to investigate the qualitative relationship between nozzle geometries and the physics properties of the flame by using parametric analysis. Based on their conclusions, the nozzle geometry could be optimized to obtain the optimal status of the flame. The combustion models in these two works were built on propylene-oxygen combustion via 2-D simulation. By using a similar computational model, Khan and Shamim [75] further explored the effect of nozzle geometries and investigated the physicochemical performance in a dual-stage HVOF system. Emami et al. [76] kept on the research works on the dual-stage HVOF system and discussed the effects of two combustion models on the temperature and velocity fields in this system. Pan et al. [6] built a 2-D liquid-fueled HVOF model but with kerosene-fueled chemical reaction and further optimized the shape factor and inject velocity of the particles to reach an ideal status of the in-flight particle behavior. Kamnis and Gu [74] constructed a 3-D kerosene-fueled HVOF model to examine the effects of the liquid fuel droplets on the thermodynamics of the combustion gas flow.

More recently, some researchers concentrated on the numerical modeling of the more advanced Suspension HVOF (SHVOF) process and the expensively two-way Eulerian-Lagrangian scheme that was used to simulate interactions between the evaporative suspension droplets with the gas phase [77,78]. In general, to the authors' best knowledge, even though the numerical study is becoming increasingly mature, most previous research works have only aimed at qualitative interpretations of parameter sensitivities to the process, and there has been no published work on the multiple-view modeling method which is expected to enable an integrated HVOF numerical modeling and optimization methodology.

2.3.2 Numerical Modeling of the In-flight Behavior

In this thesis, the in-flight behavior refers to the physicochemical behavior of the flame and in-flight powder particles before and after the injection from the nozzle, as described above. Based on the mechanism of HVOF processes, the in-flight behavior model should at least cover the physicochemical phenomenon simulation of combustion, gas dynamics, and the in-flight particle behavior. Regarding the droplet deformation and solidification, an individual model was always used for this phenomenon, however, the inputs (e.g., powder particle melting ratio, velocity, etc.) should come from the in-flight behavior model. To support low-level computations in this thesis, the numerical models commonly used in related publications for understanding these phenomena are summarized in this subsection in terms of the different physicochemical phenomena involved.

As the flame flow in HVOF processes is subsonic/supersonic, the flow should be treated as a high-Reynolds-number turbulent compressible flow. For complex turbulent flow problems, Reynold and Favre averaging was used to simplify the small-scale turbulent fluctuations [68,77]. To represent the effect of turbulence, the Reynolds stress term was estimated by using the *k-ε* turbulence model (normalization group *k-ε* turbulence model or realizable *k-ε* turbulence model was usually used) [73,77,79]. The mass fraction of each species after the reaction was governed by the convection-diffusion equation [72,78]. Based on the fact that the fuel and oxygen are mixed thoroughly before feeding to the combustion chamber, a single step and eddy-dissipation model was always used to simulate the combustion [79,80]. On the particle dynamics side, owing to the very low particle loading (less than 4% usually) [81], a one-way coupling between the gas phase and the particulate phase was assumed in [82–84]. According to the analysis in [85], it is reasonable to assume that the particle coagulation process is negligible and the powder size distribution does not change during the process. The motion of the particles was governed by Newton's law with the major drag force [6]. Regarding numerical discretization methods for solving the corresponding governing equations, a first-order upwind scheme was used first to get a convergent solution, then the shock diamonds at the nozzle's exit could be refined by using a second-order upwind scheme if necessary [86]. Some of these models have been verified by experiments, like flame behavior and the shock diamond existence [80]. Owing to this sophisticated modeling technique, these models are used in this thesis. The mathematical representation of these models is presented in Appendix 1.

2.3.3 Dynamic Coating Modeling in Robotized Thermal Spraying

To explore the effects of the kinematics on the coating process, several research teams proposed numerical models for robot-guided thermal spraying processes. Bolot et al. [87] proposed a dynamic process model that allows taking the robot dynamics into account. The spray pattern for thermal flux and coating thickness was estimated by mathematical derivations based on a vacuum plasma spraying, which limits the model to be applicable for different vacuum plasma spraying systems. Candel et al. [88,89] presented an idea enabling to remedy the shortcoming in Bolot's model. The calculation of the contribution of the flame and particles to the total thermal load could be done by considering CFD simulations of the combustion and in-flight behavior of the flame and particles. However, the approach integrating the CFD spray model into torch trajectories was not introduced in their publications. In addition, in their research, to overcome the issue of the difference between the time step in CFD tools and the time interval among trajectory points, every trajectory point was associated with the nearest node of the substrate surface mesh, which may increase the simulation error when the time interval is increased.

As the robotized thermal spray process modeling gets sophisticated, the prediction and optimization of the coating thickness and substrate temperature have been brought to the fore. Based on a simulation model, Hegels et al. [90] concentrated on optimizing a given nozzle path to improve the coating thickness uniformity on a workpiece with flat and curved regions through an iterative post-optimization. The 3D coating height profile used in their simulation was analytically formulated, which did not consider some specific operating parameters, like electric arc current in the plasma spraying or fuel gas flow rate in HVOF thermal spraying. Chen et al. [91] constructed a numerical coating profile model through a Gaussian distribution fitting. Chen's model is specific to the cold spray process and focuses on the kinematic parameters, such as spray angle, spray distance, and nozzle traverse speed. Zhang et al. [92] created a spherical surface coating thickness model. A spherical coordinate system was employed to describe the Gaussian coating profile which required a preliminary experiment to estimate the height of a single coating profile. Their model was validated by a specific set of parameters in the plasma spraying. More recently, Deng et al. [93] reported an approach predicting coating thickness for components with complex curved surfaces, especially in the case of shadow effects. They further developed the Gaussian coating profile model concerning the parameters of spray angle, spray distance, nozzle traverse speed, and deposition efficiency. However, since the data used for constructing the Gaussian coating profile was obtained in cold spraying, their model is limited to this technology. As to the aspect of HVOF thermal spraying, the coating thickness prediction is still in its relative infancy due to the complexity. Li and Christofides [94] presented a stochastic simulation method to predict the microstructure of HVOF coatings. Besides, based on experimental validation, Mostaghimi et al. [95] proposed a set of rules to simulate the build-up of a small area of the coating. However, the coating thickness simulation was not shown in their papers. Regarding the field of substrate temperature, the influence of robot trajectory on thermal history was first studied by Nylen and Edberg [96]. A heat transfer model between the plasma and component was built by using the FEA. Candel and Gadow [88] firstly proposed a coupling mechanism to link a CFD of the in-flight behavior of gases and particles and a finite element model of the substrate component so that the heat flux calculated by the CFD model can be used for simulating the substrate temperature. Liu et al. [97] developed a finite element model for the transient analysis of the temperature and residual stress formation of the substrate component. The contribution of sprayed particles to substrate heating was taken into account using a heat flux presenting a Gaussian distribution profile. Their work focuses on the physic understanding and lacks the capacity for various working scenarios.

Based on the above-mentioned findings, most models mainly concentrated on the effect of the kinematic parameters on the development of the coating. Some operating parameters and working conditions in specific thermal spray technologies, e.g., the gas flow rates and the nozzle geometry in HVOF processes, are not involved.

To sum up, even though the numerical studies of HVOF thermal spraying are becoming increasingly mature, most previous research works have only aimed to understand the fundamentals of the complex phenomenon. The applications of these models into the DT concept are still restricted.

Chapter 3: Conceptual Framework of Feature-based Modeling in a Digital Ecosystem

3.1 Chapter Overview

The concept of DTs has been gradually mature. A complete conceptual model containing multidisciplinary technologies has been given in recent publications [24,36]. The applications of the concept are increasingly being embraced by manufacturers. However, most studies focused on the applications of emerging technologies in the concept, like artificial intelligence, virtual reality, augmented reality, and big data. Research works relevant to the simulation model construction and real-world data processing in the simulation, especially real-world physics phenomenon simulation involved in the industry, are limited. As mentioned in Section 1.3, this thesis concentrates on the modeling of industrial processes in the context of DTs, which concerns physics in real-world phenomena.

Therefore, instead of looking for futuristic goals of the DT's framework, the first objective of this thesis is to develop a practical framework of digital twins toward the current industrial status. In the framework, an industrial process will be divided into some sub-level models in terms of physics phenomena involved, where CAE tools are mainly utilized here with near-real-time input data for simulating the phenomenon in each sub-level model. This framework clarifies the data processing in the CAE environment for challenges from the digital twin concept. Meanwhile, it also provides the capacities for adding the new features in digital twins with the supports of real-world systems in the future, e.g., data acquisition system and control system [98].

Before the concept of digital twins, feature technology [55] had achieved great success in the modeling of production and manufacturing process to capture interdisciplinary entities as well as association relationships between different stages or domains of the whole product lifecycle [8], which enhances simulation models to a smart and flexible level. With its significant advantages of information fusion and multiple-view integration [38], creating multi-view models for complex manufacturing processes is no longer a cumbersome task. However, in view of the recent progress of emerging technologies, because of the new structural formalism and transmission of the data, feature modeling is facing challenges with the new-generation information technologies, such as the Internet of Things (IoT), artificial intelligence (AI), and big data. To enhance the flexibility of the proposed framework for different processes and scenarios, advanced feature technology is adopted to model the sub-level models for the basic compositions in the proposed framework and capture interdisciplinary entities and association relationships for the foundation level. The feature concepts are extended in this work so that the common characteristics in the concept of digital twins can be considered.

Some industrial process modeling in the view of digital twins and the evolution of feature modeling have been separately reviewed in Sections 2.1and 2.2. The remainder of this chapter is organized as follows: In Section 3.2, the terminology in the previous literature is introduced. Based on these concepts, a hierarchical structure for describing an industrial process is proposed. Section 3.3 outlines a conceptual framework for clarifying the roles of these concepts in a digital ecosystem. In Section 3.3.2, the real-world data processing and mutual supports among different modules in the framework are outlined. Section 3.4 introduces the feature concepts tackling the challenges from the DT concept.

3.2 Terminology

The traditional industrial process information models tend to have a weak hierarchy, which adds much difficulty to the clear organization and standard expression of process information. To overcome this issue and apply the proposed modeling method in a digital environment, the concepts commonly used in the clutter of digital twin-related literature are identified firstly. Then relying on these, a concept, feature-based digital model, as a foundation, is proposed to form a hierarchical structure for modeling industrial processes.

The terminology in the current digital-twin related literature is shown as follows:

- Digital twin (DT) is a virtual counterpart that is linked to a real-world entity. The information can be distributed among different systems, but the pieces of information should be linked to each other to form one coherent entity. The term digital twin serves as a common noun for any kind of digital twin object [26,36,99].
- Digital twin instance (DTI) represents the virtual counterpart of a specific real-world industrial process. It should describe and serve a physical process comprehensively, including rule-based methods for generating robust models, a structural database for representing physical phenomena, strategies for deriving engineering solutions, and so on. To achieve this, it might be composed of virtually separated units for describing different physicochemical phenomena involved in a process. It must be constantly available on the Internet to ensure the constant flow of data [4,100]. Each DTI has a unique identification that can be used to connect to the Internet and fulfill works related to big data and AI.
- Digital twin class (DTC) refers to a virtual model temple of a series of real-world industrial processes with similar features. These similar industrial processes are treated as DTIs, as depicted in Figure 3.1. They can be represented in a virtual environment in a standardized way [4]. In this research, the standardized way is described by the advanced feature technology.

However, the models built on these concepts might not be primitive enough. This research further decomposes the virtual model into smaller granularities, as shown in Figure 3.1. Meanwhile, to apply the advanced feature technology, the concept of a feature-based digital model is proposed to build a base of a hierarchical structure for describing an industrial process.

- Basically, an industrial process comprises multiple devices and involves various physical phenomena. On the virtual side, it is hard to capture all information by a single simulation module because a module in simulation tools is usually designed for a series of specific physical phenomena with similar physical characteristics. For comprehensively modeling an industrial process, feature-based digital models (FDM) use the advanced feature technology to construct standardized templates for basic units of a digital twin whose behaviors are commonly simulated in a single simulation module and then clarify the inter-model associations among them, as shown in Figure 3.1. Thus, a feature-based digital model refers to a unit on the virtual side, and its model is built on a specific simulation tool, yet containing all information, e.g., computation, analysis, intelligence, and optimization. The idea of modularity has been accepted in previous related publications [4,33], although the modularized objectives are different.

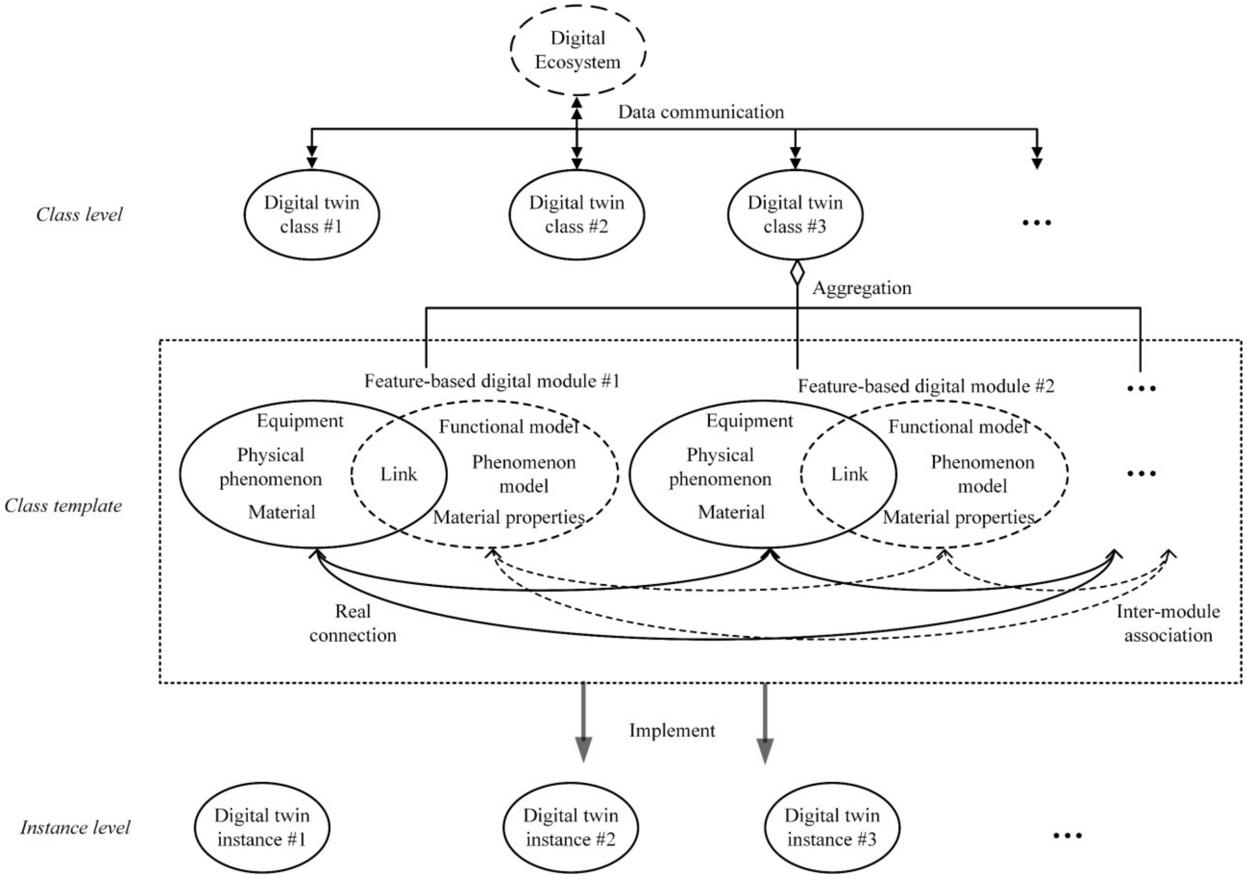

Figure 3.1 A hierarchical structure of digital twins

Based on the fact that an industrial process always comprises multiple devices and involves various physics phenomena, the digital twin class could be decomposed into several modules, as shown in Figure 3.1, where every module is defined as a feature-based digital model and serves for specific physics in the real world, such as the UML (unified modeling language) representing template for generally modeling the in-flight behavior existing in various HVOF spray guns (Section 4.3) and the template for generally modeling different substrates and coating layers (Section 6.3.1). Different modules (feature-based digital models) connect with others via some characteristic parameters. Like the coupling methods commonly used in numerical modeling, sometimes, iterative coupling algorithms need to be specifically designed so that robustness could be achieved. These connected feature-based digital models form a standardized template of the whole process which is called the digital twin class. Owing to the feature-based modeling environment, an industrial instance can be easily created by carrying out its actual scenario, like the value of operating parameters. All digital twin instances generated by a digital twin class have the same model structure and data format. This hierarchy magnifies the benefits of implementing emerging technologies.

3.3 Conceptual framework

3.3.1 Introduction of the conceptual framework by using an HVOF process

Figure 3.2 schematically illustrates the proposed conceptual framework by using an HVOF process. It composites three major units. In the concept of digital twins, each unit has a real entity and a corresponding virtual representation. Each virtual representation could be treated as an individual feature-based digital model. These feature-based digital models associate with each other to realize the real connection in the virtual side, as well as communicate with a cloud database for implementing the new-generation technologies [101]. To realize the connection, communication and data transfer are critical procedures. A digital twin class for an industrial process usually needs multiple feature-based digital models which closely work together. They are always connected via Ethernet or parallelly run on a single processor. Thus, a consistent Ethernet protocol, e.g., EtherCAT, might be used to standardize the communication functions. Due to the global distribution of the DTs and the types for different fields, the data might be transmitted to the collaboration environment via different interfaces and communication protocols (e.g., Profibus, TCP/IP, and Modbus [19]), which increases the difficulty to execute the data analysis. Hence, these protocols should be mapped to the ISO Open Systems Interconnection (OSI) model [3].

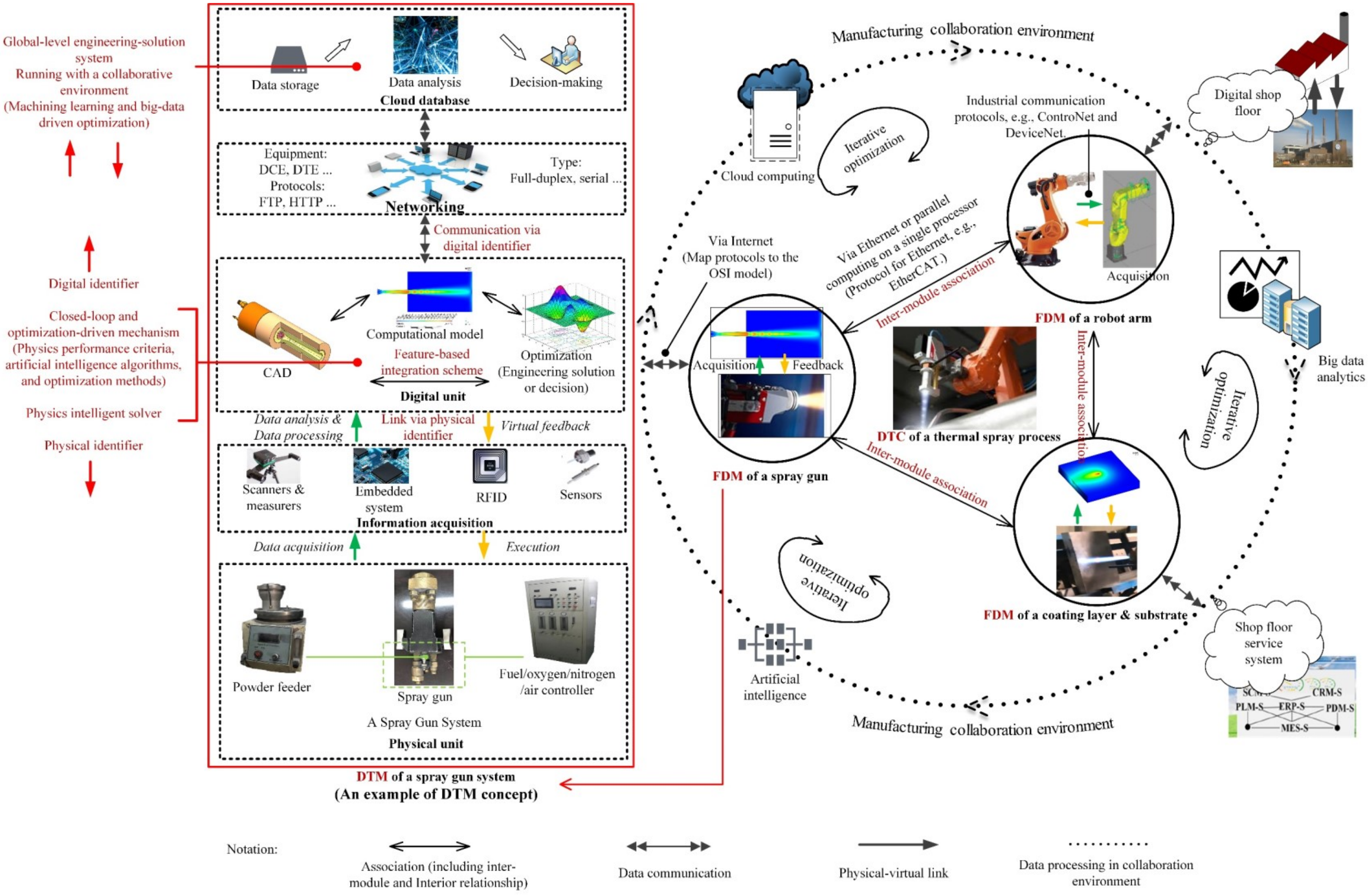

Figure 3.2 Schematic representation of the conceptual framework by using a homemade Dimond Jet HVOF system.

The concept of a feature-based digital model is further elaborated by using a relatively complicated unit, the Dimond Jet gun system, as shown in the left of Figure 3.2. The realization of the DT concept needs at least four levels, physical equipment, data acquisition device, simulation model, and cloud platform. In a Dimond Jet gun system, the thoroughly mixed fuel-oxygen gases (typically hydrocarbon-oxygen) and micro particles are fed into the gun chamber where a combustion reaction takes place which in turn generates a hot-sonic/supersonic multiphase gas stream. Within the stream, micro particles of metals, alloys, and/or ceramics are accelerated, heated, and ultimately deposited onto a substrate at high speed [66,102]. The gas flow rates and powder feed rate are monitored and controlled by the gas controller and powder controller as shown in Figure 3.2. By connecting the equipment with special sensors and actuators, the system can reach a DT level. State changes on the physical side are monitored by sensors, then collected and transmitted to the virtual side. Some communication protocols, e.g., ControNet and DeviceNet [3,103], are needed here to bridge the different data structures and formats. By modifying these protocols to satisfy the real-time and reliability requirements of the DT concept, the real-time state is able to be sent to the virtual model as setup parameters and vice versa. For instance, specific sensors could be embedded in the gas controller system for detecting the real-time gas flow rates. This data will be transferred to the virtual model via a protocol that adjusts the data format and defines the transmission. Apart from these requisite rulers and methods for bridging the physical-virtual connection, a concept of the physical identifier is proposed as an attribute in a feature-based model to accurately link these parameters in the real world, like fuel, oxygen, nitrogen mass rate, and so on, with the ones on the virtual side, where the components in the virtual model are abstracted as class levels with standardized attributes. The feature concepts will be illustrated in

Section 3.4. In the feature-based model, an intelligent solver is often necessary to respond to the changes of real-time input data when the real-world operations change. Facilitated by the internet-based connections and communications in manufacturing, the simulation results from the virtual side should be self-organized into resource communities and then further analyzed in a manufacturing collaboration environment by emerging technologies with their labels, digital identifiers.

3.3.2 Real-world Data Processing and Mutual Supports among Different Models

In a real industrial process, typically, partial operating parameters or conditions are always changing with progress. Others might be constant, or their changes with the progress can be determined and predictable. Based on this fact, the input data processing in the modeling process and mutual supports among different models are further illustrated in Figure 3.3 to realize the synchronization of phenomena. After receiving the input information, the first step is to determine whether it should be dealt with an online mode or offline mode. Generally, the data inputted to the CAE environment could be divided into two types, real-time data that changes with the real scenario, and known data whose change throughout the simulation can be known in advance. An online mode means the simulation state is synchronized with the real-world scenario and/or real-time phenomena of other models, where every time step the model reads data from the sensors and/or outputs by other models and updates its boundary conditions and/or setup parameters with this information. In terms of the time interval for receiving this information, the feature-based digital model should set up the same or integral multiple time step size of the time interval so that it can read and load the synchronous data every certain time interval. Then, according to the real-world scenario, the model could calculate the time length, which in turn determines the number of time steps. It is worth noting that, after starting to run the model, the time reference of the data from other models could be different from the feature-based digital model. Thus, the data must be adjusted to the same time reference. The online mode requires that every time step the model must read the synchronous real-world and/or inter-model data, and then update the CAE setup parameters and/or boundary conditions. After completing the input setups, the physics solvers are activated. Then, the obtained periodic results for each time step are exported and recorded by ASCII files which can be uploaded to a could database or transferred to “common data models” for other feature-based digital models. On the other hand, an offline mode does not link to real-time updates. Before the initialization of simulation, the change of setup parameters and boundary conditions can be determined and predictable in advance. There are two ways to synchronize the phenomena among different models. One is the same as the online mode if any other models adopt the online mode. Another one, as depicted on the right side of Figure 3.3, is to acquire the data from sensors and/or run other models in advance, where the other models must fully run in the offline mode, and then construct functions of time and/or store the data into a “common data model”. These functions can be assigned to time-dependent setup parameters and/or boundary conditions in the feature-based digital model. The data from the “common data model” could be loaded into the CAE environment beforehand. The variable of time should be matched with the time in the feature-based digital model as well.

In general, in a real digital-twin system, the changing scenario is detected by the data acquisition devices and sent to the virtual side. To timely replace the corresponding setups in the CAE model with the latest data, every CAE time step, the online mode reads the file and loads the data via defined associations. For the known operating parameters or conditions throughout the progress of the simulation, the offline mode loads all the information before running the simulation. Thus, the online mode can synchronize the changing input data, however, it costs more simulation time for approaching data transmission. The offline mode avoids the time-consuming data transmission during the simulation, which can enhance the timeliness for the real-time capacity. However, the change of setup parameters and boundary conditions must be known in advance.

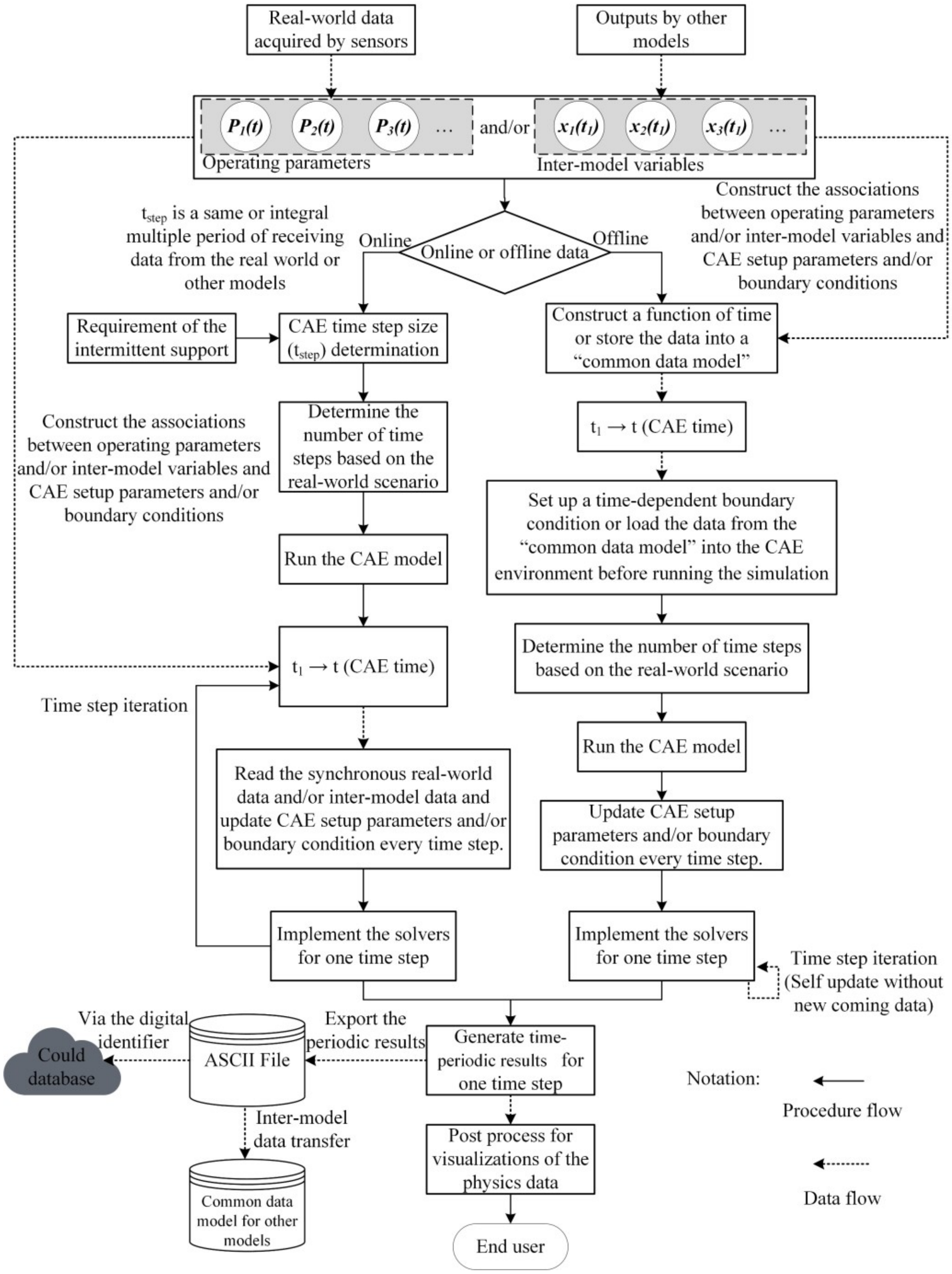

Figure 3.3 Procedure and data flow for the real-world data processing and mutual supports among different models.

It can be noticed that the proposed framework enhances the construction of the digital twin of an industrial process to be manageable and systematic. Furthermore, the modularization idea in the framework significantly raises the capacity of timeliness. Typically, a single virtual model with the consideration of all physics phenomena involved is hard to realize. Moreover, a full-scale physics model usually requires many hours of computing time. In this case, the capacity for the interaction of operation support would be compromised. The proposed framework modularizes an industrial process simulation in terms of different physics phenomena. In this way, the complex modeling is simplified, and the professional solvers can be appropriately used for the specific physics phenomena, which remarkably increases the timeliness capacity.

From a low-level point of the model application, as shown in the left of Figure 3.2, by embedding physics performance criteria, artificial intelligence algorithms, and optimization methods, the feature-based digital model is capable of providing some local services, like predictions or advice for its real twin. For instance, in Section 4.3.2, under the optimization-driven mechanism, the operating parameters, such as gas flow rates and spray distance, were automatically outputted from a robust model for the in-flight behavior of the powder particles to obtain excellent coating properties of porosity, deposition efficiency, and adhesion strength in HVOF processes. Besides, owing to the increased timeliness capacity, the complicated physics behaviors can be monitored with the real process progress. By equipping with a control system, like the inverse way of receiving the real-time inputs from the data acquisition systems, the feature-based digital model can control and execute the real-world process. The optimal operating parameters for expected working performances and real-time adjustments for correcting operating errors and avoiding unexpected performances could be translated to control signals which command the actuators to carry out such model outputs on the real side. In this way, it could achieve a tight interconnection between the virtual model and its real twin.

In view of a high-level application, the feature-based modeling method works as a template for collecting data from similar industrial processes globally. As shown in the right of Figure 3.2, running with a collaborative environment, the same data format and structure from different machines or materials could collaborate. The proposed feature-based digital modeling will enhance global industry development from the virtual world, where the global information collection will support big-data driven optimization for industrial processes [26,27].

In terms of the above description, it is obvious that information fusion and data management also play significant roles in constructing a virtual model toward the concept of digital twins. In the next section, the capacity of the feature technology is extended to cover these challenges.

3.4 Feature-based Semantics Model

This section proposes a standardized model template that can guide the modeling process to cater to the trend of digital twins in the industry by clarifying the model elements and organizing their functional relationships such that they are dependent, associated, and aggregated. Further, a multiple-view integration framework is constructed by using these elements. The interior relationships among the views are also elucidated in this section.

Advanced feature technology has been applied in product modeling to capture interdisciplinary entities as well as association relationships between different stages or domains of the whole product lifecycle [8]. In this research, except the traditional association relationships, the application of feature technology is to manage the periodic update of the interior relations so that the real-world data can timely control the running of subsequent views, and also keep the inter-model consistency which enables the phenomenon synchronization among models. To leverage the advanced feature technology in the concept of digital twins, some feature concepts are extended to deal with the key characteristics of digital twins, like physical-virtual communication, real-time capacity, and process optimization.

As depicted in Figure 3.4, *CAD functional feature* as an extension of the functional feature [60] is defined as a class of virtual representation of real basic units that are composed of geometrical entities and non-geometrical entities (e.g. equipment specifications, physics behaviors existing on the geometrical entities, and geometrical functions), where these entities could change with the real-world scenario via the *physical identifier* which is also embedded as an attribute in the CAD functional feature. *Physical identifier* [4] is defined as the identifier linking the physical space to the digital space. Hence, the physical identifier enables local sensors access to the virtual model, serving as a gateway between the physical assets and their digital counterpart. For example, in a thermal spraying factory, a group of nozzles might be used. These nozzles have different functions due to their characteristics. To distinguish them, they generally have a unique identification code in the real system. Correspondingly, their virtual models should have an identifier so that the real-time state and information of the real nozzle exactly link to the virtual side. This identifier could use the same code in the real system. Another new concept missed in the previous feature modeling is *digital identifier* [4] which is a way to connect a feature-based digital model to a network. The digital identifier has two requirements. It should i) be unique at a sufficient level, optimally globally, and ii) enable access to the feature-based digital model from any part of a digital twin network, optimally the Internet [4]. For example, the uniform resource identifier (URI) [4] can be used as the digital identifier, which is the parent category of the common URL addresses. As a feature-based digital model is defined as a digital block of a unit with similar characteristics, by adding the digital identifier concept to a feature-based digital model, the solution can be transmitted to a ‘cloud’ and analyzed using big data analytics and AI technique. When CAD models are built, geometrical entities, e.g., faces, edges, and points, are allocated to these two identifiers so that the real-time data and the model outputs could be exactly linked and transferred to virtual models and a cloud platform respectively.

Looking into the CAD/CAE integration view of Figure 3.4, in this mechanism, typically the geometrical entities in the CAD functional feature are mapped to specific counterparts in the subsequent simulation tools. For example, the volumes enclosed by faces could form computational domains in a CAE view, and the process functional geometries might be itemized as setup parameters of the subsequent view models, such as symmetry planes/axes, gas/particle inlets, and inner faces enclosing fluid space. The non-geometrical entities (e.g., manufacturing system specifications) define setup parameters or constraints. *CAE boundary feature* is defined as a class of features that contains such mapping relations of geometrical dependencies between CAD entities and their associated CAE mesh representations as well as non-geometrical dependencies [62]. In this way, the virtual models in subsequent views are controllable from the previous views. In addition, the real-time data from sensors could be transmitted to these views via the feature association and the geometries linked to the identifiers.

In the previous applications of the feature technology, different features were usually used to model the entities in an individual model. The multi-view integration also focused on the information fusion within one model. The mechanism for real-world data control and the information communications among different models were not covered. In this research, the CAD functional feature and user-defined boundary condition feature work together for dealing with these problems. In contrast to a boundary condition with a constant value, the *user-defined* *boundary condition* in Figure 3.4 is defined as a new feature concept containing time-dependent variables controlled by the real-time data from the sensors or other models with a series of algorithms for automatically employing the time-dependent variables to establish changing setup parameters and/or boundary conditions over time. As depicted in the upper-left corner of Figure 3.4, based on the above CAD/CAE associations, once the non-geometrical entities in a "common data model" attached to the CAD functional feature are updated with the real-world scenario, the value of the associated time-dependent variables in the user-defined boundary condition feature will correspondingly change. When the next time step starts, the algorithms embedded in the user-defined boundary condition feature will replace the old value with the newest value of the time-dependent variables before triggering the physics solvers in the CAE analysis view. As mentioned in Section 3.3, special attention must be paid to the time reference of the input data. To realize the synchronization with the real world and/or other online models, the feature-based digital model should set up the same or integral multiple time intervals of the data transmissions from sensors and/or the online models' time iteration so that the user-defined boundary condition can read and load the synchronous data every certain time intervals.

According to the above mechanism, a feature-based digital model also needs a good capacity to respond the real-time data synchronously and automatically from sensors and/or other models. Therefore, an intelligent solver is a prerequisite to automatically understand the physics behaviors behind processes when a new set of data is sent to the virtual model. Typically, the solver can be featured to realize the intelligent and automatic abilities for a specific physical behavior [64]. For this purpose, at the upper-right corner of Figure 3.4, *physics feature* is defined as a class that contains the related modeling parameters and the corresponding governing equations for a specific phenomenon with the aggregation of *intelligent solver* including a set of knowledge-based rules to determine the solver setup parameters and criteria for confirming the robustness of the model. To automatically generate a robust numerical model without human interactions, an effective approach is to embed artificial intelligence or knowledge into the modeling system. This embeddedness generally needs physical knowledge and the best practices in specific fields [13,104]. Taking the HVOF process as an example, an intelligent solver for understanding the complicated physicochemical phenomenon of the combustion, flame, and in-flight particle, will be explained in Section 4.4. This physics solver can flexibly adjust the model setups to fast respond to the variations in the real world. It starts from the commonly used operating parameters and contains the process of computational domain determination, reaction formula calculation, solver setup, and convergence analysis. In the case study, it was used directly for solving the physics phenomena involved in the static in-flight behavior model.

Finally, the robust analysis model will run to generate analysis results. These results are further clustered into a feature concept, *phenomenon feature* in the bottom-right corner of Figure 3.4, in which, the different physics behaviors are established. The proposed feature primarily works as an interface that enables the phenomenon information from the CAE model to be usable for the optimization view. In addition, the phenomenon feature contains the methods for visualizing the complicated physics data obtained from the analysis model. It also should be noticed that, with the concept of digital twins, most solvers are switched to the transient mode. Thus, all obtained analysis results are time-dependent. The phenomenon feature stores the result every time step or every certain time step subject to the application. As shown at the bottom of Figure 3.4, the end users are able to access this feature to check the results.

So far, under the aforementioned scheme, the model can easily communicate with other models, as well as, support the real-time capacities. Regarding process optimization, like reducing cost, shortening time, and improving quality, an effective optimization model should be clearly devised. To systemically integrate the optimization process, the *process optimization feature* is proposed here as an extension of the associative feature concept into manufacturing process optimization. As shown in the bottom-left corner of Figure 3.4, it contains optimization intents that are derived from manufacturing requirements, and optimization attributes, like design variables, constraints, optimization equations, and optimization algorithms, and so forth. To generate a process optimization feature model for a specific industrial scenario, clear association rules are required to support information transfers between variables of the optimization process and entities of the feature-based CAD/CAE integration mechanism. Apart from the parameter association mechanism, due to the implicit expression of optimization objectives, constructing a fit-for-purpose model is also crucial for the optimization process, which enables the conversion from engineering problems to mathematical models. This process is usually implemented through expert knowledge and best practices in engineering optimization. With this mechanism, firstly the complex physics phenomena behind the industrial processes are visualized on the virtual side so that the end users without special knowledge could readily understand them. Secondly, the physics phenomena are monitored on the virtual side with a slight delay. Some criteria could be added as triggers to ensure that the real system runs reasonably. Thirdly, with the interior associations established, the model could be optimization-driven for providing engineering solutions for the real world. For instance, in Section 4.3, the optimization view drove the system and calculated the optimized operating parameters for improving the HVOF coating quality. In the future, with a control system joining, these optimized parameters could be fed back as control signals for the actuators in the real operating system.

Further, to enhance the optimization to a level toward future manufacture, the concept of digital identifier [4] is also used and aggregated into the process optimization feature as illustrated in the bottom-left corner of Figure 3.4. Finally, as depicted in Figure 3.4, a real-time, optimization-driven, closed-loop, and multi-view digital block template for the basic unit in industrial processes is completed.

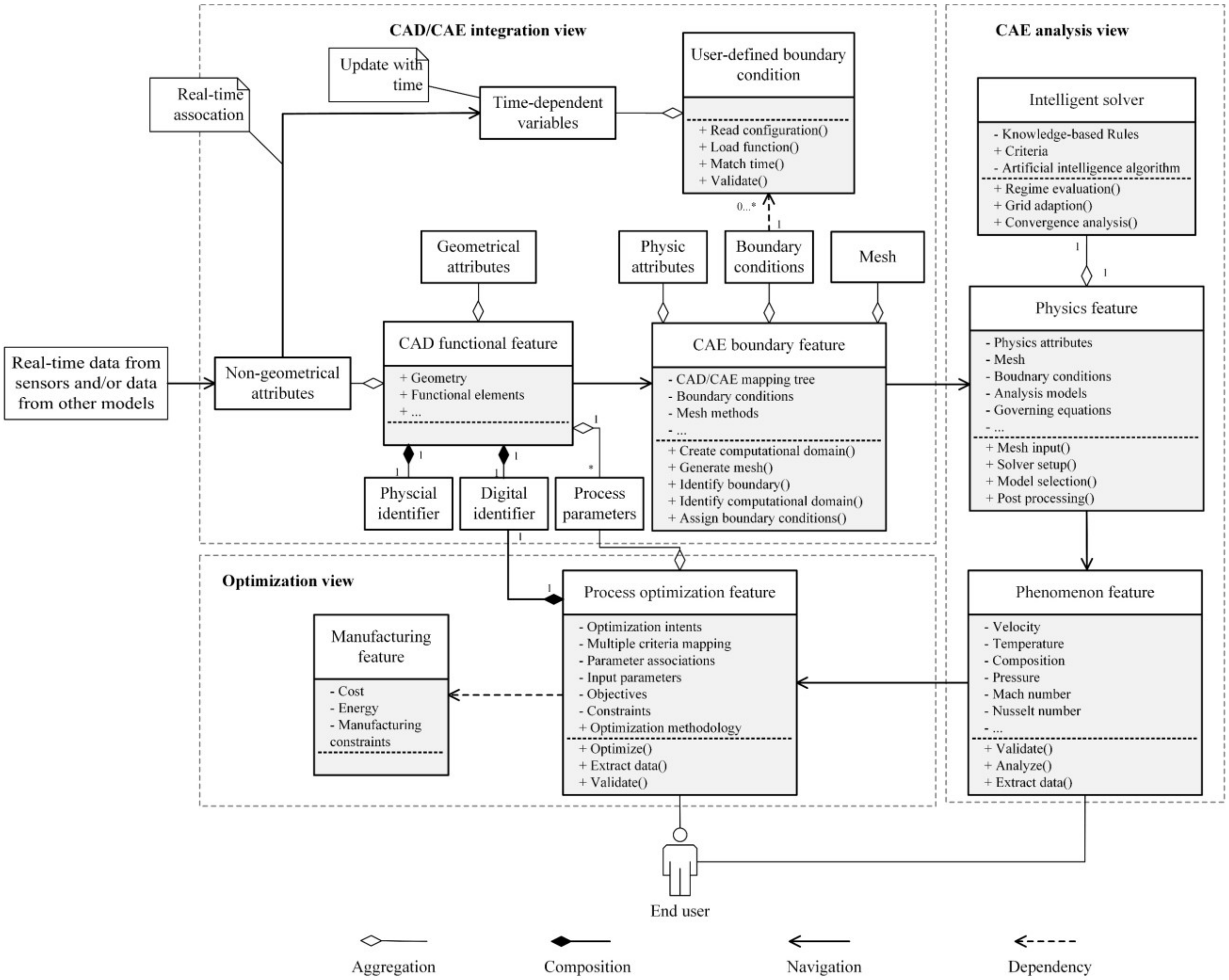

Figure 3.4 Feature class diagram representing inter-feature associations based on UML (Unified Modeling Language).

3.5 Conclusions

Against a background of smart manufacturing, an increasing level of interest in research on digital twins has been witnessed over recent years. With the development of the new-generation information technologies, digital twins of manufacturing processes refer to an ideal state of manufacturing, in which real-time transmission and analysis of data from across manufacturing processes, along with model-based simulation and optimization, create intelligence to yield positive impacts on all aspects of manufacturing. However, the recent works mostly focused on the implementation of the emerging technologies into the concept. The digital counterparts of physics phenomena involved in manufacturing processes are always ignorable. In the view of traditional simulation tools, like CAE, CFD, and so on, the works on a systematic method of leveraging them in the aspect of digital twins are very limited.

Thus, this study contributes to the modeling method of industrial processes in the context of digital twins. Based on the hierarchical structure of digital twins in previous research works, a semantic information modeling framework toward the realization and integration has been developed. Distinguished from other existing digital twin frameworks, the proposed framework modularizes industrial processes in terms of the semantic information modules of physics in the real-world phenomena and adopts CAE tools to construct achievable digital physics models of industrial processes. The inter-module associations and near-real-time data processing in the modules are also clarified in the framework so that the phenomena distributed on separated sub-level physics models can be time-sensitive mutual supported for representing the real-world process comprehensively. The common characteristics for modeling industrial processes in this framework are identified and organized systematically via the advanced associative feature technology. Further, a feature-based digital model template has been established for the physics phenomena contained in the basic compositions of an industrial process.

In summary, this chapter describes the proposed framework from an overall perspective, which aims to the realization of the functions, multiple-view integration, and closed-loop optimization within a proposed feature-based digital model, inter-module associations for comprehensively describing a manufacturing process, and synchronization of physics phenomena. The validations of these functions will be elucidated in the following chapters respectively.

Chapter 4: Multiple-view Integration and Closed-loop Optimization

4.1 Chapter Overview

As described in Chapter 3, the proposed feature-based digital model is capable of not only mirroring the real-world physics phenomena on the virtual side but also providing some local services, like advice for its real twin. To achieve this goal, the partial feature concepts in Chapter 3 are implemented to realize a multiple-view integration with a closed-loop optimization mechanism, which can significantly enhance the automatization for solving engineering problems. The engineering intents from the optimization view drive the CAE analysis and receive outputs from it as the feedback loop. To validate this mechanism, HVOF thermal spraying is used as an example. It is worth noting that CFD, as an important branch of CAE, is used in the analysis stage for understanding the main physicochemical phenomena involved in this chapter. Due to the similar computation mechanism, the main associations in the proposed feature-based integration environment are not affected.

High-velocity oxygen-fuel (HVOF) thermal spraying is an advanced thermal spraying technology involving a controlled complex physicochemical phenomenon process with parameters. Optimizing the process while considering interwoven multidisciplinary aspects is a non-trivial research challenge. To overcome the two existing challenges in the optimization of the HVOF process, the low generalization capacity and the lack of the integration of optimization methodology, this work in this chapter establishes a closed-loop and optimization-driven model for the HVOF process from a multi-view approach, integrating CAD (computer-aided design), CFD analysis and optimization views. Based on the progressive HVOF numerical modeling development, the proposed model adopts a new idea to optimize the spray coating by controlling the in-flight behavior of the gas-particle jet. Thus, this proposed model is able to enhance the simple parametric analysis in the previous numerical studies to a higher level with systematic optimization so that the traditional numerical modeling can generate a positive impact on the real process. At the core, advanced feature technology [8] was used to guide the realization of seamless information transfer among CAD, CFD, and optimization views by allowing associations among them, which supports the optimization-driven mechanism. Besides, advanced feature technology was used to model the semantic entities involved in the modeling architecture of the virtual process so that the multi-view integration can support spray system configurations for various industrial HVOF processes and provide a high generalization capacity.

To validate the modeling method, an actual HVOF spray system depositing WC-12Co coating was modeled. The optimal process parameters generated by the model were implemented in the HVOF spray system, and its coating properties were tested experimentally to verify the model effectiveness.

4.2 Conceptual Model of the HVOF Coating Optimization

The coating formation process consists of stages of splatting molten or semi-molten particles, sintering of the deposited particles onto the substrate, solidification, and deformation. Ideally, the in-flight particles are heated to a semi-molten state. When the particles hit a substrate, the sudden deceleration causes a pressure build-up at the particle-substrate interface. The high energy inside the particles forces the molten material to flow laterally or the ductile solid material to deform. The liquid bonding material spreads outward from the point of impact and forms a splat [67]. According to the studies of the coating formation mechanism [66,67], the mechanical properties of the spray coating are significantly affected by the physical and chemical states of the in-flight particles, such as velocity, temperature, degree of melting, and oxidant contents. The in-flight particle behavior, however, is coupled with the gas dynamics which are directly related to the operating parameters, such as the gas flow rate, the fuel/oxygen ratio, spray distance, and other various operational conditions, like the spray system used and the fuel/oxidant types [80]. That means the coating properties can be controlled indirectly by the operating parameters via the states of the in-flight particles.

Figure 4.1 presents a conceptual model and the predominant steps of the proposed optimization strategy by integrating CAD/CFD/Optimization. The conceptual model consists of two stages, numerical model construction and optimization process. For providing reasonable generality and high fidelity of the real world, the numerical model has been constructed with due regard to real system specifications, coating requirements, and working conditions in diverse scenarios. The rules associating with the real operational conditions and the numerical model setup parameters have been established and detailed, which makes the model easy to apply in different cases using HVOF technology. The detailed association rules are given and explained in Section 4.3.

In the process optimization stage, optimization intents are identified corresponding to the scales of the in-flight particle properties and/or other engineering intents (e.g., cost). For example, the cost could be added as an objective by calculating the total gas flow rate. Then the cost objective can be optimized to achieve an energy-efficient spray process. The specifications typically describe the operations of the system, like operating parameters and their ranges. In the optimization view of Figure 4.1, the operating parameters define the variables of the design of experiments (DOE) [105], and their ranges are used for the design matrix generation and further determine a feasible region for the optimization process. An example optimization model is given in Section 4.6.1, which shows the implementation of a case study. The substrate properties, particle properties, and working conditions (e.g., working space) could be further modeled as constraints. For example, the in-flight particle temperature of small particles could be added as a constrain to strictly avoid overheating. In most real HVOF systems, the operating parameters are fuel, oxygen, nitrogen gas flow rate, particle feedback rate, and spray distance [67,71]. Thus, the proposed optimization strategy works on these commonly used parameters to improve the coating quality. As the coating performance is usually influenced by multiple in-flight properties of the particles, the multi-response surface (MRS) [105] is used to model the mathematical relationships between the common operating parameters and the in-flight properties of the particles. Further, desirability functions [10] are carried out to construct a single objective function for accommodating these properties and reaching the best in-flight state of the particles. During the construction of the desirability functions, the information mapping consistency between coating requirements and the optimization intents is crucial for ensuring the model is reusable, for which specific knowledge and rich experience are required and formally captured. Besides, to create an effective testing design space, the design of experiment (DOE) [105] approach is adopted for design /response variable validation. Finally, by implementing the optimization method, the ideal operating parameters are calculated subject to predefined optimization intents. It is worth mentioning that this model conceptually presents potential factors as many as possible which may not be completely considered in the case study of this work. However, in the future, these potential factors could be implemented by following this verified model template.

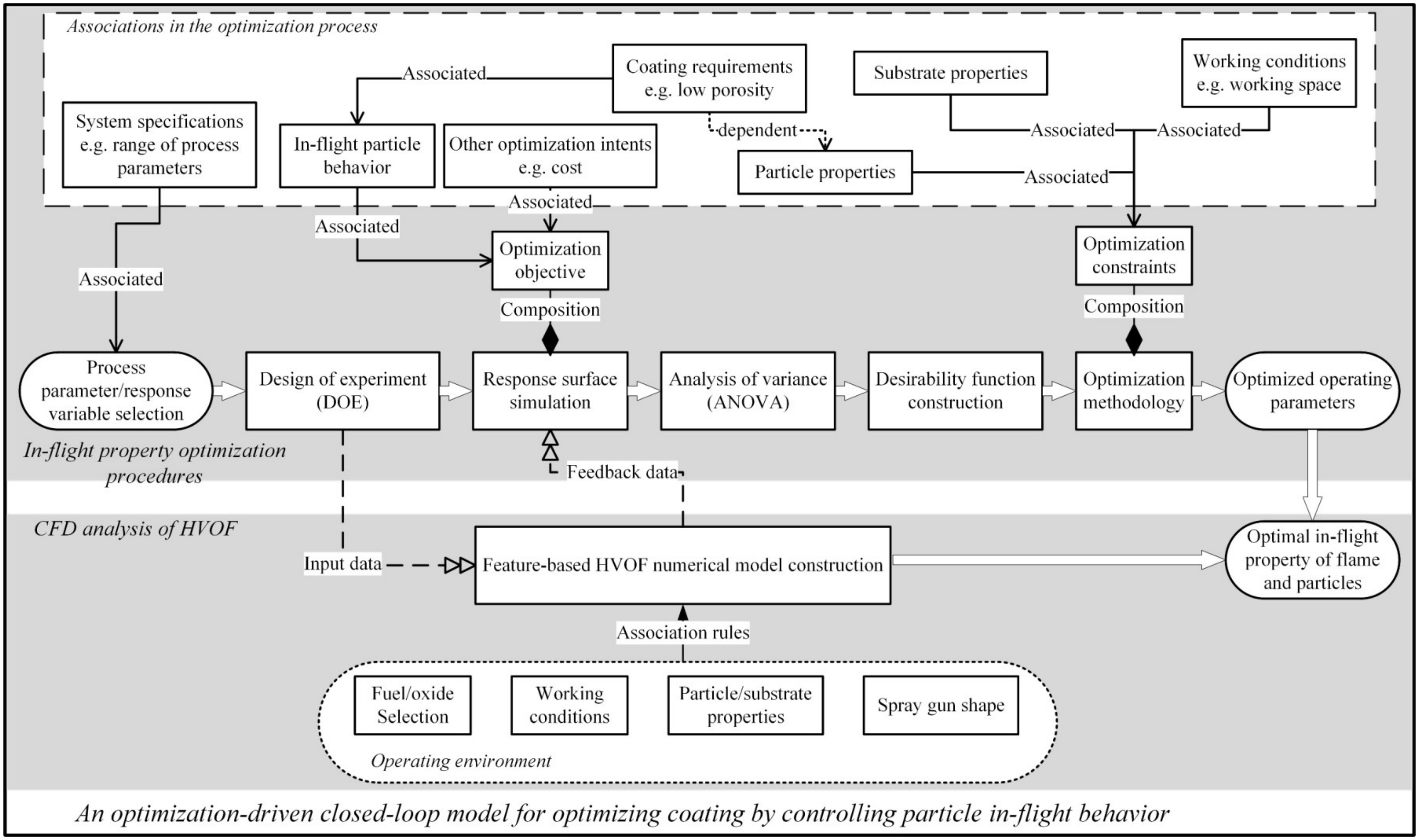

Figure 4.1 Conceptual model of the HVOF coating optimization

4.3 Feature-based Data Model for the In-flight Behavior in HVOF processes

4.3.1 Associations in the feature-based CAD/CFD Integration

Implementing the idea outlined above requires a persistent domain integration solution so that the information transmission mapping among different domains can be resolved. The integration needs to respect two aspects: automating the model construction and maintaining the engineering information mapping consistency. Although both aspects have been extensively studied in different areas, a mature integration solution for industrial processes with complex physicochemical phenomena is still not available. In light of the complexity of the HVOF process, a multiple-view integration method for HVOF processes is proposed by expanding the proposed features introduced in Section 3.4 into a multiple-view framework following the Unified Modeling Language (UML) convention [106], which is depicted in Figure 4.2. This figure supports the conceptual model shown in Figure 4.1 and illustrates the interdisciplinary views and entities involved. The components are abstracted as class levels with standardized attributes; by doing so, the model structure can be well organized and reusable according to an object-oriented approach. Such a class structure supports the construction of the associations among different views. This section explains some instances of the feature concepts in Section 3.4 for the specific process of HVOF thermal spraying and describes the association mechanism among them.

This chapter focuses on providing a unified model compatible with different HVOF spray guns, and the CFD model is intended to be created and maintained likewise to achieve feature-based CAD/CFD integration. In the proposed model structure shown in Figure 4.2, the following feature instances are introduced conceptually: HVOF nozzle CAD functional feature, CFD boundary feature, HVOF physicochemical feature, HVOF gas dynamics feature, HVOF in-flight particle feature, HVOF process optimization feature, and coating feature. Among those defined feature instances, their information entities are clustered and managed as functional views (modules) while at a lower level, the detailed parameters are associated, and the mapping relations are further illustrated in Figure 4.3. All the attributes and their values are organized and store into a common data model [9] named "HVOF coating system specifications" (non-geometric information) and permanently stored as a data file periodically by the user. During the run time, these entities in Figures 4.2 and 4.3 are associated.

Looking into the CAD/CFD integration view of Figure 4.2, the *HVOF nozzle CAD functional feature* of the HVOF system*,* as an instance of the *CAD functional feature* [60] for HVOF processes, is composed of a spray gun geometry model, functional fluid geometry, functional elements, controlling parameters. The HVOF computational domain of the combustion and flame is determined by incorporating the *HVOF nozzle CAD functional feature* module, such as spray gun geometry, functional elements, and fluid geometry [64], and the control parameters (associated with process parameters), such as of the *spray distance*. Note process parameters are extracted from the process optimization module and mapped as control parameters in the CAD functional feature. To achieve closed-loop virtual CFD physics simulation with flexible applications, the frequent yet robust information flow and interactions between CAD models and CFD setups are necessary. To conduct a set of systematic simulation scenarios as per DOE methodology, the HVOF CFD models can be automatically generated or updated through its input interface, where the input parameter values of CAD models and process parameters are generated from the DOE scenario testing matrix.

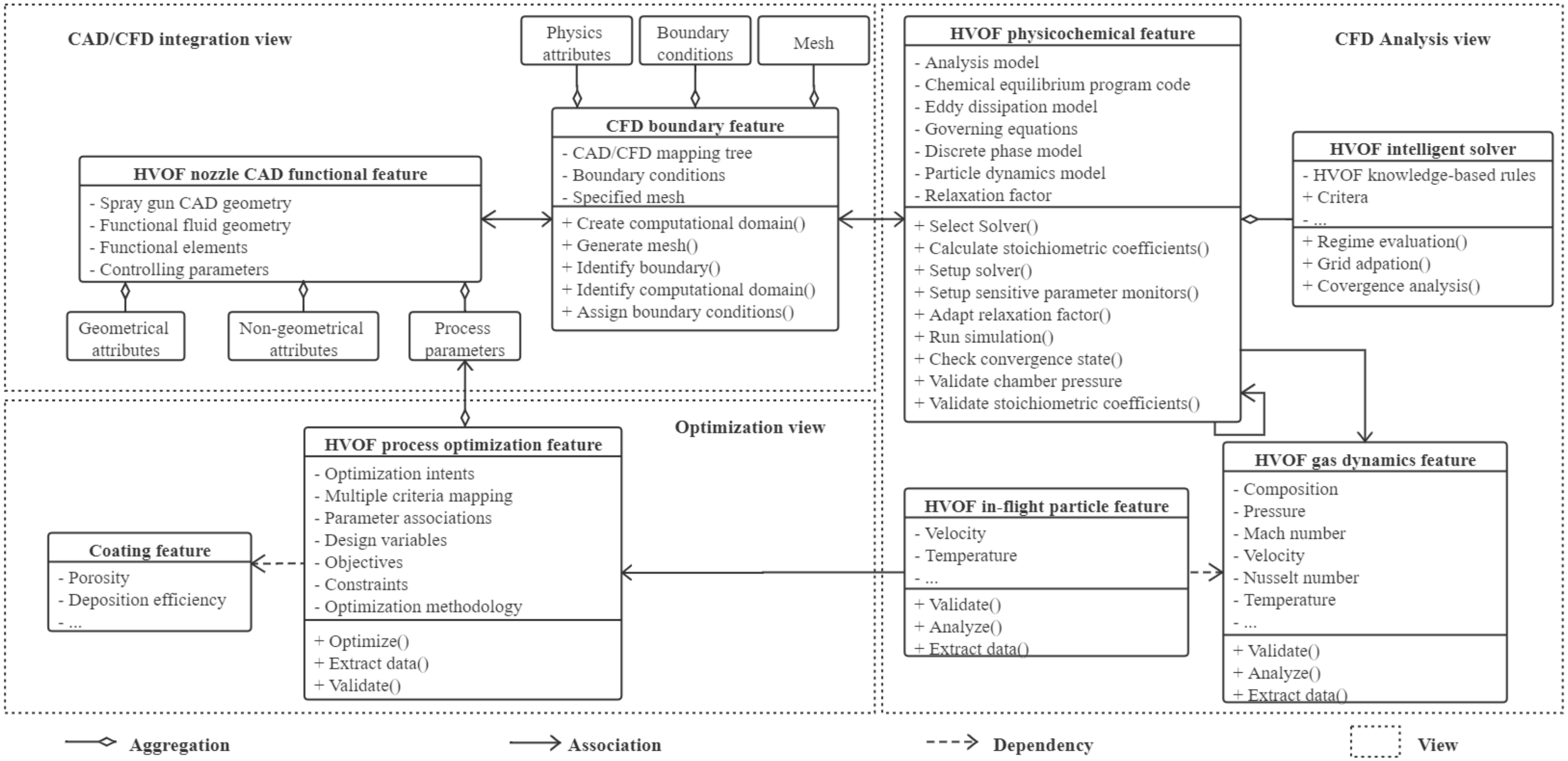

Figure 4.2 UML model representing inter-feature associations in the feature-based digital model for the in-flight behavior in HVOF processes.

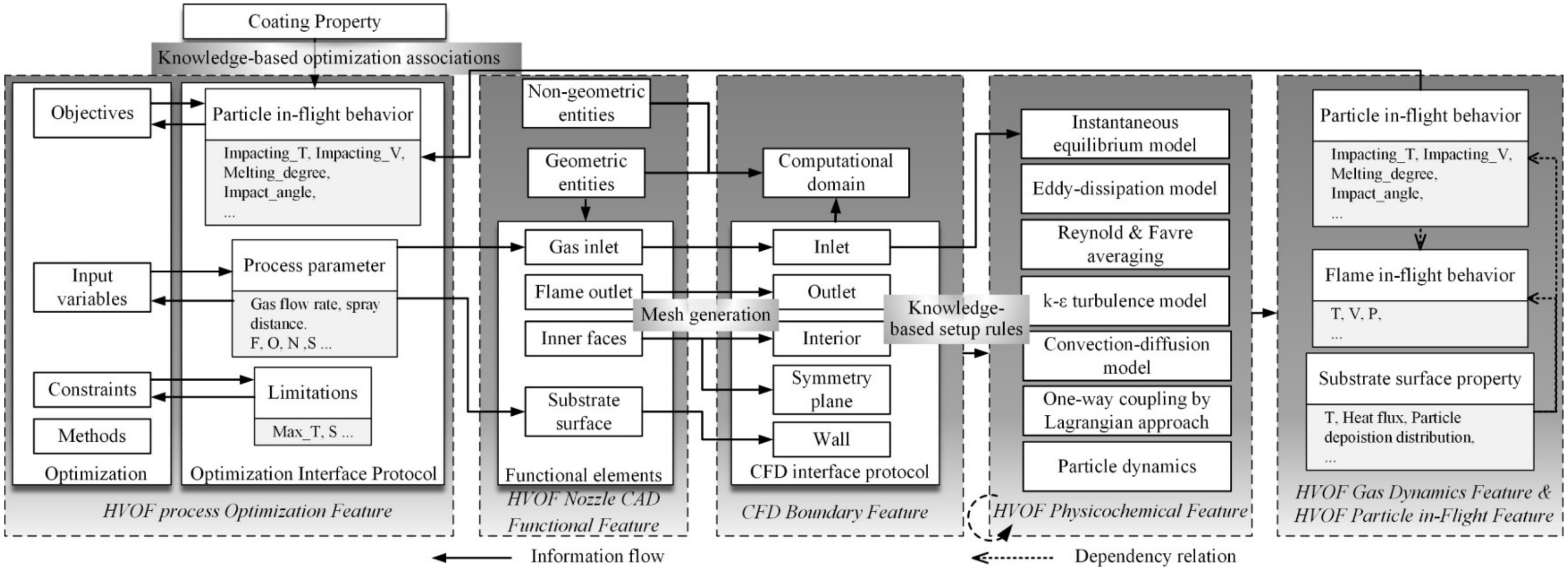

Figure 4.3 Partial associations in the proposed feature-based digital model for the in-flight behavior in HVOF processes.

The detailed associations among multiple-view features are shown in Figure 4.3. The aforementioned system specifications define the material and the cooling method of the chamber wall, as well as the range of each process parameter, which is recognized and used in the optimization view to generate a design space. For example, the parameters of spray distance defined in the *optimization interface protocol* are associated with the target substrate surface position in the *functional elements* of the HVOF nozzle CAD functional Feature.

Next, as shown in the *CFD Boundary Feature* of Figure 4.3, a parametrized computational domain with CFD-specific knowledge can be established via CAD geometry extraction and meshing operations. This CFD boundary feature has been defined as a specific one of the CAE boundary features for the field of CFD. It contains the mapping relations of geometrical dependencies between CAD entities and their associated CFD mesh representations as well as non-geometrical dependencies [62]. As an example, the process functional geometry defined in the *computational domain* can be itemized as symmetry planes/axes, gas/particle inlets, inner faces enclosing fluid space, and flame outlet.

Then, to systematically set up the simulation, *HVOF physicochemical feature,* as an instance of the *physics feature*, is proposed as shown in Figure 4.2 and defined to contain a series of candidate CFD-solving models for simulating the physicochemical phenomenon. Because the HVOF physicochemical feature is designed to compute physicochemical phenomena during the process, the related modeling parameters and the corresponding governing equations are defined as attributes and constraints separately. Through investigating previous research efforts, the related CFD models and the corresponding governing equations attached in the HVOF physicochemical feature are further explained in Appendix 1. However, a robust simulation requires not only reasonable model selections but also complicated solver setups that should correspond to actual operational conditions. Thus, the *HVOF intelligent solver feature* aggregated into the HVOF physicochemical feature contains a set of knowledge-based rules to determine the solver setup parameters and generate a stable CFD model, which will be elaborated in Section 4.4. Such rules will enhance the flexibility and intelligence of the numerical model.

When the computational domain is transferred to the HVOF physicochemical feature (a CFD environment) shown in Figure 4.3, its entities are recognized as the functional geometry input by using the mapping tree embedded in the CFD boundary feature. For the detailed interpretation of the mapping relations, the reader could refer to [64]. Consequently, a controllable input interface of the HVOF CFD solver, including parametrized geometry and boundary elements, can be established.

Finally, before the optimization view, the modular solvers corresponding to the different simulation models, e.g., instantaneous equilibrium model and eddy-dissipation model, will run to generate simulation results. These results are further clustered into two specific features from the concept of the phenomenon feature, the *HVOF gas dynamics feature* and the *HVOF in-flight particle feature* in the bottom-right corner of Figure 4.2, in which, the behaviors of the fuel-oxygen combustion gas dynamics and in-flight particles are established. The proposed features primarily work as an interface that enables phenomenon information generated from the simulation to become usable for the optimization view. In other words, after building a robust HVOF numerical model, all the physics behavior of the flame and particles could be exported from the simulation results to the downstream optimization view. Typical attributes describing the behavior of the flame and particle are indicated in Figure 4.2. Besides, it can be observed that between the in-flight particle behavior model and the flame gas behavior model, a "one-way dependency" symbol is used to reflect the physics reality.

4.3.2 Feature-based optimization process setup

In this subsection, Figure 4.2 is used again for demonstrating the feature-based optimization view setup. Under the aforementioned feature-based association mechanism, the inputs of the HVOF numerical model can be orderly and iteratively executed to search for the optimal in-flight particle properties and the corresponding process parameters. However, because of the large number of process parameters and their wide ranges, it is impractical to implement an exhaustive algorithm without an effective optimization methodology. Based on the associative feature concept, the *HVOF process optimization feature* is proposed here as an instance of the process optimization feature to implement the optimization process in the HVOF process systemically, shown in the lower-left corner of Figure 4.2.

HVOF process optimization feature contains optimization intent that is derived from manufacturing requirements, and optimization attributes, like design variables, constraints, optimization equations, and optimization algorithms. For example, a dense coating requirement can correspond to an optimization intent for reducing the particle 'side-spreading' (radial) velocity prior to the impact. To generate a process optimization feature model for a specific HVOF scenario, clear association rules are required to support the information transfer mechanism between the variables of the optimization process and entities of the feature-based CAD/CFD integration view. The optimization design variables are associated with the itemized functional geometries attached to the HVOF nozzle CAD functional feature, and the optimization response variables are derived from the manufacturing requirements which are in turn, associated with the corresponding in-flight particle properties. In this way, the optimization view can drive the CFD analysis and receive outputs from the CFD analysis view as the feedback loop. The optimization model according to the DOE matrix will be reflected as a series of the non-geometry attributes and functions that drive the CAD functional feature parameters for different scenarios. In turn, the *system specifications* defined in the common data model determine the optimization domain.

As the coating quality is controlled by the in-flight flame and particle properties, and their relationships are relatively tricky, constructing a fit-for-purpose model is crucial during the optimization process. To fill the gap, knowledge-based association reasoning is necessary. Some possible relationships have been summarized in Table 4.1, based on the currently available investigation results of pertinent literature. This table could be extended in the future with further research development of this area and new associations may appear. On the other hand, to obtain a high-quality coating, typically more than one key in-flight flame and particle property needs to be well controlled. Thus, as shown in Figure 4.2, multi-objective optimization is used here coupling constraints derived from manufacturing conditions which are abstracted as *coating feature* (which is a specific instance of the manufacturing feature). Finally, an optimization-driven, closed-loop, and multi-view model for HVOF process optimization is completed.

Table 4.1 Knowledge-based optimization associations for HVOF process optimization

Particle/gas in-flight property	Coating property	Potential decisions	Reference
Particle temperature (Melting degree)	Bonding strength Porosity Residual stress	The temperature should be controlled within a certain range to ensure particles with a molten or semi-molten state.	[67,68,72] [69,107] [107–109]
Particle velocity	Bonding strength Porosity Deposition efficiency	Higher particle velocity means more conversion of the particle kinetic energy into the coating formation.	[110] [69] [72,89]
Particle impact orientation	Deposition efficiency	For high deposition efficiency, an orientation perpendicular is expected.	[89,111]

4.4 Parametric-controlled Intelligent Solver

Coupled with the optimization process, the HVOF numerical model needs to be flexibly adjusted so that it is able to provide a fast response to the variations of the process parameters. Thus, a parameterized HVOF numerical modeling method is designed in this work. It starts from the commonly used process parameters and contains the process of computational domain determination, reaction formula calculation, solver setup, and convergence analysis, as shown in Figure 4.4.

Note that the computational domain is derived from the HVOF nozzle CAD functional feature by combining the geometric entities and the process parameters, such as the spray distance, and its functional attributes guide the mesh generation. The physics models for calculating the gas flow and particle behavior are set up according to the attributes of the HVOF physicochemical feature. The values of process parameters, like the gas flow rates, are assigned to boundary conditions via the association mechanism embedded in the CAD/CFD integration view. To integrate the information from the system specifications (a common data model) into the proposed model, it is worth noticing that the powder particles, such as their thermophysical properties and shape equivalent factors, and the substrate properties such as the material properties, are set accordingly as the setup conditions of the CFD model. Thus, these real factors are taken into consideration to obtain the corresponding particle behaviors which will be further applied in the optimization view to construct the response functions.

Typically, the HVOF process is fueled by hydrocarbon gases, like propylene, propane, and many others or hydrocarbon liquids as kerosene. Oxygen and compressed air (which is assumed to comprise oxygen and nitrogen only) are usually used as the oxidant. Thus, the process starts with fuel gas selection. When the combustion temperature reaches above 2000 K, the combustion of hydrocarbon gases is complex because the reaction products will be dissociated into a number of low-molecular species [112]. To model the combustion model accurately, the reaction is considered as the following form

$$n_1 C_\beta H_\gamma + n_2 O_2 \rightarrow n_3 CO + n_4 CO_2 + n_5 H + n_6 H_2 + n_7 H_2 O + n_8 O + n_9 OH + n_{10} O_2 \tag{4.1}$$

The stoichiometric coefficients can be calculated by using a chemical equilibrium code developed by Gordon and McBride [113]. After a reaction formula has been generated, the chemical reaction model can be completely set up by using the aforementioned analysis attributes of the HVOF physicochemical feature as discussed in Section 4.3.

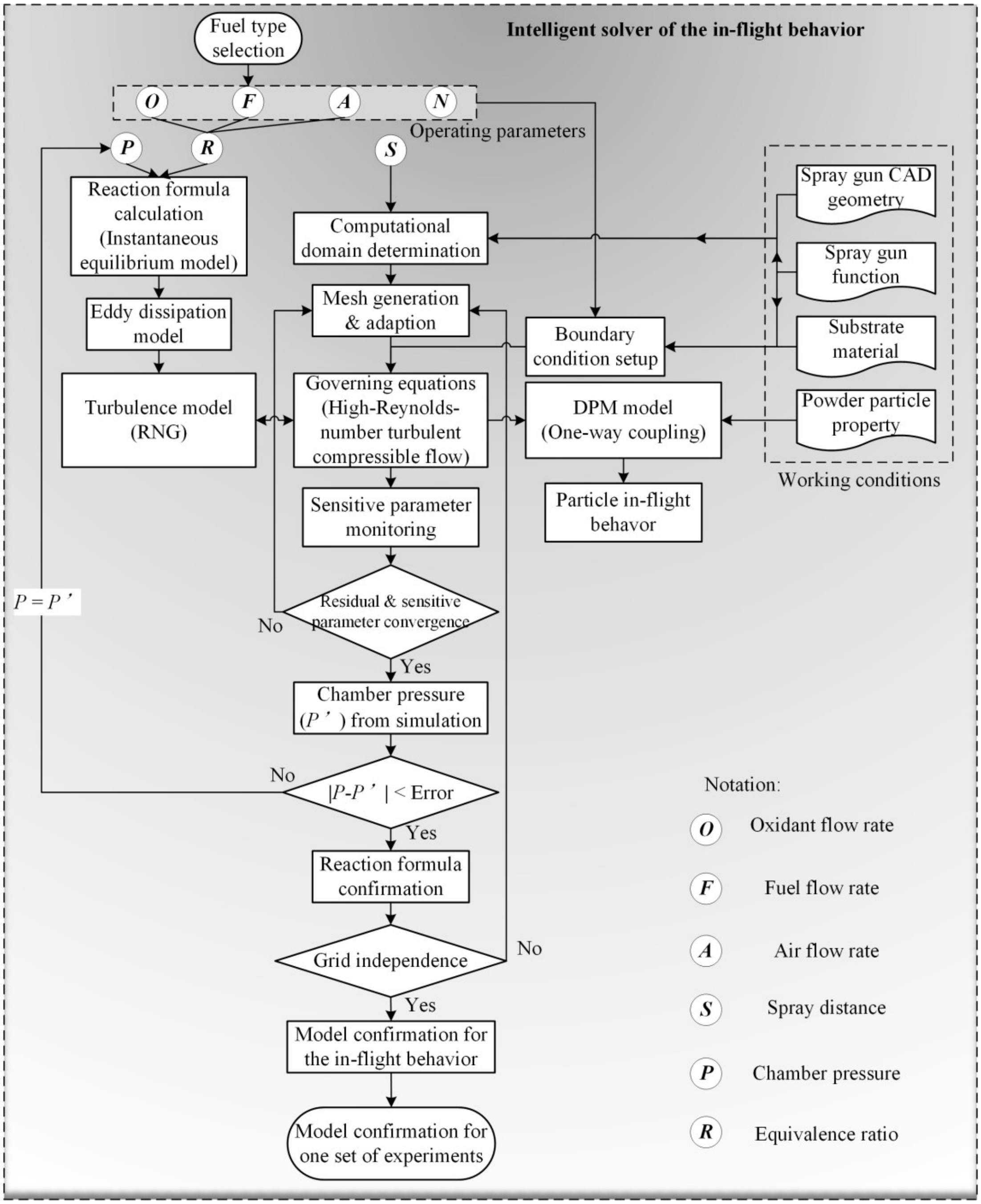

Figure 4.4 Parametrically-controlled intelligent solver for the in-flight behavior in HVOF processes

These stoichiometric coefficients rely on the equivalence ratio and combustion pressure P, and they are affected by the process parameters, e.g., the gas flow rate, or even the geometric entities of the spray gun. However, the stoichiometric coefficients and combustion pressure *P* are mutually dependent. Therefore, the chamber pressure *P* in Figure 4.4 will be assumed with a reasonable input initially to calculate the stoichiometric coefficients in Equation (4.1) and then carry out an initial simulation. The output of the CFD simulation will result in a new value of the *P* parameter, denoted as *P'*. Then when the difference between *P* and *P'* is larger than acceptable tolerance, *P'* value replaces the original assumption *P* value and reiterates the CFD simulation until their difference is small enough to be accepted.

For obtaining a convergent simulation, the last step of the solver setup is to construct the simulation solution monitoring conditions to check the convergence state with iterations. Typically, the solution convergence checking looks into the important physics properties and integral quantities which should be evolved to stable ranges of allowed tolerances. When the simulation encounters non-convergence problems, mesh grid adaption will be triggered. The local mesh may be adjusted so that simulation nodes are increased. If the simulation still has the non-convergence problem or is oscillating after several mesh rounds of adjustment, the under-relaxation factors have to be prudently reduced to increase the solution stability, although this is not recommended. After obtaining a convergent solution, grid independence verification will be conducted to further check the stability and accuracy. This step can be completed by inspection of plotting the sensitive parameters against the number of nodes [114], or an estimation of the order *p* of the discretization scheme [115]:

$$p \approx \frac{\log\left(\frac{\phi_{\Delta x_2}-\phi_{\Delta x_1}}{\phi_{\Delta x_3}-\phi_{\Delta x_2}}\right)}{\log(\alpha)} \text{ where } \alpha = \frac{\Delta x_1}{\Delta x_2} = \frac{\Delta x_2}{\Delta x_3} \tag{4.2}$$

where Δx_1, Δx_2, and Δx_3 are three grid levels, represented by the grid spacing; α is the refinement rate, and $\phi_{\Delta x1}$, $\phi_{\Delta x2}$, and $\phi_{\Delta x3}$ are the characteristic parameters corresponding to the three grid levels. Grid independence is achieved if p is in the range of 0 to 2.

So far, all the steps for systematically generating a robust numerical model are described as a sequential solution in Figure 4.4, which is defined as a simulation setup template for a number of simulations required by the optimization view.

4.5 Optimization Methodology

4.5.1 Response surface method

In order to correlate the process parameters and in-flight particle characteristics, statistical techniques are developed based on the feature-based optimization view concept as shown in Figure 4.2 with the associated functional attributes of the HVOF nozzle CAD functional feature. Some widely used statistical techniques include the kriging method, the radial basis function (RBF)-based method [116], and the response surface method (RSM), where the RBF-based and kriging methods are more suitable for exploring highly nonlinear problems, but the RSM fits better for engineering problems with a small group of input variables and a low-degree polynomial function [64]. In this case, RSM is used to model the empirical relationships between the in-flight particle properties and the converted design variables. The relationship type is explained by using a second-order polynomial equation

$$Y = \beta_o + \sum_{i=1}^{k} \beta_i x_i + \sum_{i=1}^{k} \beta_{ii} x_i^2 + \sum_{1 \le i \le j}^{k} \beta_{ij} x_i x_j + \varepsilon \tag{4.3}$$

where Y is the predicted response, β_o is the interception coefficient, β_i is the linear coefficient, β_{ii} is the quadratic coefficient, β_{ij} is the interaction coefficient, k is the number of input variables, and ε is the error.

To provide a systematic and revealing optimization model without a great deal of data to support the original hypotheses, the RSM must establish a Design of Experiments (DOE) matrix [10]. Herein, a full-factorial Central Composite Design (CCD) [117] is adopted to generate scaled design points. Those design points link with process parameters to drive the parametrically-controlled numerical model to obtain the correspondingly in-flight flame and particle properties. Then, the empirical relationships can be modeled.

After obtaining an initial response function, analysis of variance (ANOVA) technique [105] is carried out to identify the adequacy of the predictive model. Several criteria are used to assess the model, such as the coefficient of determination (R^2), probability value (p-value), Mean Absolute Error (MAE), and Root Mean Squared Error (RMSE). If the model has an unacceptable error, some additional design points will be generated and used as new inputs for the next round of regression analysis.

4.5.2 Basic desirability functions

Generally, more than one particle property needs to be well controlled to get a high-quality coating. Therefore, several response surfaces should be constructed and optimized simultaneously via the multi-response surface method with the desirability function approach proposed by Harrington (1980) [10]. As there are several response functions to optimize synchronously, each of the functions is transformed into a compromised “desirability” function corresponding to a type of optimization goal, such as the maximum, minimum, or target respectively shown in Equation (4.4) to (4.6). For obtaining an optimization solution compromising different response functions, an overall desirability function is measured by the geometric mean as shown in Equation (4.7). All the transformed desirability responses are dimensionless variables that range from 0 to 1, where a high value indicates a desirable level and a low value is corresponding to an undesirable level.

$$d_r^{max} = \begin{cases} 0 & \text{if } f_r(\boldsymbol{X}) < A \\ \left(\frac{f_r(\boldsymbol{X})-A}{B-A}\right)^s & \text{if } A \leq\ f_r(\boldsymbol{X}) \leq B \\ 1 & \text{if } f_r(\boldsymbol{X}) > B \end{cases} \tag{4.4}$$

$$d_r^{min} = \begin{cases} 0 & \text{if } f_r(\boldsymbol{X}) > B \\ \left(\frac{f_r(\boldsymbol{X})-B}{A-B}\right)^s & \text{if } A \leq\ f_r(\boldsymbol{X}) \leq B \\ 1 & \text{if } f_r(\boldsymbol{X}) > A \end{cases} \tag{4.5}$$

$$d_r^{target} = \begin{cases} \left(\frac{f_r(\boldsymbol{X})-A}{t_0-A}\right)^{s_1} & \text{if } A \leq\ f_r(\boldsymbol{X}) \leq t_0 \\ \left(\frac{f_r(\boldsymbol{X})-B}{t_0-B}\right)^{s_2} & \text{if } t_0 \leq\ f_r(\boldsymbol{X}) \leq B \\ 0 & \text{otherwise} \end{cases} \tag{4.6}$$

$$D = \left(\prod_{r=1}^{R} d_r\right)^{1/R} \tag{4.7}$$

In the equations above, A and B are limit values and t_0 is the target value. The exponent s determines the importance of achieving the desired value (A, B or t_0). $\boldsymbol{X}$ is the design variable matrix and f_r is the model generated by RSM.

4.6 Case Study

4.6.1 Implementation of the feature-based model

The process of splat formation is an important phase of coating deposition that determines both the microstructural and macroscopic characteristics of the coating. This process strongly depends on the state of the particles prior to their impact on the substrate. Generally, higher particle velocity means more conversion of the particle kinetic energy into the work of viscous deformation and surface energy during the transient impact. Moderate particle temperature can prevent powder particles from superheating or vaporization and simultaneously decreases the dynamic viscosity of the molten bonding material to some extent, which protects the material properties of the powder particles and facilitates the liquid bonding material to spread outward from the point of impact.

Thus, optimum particle temperature together with a high particle velocity can significantly improve the microstructural and macroscopic characteristics of the coating.

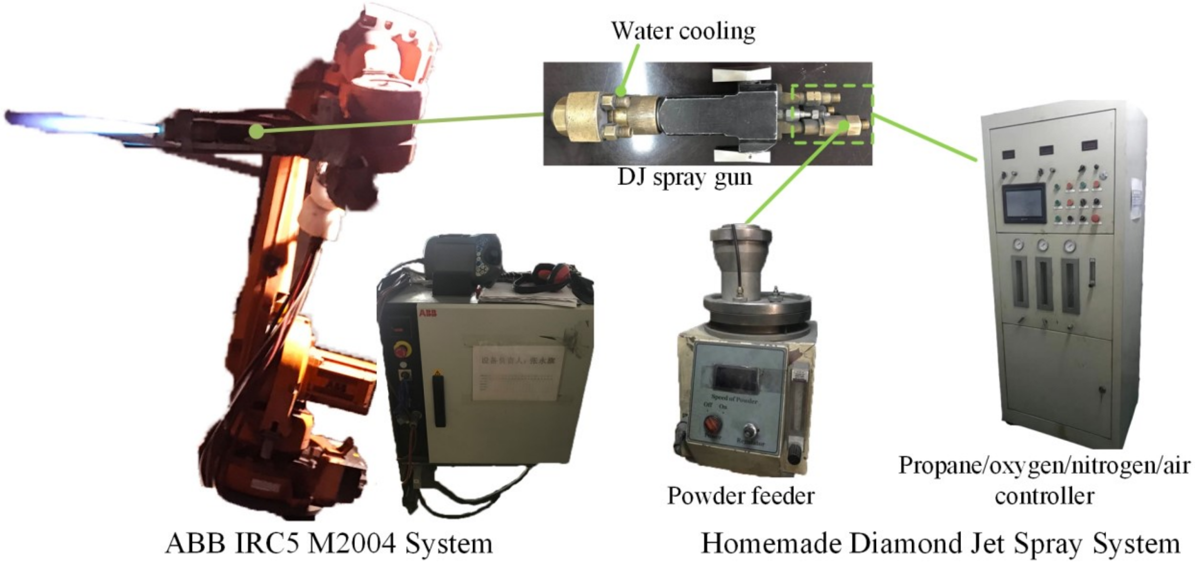

Figure 4.5 A homemade Diamond Jet spray system.

Based on the above analysis, in this subsection, the proposed feature-based model is used to optimize the velocity and temperature of the particles prior to their impact on the substrate within an operating environment that was based on a homemade Diamond Jet HVOF spray system and an ABB IRC5 M2004 robot system, as shown in Figure 4.5. More detailed features and parameters of the spray gun are available in Figure 4.6. Five crucial process parameters, i.e., oxygen, fuel, air, and nitrogen flow rates and spray distance, were selected for this purpose. Spray angle was kept constant (perpendicular to the substrate) during the simulation and experimental verification.

To validate the modeling method, WC-12Co powder with an 11.63-μm volume median diameter was used in this case, and the in-flight particle behavior was calculated with ANSYS Fluent as the solver; the particle size distribution and thermophysical properties are given in Table 4.2 [118]. Driven by the optimization intent, the optimal process parameters were obtained by the

HVOF model. The characteristics of the deposited coating were tested experimentally. The tested results verify the effectiveness of the proposed model.

Table 4.2 Particle size and thermophysical properties of WC-12%Co particles [118].

Density (kg/m^3)	14320
Specific heat (J/kg K)	295
Latent heat of fusion (10^6 J/kg)	0.42
Melting point (K)	1523.15
Surface emissivity	0.4
d_{10} (μm)	8.35
d_{50} (μm)	11.63
d_{90} (μm)	16.12

In the Diamond Jet spray system, the premixed fuel gas (propane) and oxygen are fed into a combustion chamber, where they react to produce high-temperature combustion gases. The exhaust gases together with the air injected from the annular inlet orifice expand through the nozzle to reach supersonic velocity. Nitrogen gas carrying powder particles is injected into the nozzle at the central inlet orifice. Table 4.3 indicates the system specifications and partial associations among the multiple views. Oxygen-propane combustion is used in this system.

Table 4.3 Partial system specifications and associations among the multiple views

System specifications			HVOF Process optimization feature	HVOF nozzle CAD functional feature	CFD boundary feature	HVOF physicochemical feature
Item	Unit	Description/Range	Process parameter	Functional element	Boundary condition	Solver setup parameter
Fuel type	—	Propane	—	—	—	Fuel selection
Fuel flow rate	SLPM	100~200	Fuel flow rate	Fuel & inlet	Flow inlet	Flow rate
Oxygen flow rate	SLPM	550~650	Oxygen flow rate	Oxygen & inlet	Flow inlet	Flow rate
Nitrogen flow rate	SLPM	76~116	Nitrogen flow rate	Nitrogen flow inlet	Flow inlet	Flow rate
Airflow rate	SLPM	475~675	Airflow rate	Airflow inlet	Flow inlet	Flow rate
Spray distance	mm	120~200	Spray distance	External flow length	Computational domain	—

Figure 4.6 illustrates the feature conversion in the CAD/CFD integration view and the CFD analysis view. The functional geometry which has been itemized as functional elements is shown in Figure 4.6(a). Figure 4.6(b) shows the crucial geometric information that was acquired from the direct measurement of the spray gun. Following feature conversion in the CAD/CFD integration, the parametrically-controlled CFD boundaries of the domain were tagged and associated with the corresponding design variables of the multi-objective optimization feature via the functional elements attached to the CAD functional feature, as shown in Figure 4.6(c). Besides, the physical attributes attached to the tags were used to guide the mesh generation as shown in Figure 4.6(d). Figure 4.6(e) and (f) present the temperature and velocity contours of the flame flow with a set of

process parameters (refer to case DP43 in Appendix 2), which is a visual representation of the HVOF gas dynamics feature. Figure 4.6(g) and (h) plot the temperature and velocity of the particle along the centerline of the spray gun with the same process parameters, which is a visual representation of the HVOF in-flight particle feature.

To illustrate the proposed HVOF numerical modeling, here, case DP43 in Appendix 2 is used as a sample to explain the procedure for generating a robust HVOF model. Regarding other experimental points, the computational domain and setup parameters can be easily updated subject to changes in the attribute value of the HVOF nozzle CAD functional feature by using the Configuration Manager provided in ANSYS Workbench. The number of cells, in this case, is 157,688. This case was set up in the feature-based template, thus the boundary conditions were set up according to the feature conversion as shown in Figure 4.6(a) and (c). As to the gas flow inlets (air, nitrogen, propane & oxygen) indicated in Figure 4.6(a), the boundary condition of the mass flow inlet was used for describing the flow rate. In the external flow field, the radial extent of the computational domain is chosen to be 50 mm which is much wider than the throat radius. The pressure outlet condition and wall condition were respectively specified to the outer boundaries and the substrate, as shown in Figure 4.6(c) [81]. For respecting the computational time and convergence problems, a temperature boundary for the substrate surface and the chamber wall was set up as a constant temperature of 300 K. Although it may change with the spray process, the variation in the temperature is small when compared with the temperature of the adjacent flame. After obtaining a stable simulation of the flame jet, the values given in Table 4.2 were correspondingly assigned to the setup parameters for the DPM. It is worth noting that the particle diameter was approximately assumed to be 10 μm with the shape factor of 1, because about 80% of the powder particles were around 10 μm.

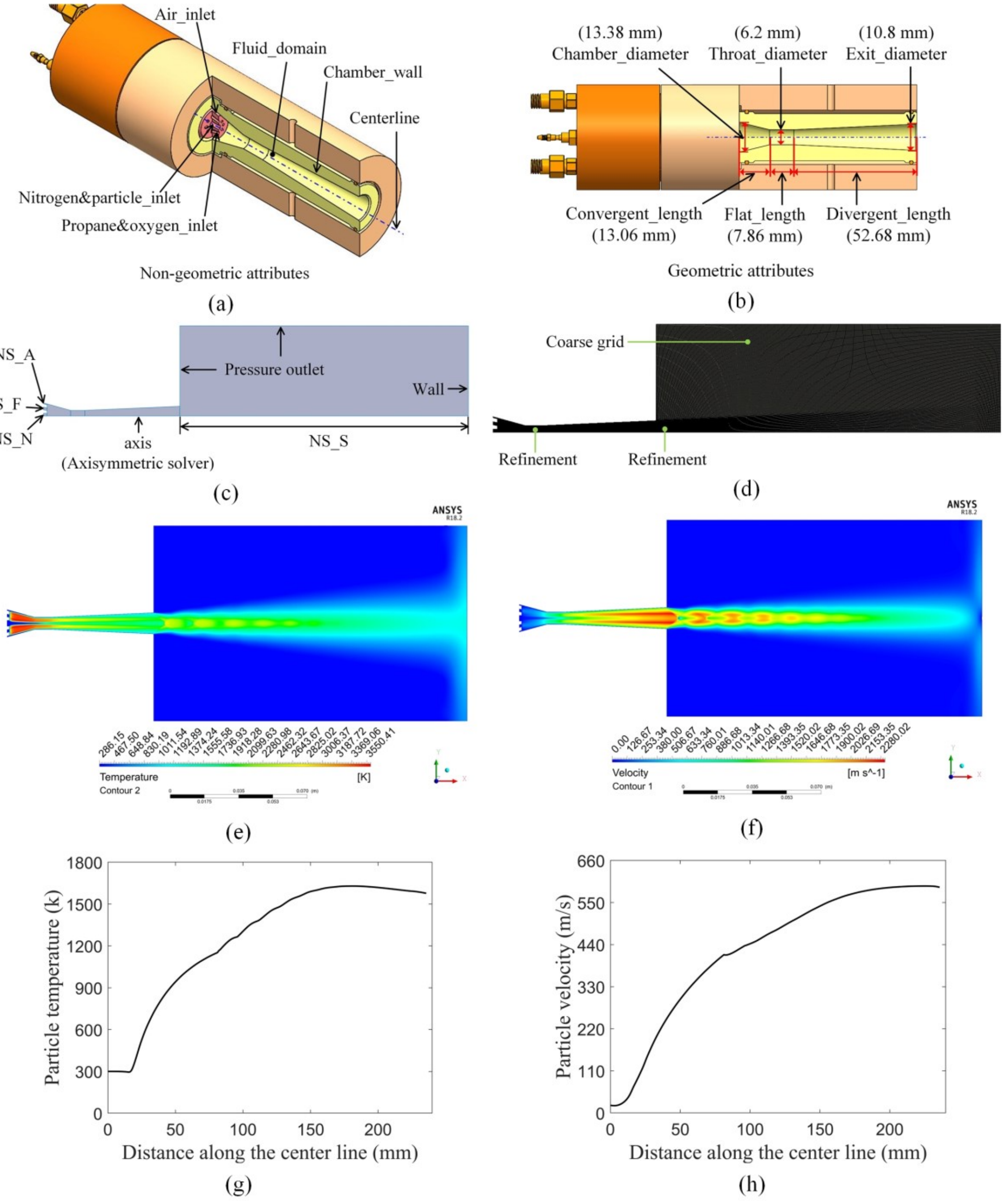

Non-geometric attributes

(a)

Geometric attributes

(b)

(c)

(d)

(e)

(f)

(g)

(h)

Figure 4.6 Schematic representation of the feature conversion in the CAD/CFD integration view and analysis view: (a) partial sectional view of the spray gun CAD model with non-geometric attributes; (b) the front view of the spray gun CAD model with geometric attributes; (c) parametrized CFD boundaries of the domain; (d) mesh generation; (e) temperature contour of the flame flow; (f) velocity contour of the flame flow; (g) particle temperature along the centerline of the spray gun; and (h) particle velocity along the centerline of the spray gun

The parameter monitors of the chamber pressure and heat flux integral quantity on the substrate surface were set up in the CFD session to check the convergence and stability of the simulation. 7-bar chamber pressure was presumed to get a starting point for the combustion. As shown in Table 4.4, the formula coefficient error in the last two iterations is quite small and can be ignored, thus the reaction formula was determined via several iterations.

Table 4.4 Reaction formula determination for the center point simulation.

Iteration No.	Presumed pressure	Reaction formula	Simulation pressure
1	7.0 bar	$C_3H_8 + 4.786O_2 \rightarrow 1.769CO + 1.222CO_2 + 0.333H + 0.513H_2 + 2.88H_2O + 0.308O + 0.855OH + 0.658O_2$	6.5 bar
2	6.5 bar	$C_3H_8 + 4.791O_2 \rightarrow 1.769CO + 1.222CO_2 + 0.342H + 0.521H_2 + 2.872H_2O + 0.308O + 0.855OH + 0.667O_2$	6.6 bar
3 (Final)	6.6 bar	$C_3H_8 + 4.791O_2 \rightarrow 1.769CO + 1.222CO_2 + 0.342H + 0.521H_2 + 2.872H_2O + 0.308O + 0.855OH + 0.667O_2$	6.6 bar

After obtaining an acceptable reaction formula, the independence analysis was carried out to further check the stability of the simulation model. Three grids were systematically refined around the rate of 1.9, and the order p of 0.6 obtained by Equation (4.2) gives the confidence that the simulation results with 0.1 million nodes are no longer grid insensitive. So far, a robust simulation for a set of process parameters has been achieved. The log file recording the particle temperature and velocity along the centerline could be processed in the optimization view.

The optimization-driven mechanism needs a guaranteed HVOF numerical modeling, as well as a systematic optimization modeling to enable the coverage of all constraints and optimization objectives. Table 4.3 shows some system specifications of the minimum and maximum values that can be associated with different process parameters. Based on the mapping relations embedded in the process optimization feature, such associative information is converted into design variables and parametric relations (expressions) at the experimental design level feeding the values of the parameters for the RSM, as shown in Table 4.5. To provide accurate predication models without a great deal of data to support the regression theory, the RSM uses an experimental design matrix of full-factorial Central Composite Design (CCC) with the five selected factors, which consists of 32 sets of factorial experimental design, 10 sets of star point and two sets of center points as shown in Appendix 2.

Table 4.5 The experimental design levels of the independent variables.

Design variables	Notation	Unit	Levels				
			-2.3784	-1	0	1	2.3784
Fuel (propane) flow rate	F	SLPM	100	128.977	150	171.023	200
Oxygen flow rate	O	SLPM	550	578.977	600	621.023	650
Nitrogen flow rate	N	SLPM	20	37.386	50	62.614	80
Air flow rate	A	SLPM	475	532.955	575	617.045	675
Spray distance	S	mm	120	143.182	160	176.818	200

The particle behavior prior to impact on the substrate shown in Appendix 2 was extracted from the log file recording the simulation results, which was used to fit regression models for the velocity and temperature in the optimization view. Second-order polynomial models were constructed for each response in the following forms:

$$
\begin{aligned}
y_1 = 589.2775 &+ 10.2914F + 6.8826O - 4.4622N + 2.2645A - 1.7666S + 2.327FO \\
&+ 0.1866FN - 1.6777FA + 0.1897FS - 0.4111ON + 0.2947OA \\
&+ 0.1882OS - 0.4657NA + 0.1519NS + 0.0045\,AS - 3.4752F^2 \\
&- 0.4366O^2 + 0.5382N^2 - 0.4312A^2 - 0.9582S^2
\end{aligned}
\tag{4.8}
$$

$$
\begin{aligned}
y_2 = 1508.288 &- 1.4387F + 13.54O - 49.083N - 8.3512A - 25.9316S + 8.64FO \\
&+ 2.2131FN - 0.5588FA + 3.3769FS - 1.0738ON - 3.7519OA \\
&- 1.665OS + 2.2863NA + 1.6819NS + 2.8425AS - 12.9867F^2 \\
&- 0.6733O^2 + 7.5336N^2 - 0.2985A^2 - 3.1756S^2
\end{aligned}
\tag{4.9}
$$

where y_1 is the particle velocity and y_2 is the particle temperature while F, O, N, A, and S are the design variables that represent the coded value shown in Table 4.5.

For checking the adequacy of the regression model, the ANOVA results for the particle velocity and temperature are presented in Table 4.6 and Table 4.7. It is found that the regression models are adequate. In the tables, the Fisher ratio (F value) with a very low probability value (p-value) (1.0146e-13 for the particle velocity regression model and 1.3314e-12 for the temperature model) demonstrates the selected terms in the models are significant. The coefficient of determination (R^2) was calculated as 0.974 for the particle velocity (Table 4.6) and 0.967 for the particle temperature (Table 4.7), implying that the regression model can explain 97.4% of the variability in the velocity response and 96.7% of that in the temperature response. Additionally, Root Mean Squared Error (RMSE) and Mean Absolute Error (MAE) were calculated to be 3.1845 and 1.6699 for the velocity regression model, and 15.4258 and 7.7848 for the temperature regression model, which indicates that the prediction error of the two models is small and acceptable. Collectively, these results indicate the excellent capability of the regression models.

Table 4.6 ANOVA results for particle velocity

Variables	D_f	Sum of Sq.	Mean Square	F Value	p Value	Sig. Code
F	1	4587.5165	4587.5165	452.3614	< 0.0001	***
O	1	2051.7647	2051.7647	202.3184	< 0.0001	***
N	1	862.4397	862.4397	85.0426	< 0.0001	***
A	1	222.1031	222.1031	21.9009	0.0001	***
S	1	135.1803	135.1803	13.3297	0.0013	**
F*O	1	173.2731	173.2731	17.0859	0.0004	***
F*N	1	1.1142	1.1142	0.1099	0.7433	
F*A	1	90.0650	90.0650	8.8810	0.0067	**
F*S	1	1.1518	1.1518	0.1136	0.7392	
O*N	1	5.4079	5.4079	0.5333	0.4726	
O*A	1	2.7783	2.7783	0.2740	0.6057	
O*S	1	1.1329	1.1329	0.1117	0.7412	
N*A	1	6.9406	6.9406	0.6844	0.4166	
N*S	1	0.7384	0.7384	0.0728	0.7897	
A*S	1	0.0007	0.0007	0.0001	0.9936	
F^2	1	389.5398	389.5398	38.4114	< 0.0001	***
O^2	1	6.1493	6.1493	0.6064	0.4441	
N^2	1	9.3434	9.3434	0.9213	0.3471	
A^2	1	5.9983	5.9983	0.5915	0.4497	
S^2	1	29.6156	29.6156	2.9203	0.1009	
Residual	23	233.2491	10.1413	1.0000	0.5000	

$R^2 = 0.974$, Adjusted $R^2 = 0.952$, F value = 43.262, p value = $1.0146e^{-13}$, RMSE = 3.1845, MAE = 1.6699

D_f: Degrees of freedom; F value: Fisher ratio; p-value: Probability; R^2: Coefficient of determination; RMSE: Root Mean Squared Error; MAE: Mean Absolute Error. Significance code: '***' High; '**' Moderate; '*' Low.

Table 4.7 ANOVA results for particle temperature

Variables	D_f	Sum of Sq.	Mean Square	F Value	p Value	Sig. Code
F	1	89.6485	89.6485	0.3767	0.5454	
O	1	7940.7764	7940.7764	33.3711	< 0.0001	***
N	1	104348.7857	104348.7857	438.5254	< 0.0001	***
A	1	3020.7726	3020.7726	12.6948	0.0017	**
S	1	29126.1724	29126.1724	122.4026	< 0.0001	***
F*O	1	2388.7872	2388.7872	10.0389	0.0043	**
F*N	1	156.7335	156.7335	0.6587	0.4253	
F*A	1	9.9904	9.9904	0.0420	0.8395	
F*S	1	364.9051	364.9051	1.5335	0.2281	
O*N	1	36.8940	36.8940	0.1550	0.6974	
O*A	1	450.4501	450.4501	1.8930	0.1821	
O*S	1	88.7112	88.7112	0.3728	0.5475	
N*A	1	167.2621	167.2621	0.7029	0.4104	
N*S	1	90.5185	90.5185	0.3804	0.5434	
A*S	1	258.5538	258.5538	1.0866	0.3081	
F^2	1	5440.0186	5440.0186	22.8617	0.0001	***
O^2	1	14.6223	14.6223	0.0615	0.8064	
N^2	1	1830.6487	1830.6487	7.6933	0.0108	*
A^2	1	2.8746	2.8746	0.0121	0.9134	
S^2	1	325.2728	325.2728	1.3670	0.2543	
Residual	23	5472.9377	237.9538	1.0000	0.5000	

$R^2 = 0.967$, Adjusted $R^2 = 0.939$, F value = 34.18, p value = $1.3314e^{-12}$, RMSE = 15.4258, MAE = 7.7848

D_f: Degrees of freedom; F value: Fisher ratio; p-value: Probability; R^2: Coefficient of determination; RMSE: Root Mean Squared Error; MAE: Mean Absolute Error. Significance code: '***' High; '**' Moderate; '*' Low.

To intuitively indicate the effect of each design variable on responses, Figure 4.7 gives the prediction plots of interactions. The green lines show the response surface against a single design variable, with all other variables held fixed at the center point of the design space. The red curves indicate a 95% simultaneous confidence band for the fitted response surface. Apart from the intuitive contour results, the effect of design variables on the responses was quantitatively assessed by the F value and p value from the results of ANOVA, as shown in Table 4.6 and Table 4.7. From the results of ANOVA and the prediction plots of interactions, obviously, the velocity response is highly affected by the fuel flow rate and oxygen flow rate, and the temperature response is highly affected by the nitrogen flow rate and spray distance.

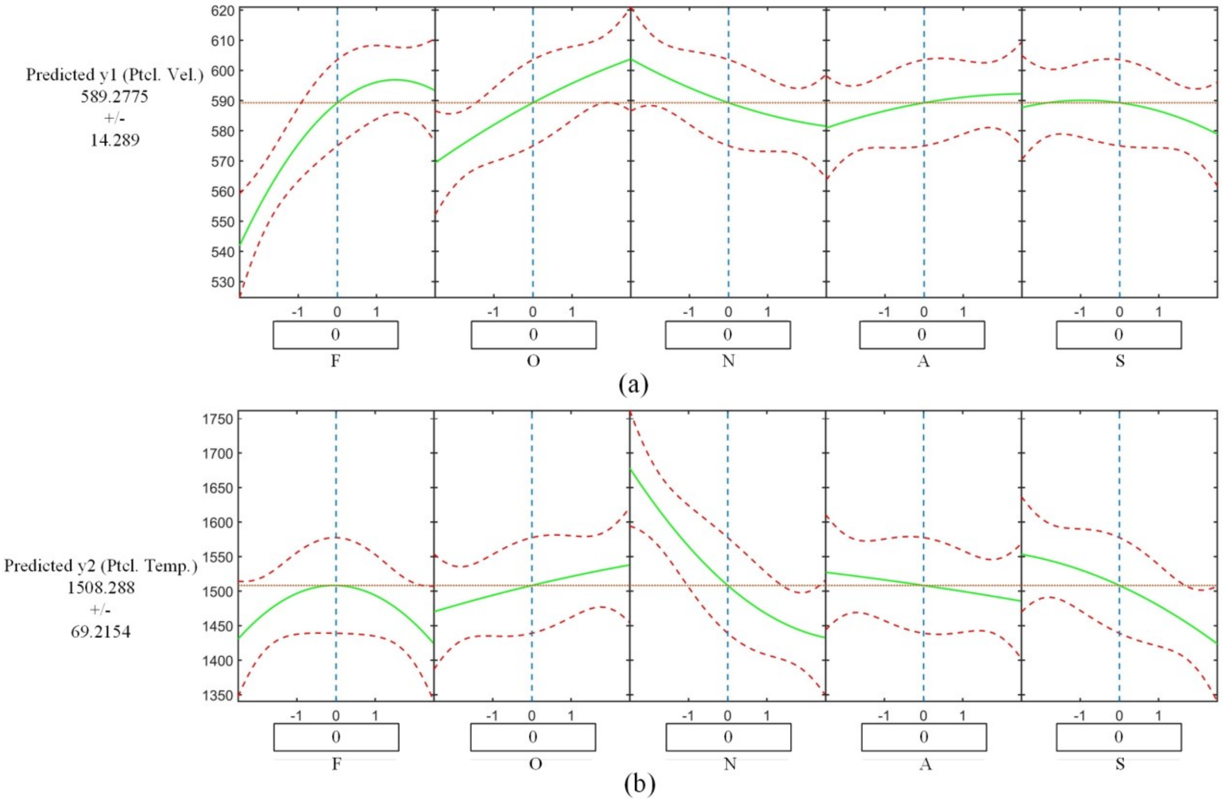

Figure 4.7 Influence of the design variables: (a) the velocity response, and (b) the temperature response.

In this case, the optimization process aimed to maximize the particle velocity and control the particle temperature around the melting point before their impacts on the substrate. Based on the optimization strategy introduced in Section 4.5, firstly, the obtained velocity response function (y1) and temperature response function (y2) were further transformed into a compromised "desirability" function respectively corresponding to a maximum goal and a target goal as shown in Equation (4.10) and (4.11), and then an overall desirability function, as shown in Equation (4.12), was constructed as the objective function by the geometric mean of the two "desirability" functions. The range of operation determines a feasible region for the optimization process. This feasible region is formulated as the constraint function.

$$d_1 = \begin{cases} 0 & if\ y_1 < V_{min} \\ \left(\dfrac{y_1 - V_{min}}{V_{max} - V_{min}}\right)^s & if\ V_{min} \leq\ y_1 \leq V_{max} \\ 1 & if\ y_1 > V_{max} \end{cases} \tag{4.10}$$

$$d_2 = \begin{cases} \left(\dfrac{y_2 - T_{min}}{T_{melting} - T_{min}}\right)^s & if\ T_{min} \leq\ y_2 < T_{melting} \\ \left(\dfrac{y_2 - T_{melting}}{T_{melting} - T_{max}}\right)^s & if\ T_{melting} \leq\ y_2 \leq T_{max} \\ 0 & otherwise \end{cases} \tag{4.11}$$

$$max.\quad D = (d_1 d_2)^{1/2} \tag{4.12}$$

$$st.\quad \begin{cases} -2.3784 \leq\ F \leq 2.3784 \\ -2.3784 \leq\ O \leq 2.3784 \\ -2.3784 \leq\ N \leq 2.3784 \\ -2.3784 \leq\ A \leq 2.3784 \\ -2.3784 \leq\ S \leq 2.3784 \end{cases} \tag{4.13}$$

In the equations above, y_1 and y_2 are the velocity response function (Equation (4.8)) and temperature response function (Equation (4.9)). V_{min} and V_{max} are the minimum value and maximum value of the velocity response (y1) from Table 6 respectively. T_{min} and T_{max} are the minimum value and maximum value of the temperature response (y2) from Appendix 2. $T_{melting}$ is the melting point of WC-12%Co particles shown in Table 4.2. F, O, N, A, and S are the design variables that represent fuel, oxygen, nitrogen, air gas flow rate, and spray distance respectively.

The optimization methodology was implemented by using a desirability function "*R*" package [119] with the Nelder-Mead simplex method [120]. Based on the associations indicated in Table 4.3, the real system specifications determined the ranges of the process parameters, which were further converted to the optimization process and formed a feasible region for implementing the optimization methodology. The optimization intents and results are shown in Table 4.8. The first two rows present the optimization objectives and the corresponding optimal values. The range of each particle property was estimated according to Appendix 2. Table 4.8 also shows the process parameter values for generating the optimal result. The overall desirability is 1, which indicates the optimal result satisfies the optimization intent. This set of parameter values was validated by simulation, and the simulation results of the particle velocity and temperature are respectively 611.293 m/s and 1534.08 K, which gives a relative error of 0.14% and 0.71%. Meanwhile, the equivalence ratio (1.209) at the optimal point is consistent with the conclusion given in [72], which indicates the validity of the optimal solution to a certain extent.

Table 4.8 Optimization result for specific optimization intent.

Variable	Optimization intent	Min.	Max.	Coded value	Actual value	Desirability
y_1 (m/s)	Max	550	610	610.420	610.420	1
y_2 (K)	Target (1523.15 K)	1200	1850	1523.150	1523.150	1
F (SLPM)	In range	100	200	1.455	180.596	1
O (SLPM)	In range	550	650	1.217	625.586	1
N (SLPM)	In range	20	80	-0.875	38.970	1
A (SLPM)	In range	475	675	0.070	577.924	1
S (mm)	In range	120	200	1.152	179.379	1
			Overall Desirability			1

4.6.2 Verification of the optimization result

For validating the model, the coating properties of porosity and deposition efficiency were tested by conducting the process parameters as suggested by the model. Further, three additional sets of experiments were conducted to verify the effectiveness of the optimization process. Two of them were conducted above and below the optimal parameter values, and one with random process parameters within the optimization space was conducted. The tested coating properties are presented in Table 4.9. Moreover, the coating structures were examined with a ZEISS Imager.A2m. It can clearly be seen from Table 4.9 and Figure 4.8 that the coating produced by the optimal parameters is dense, and has low porosity and high deposition efficiency. In Table 4.9, the experiment with Contrast 3 (random parameters) has a relatively higher deposition efficiency than the optimal one, this was caused by the low inertia of the small particles resulting in a rapid increase of the radial velocity with an increase in the spray distance. From these experimental results, it can be inferred that a high-quality coating with consideration of a real industrial scenario can be obtained by the proposed model.

Table 4.9 Experimental results of coating properties.

Experiment no.	Process parameter					Coating property		
	F (SLPM)	O (SLPM)	N (SLPM)	A (SLPM)	S (mm)	Porosity	Deposition efficiency	Adhesion bonding strength (MPa)
Optimal	180.6	625.6	39.0	577.9	179.4	1.41%	57.45%	31.0
Contrast 1 (Low)	107.9	557.9	24.7	490.9	126.4	>10%	53.20%	8.8
Contrast 2 (High)	192.0	642.0	75.2	659.1	193.6	3.09%	53.85%	16.2
Contrast 3 (Random)	112.8	641.2	57.9	494.8	142.3	2.30%	58.65%	22.2

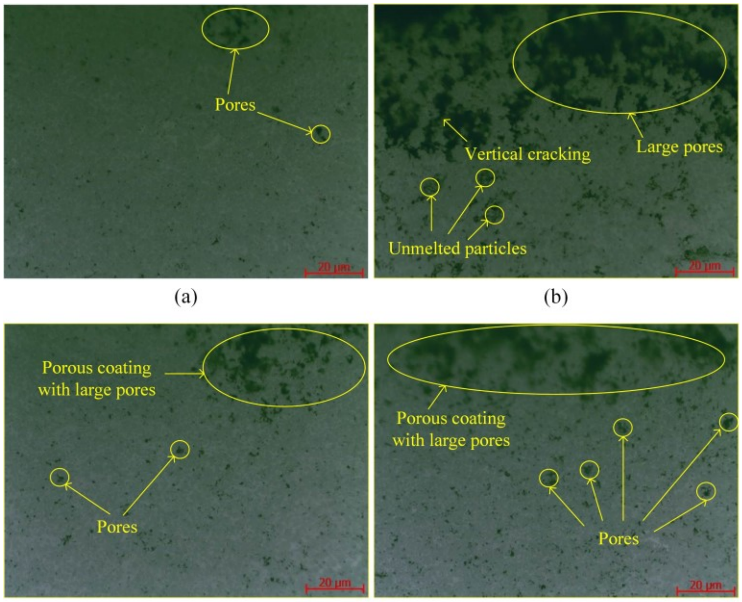

(a) (b)

(c) (d)

Figure 4.8 Microstructure of the coatings viewed on a ZEISS Imager.A2m. (a) the coating structure with the optimal parameters; (b) the coating structure of Contrast 1; (c) the coating structure of Contrast 2; (d) the coating structure of Contrast 3.

4.7 Conclusions

This chapter contributes to the implementation of the feature concepts introduced in Chapter 3 for developing multiple-view integration covering HVOF numerical analysis and process optimization, where the spray coating is optimized by controlling the in-flight particle behavior. The whole engineering process is modeled in terms of three views, CAD/CFD integration view, CFD analysis view, and optimization view. In order to map the real working conditions and HVOF system specifications into different models' setups, the entities involved in each view are constructed by using the feature concepts, hence seamless information transfers among the views are achieved. Built on top of the previous research efforts on the HVOF numerical modeling, an integrated solution for constructing HVOF interdisciplinary CAD/CFD/Optimization model has been proposed. A closed-loop complex engineering process optimization method has been developed. In this method, the optimization intent drives the numerical analysis scenarios via a parametrically controlled CAD/CFD integration solution. The optimization is conducted via the multi-response surface method with the desirability function approach used to derive the optimal process parameters.

The effectiveness of the interdisciplinary modeling method was demonstrated through a case study of an HVOF spray system depositing WC-12Co coating. It should be highlighted that the proposed system has been systematically modeled in a feature-based environment. For example, a parametric template of the numerical analysis was constructed for carrying out a group of simulations requested by the optimization intent. A set of sampled design points was taken to illustrate the numerical model generation progressively. Finally, the RSM method was used to construct the optimization objectives of the particle velocity and temperature and then these two objectives were converted into a single optimization objective via the desirability function. The derived parameter values from this optimization objective were experimentally verified via reviewing the coatings. That means the virtual model is able to provide meaningful feedback to its real twin. Besides relying on the proposed association mechanism, the modeling method can be applied to various industrial process scenarios without repetitive tasks. Therefore, it can be concluded that the proposed approach is generic for industrial HVOF processes and useful for the real-world process.

Chapter 5: Inter-module Data Processing

5.1 Chapter Overview

As introduced in Chapter 3, for comprehensively describing a physics phenomenon, multiple modules' outputs in the proposed framework should be integrated together. This chapter keeps on using HVOF processes as an example for explaining the associations among multiple modules with interdisciplinary dependencies. Coating thickness is selected as the target phenomenon.

Like most coating processes, in HVOF processes, the coating thickness is a critical property that should be precisely controlled during the process [91,121]. In view of green, smart, and digital manufacturing, the coating thickness prediction model is demanded to produce high-quality coatings efficiently. In the aspect of HVOF thermal spraying, the modeling is still highly challenging due to its complex system and multidisciplinary process parameters. Its coating thickness models, especially for studying the specific HVOF parameters, are still in relative infancy. Most research works were devoted to the kinematic parameters' effects, e.g., scanning speed, scanning step, and spray distance, on the coating thickness [91,122]. The operating parameters and working conditions specifically used in the HVOF coating, e.g., the gas flow rates and the nozzle geometry, are also critical factors of determining the coating quality [123]. However, they have not been considered in the previous research works. Moreover, most of the previous models were empirical models derived from the experimental data. Although these models are reliable for specific applications, they may not be applicable to other systems and working conditions, and these modeling methods based on experiments are time-consuming and expensive, which does not satisfy the requirement of the DT concept. Therefore, this chapter proposes a parametric and flexible model for HVOF coating thickness control with due regard to the complex spray system and the multidisciplinary parameters by using numerical modeling.

The related works have been reviewed in Section 2.3. The remainder of this chapter is organized as follows: Section 5.2 demonstrates the procedure of the proposed model by simulating a specific scenario. The associations among the above-described models are also clarified in this section. In section 5.3, the simulation results and experimental validations under four sets of operating parameters are presented to verify the effectiveness of the model.

5.2 Associations among the Multiple Modules for HVOF Coating Thickness Simulation

The general procedure for constructing the model is presented in Figure 5.1. The first step is to simulate the in-flight flame/particle behavior by using the in-flight behavior model developed in Chapter 4. Due to the revolved structure of the nozzle chamber, the model in Chapter 4 is always built on a 2D axisymmetric CFD model to reduce the computation cost. Once the steady behaviors of the combustion, flame, and in-flight particles are obtained, the particle landing distribution on the substrate surface can be extracted from the HVOF in-flight particle feature. To evaluate the influence of particle size on the deposition distribution, by suiting the Rosin-Rammler diameter distribution [124,125] the particle size range is discretized into a number of groups that are separately inputted to the in-flight behavior model and get their landing distributions on the substrate surface. Then, according to the particle landing distribution, a rule-based coating growth model captures an initial coating profile in the second step. The third step is to convert this initial coating profile built on the in-flight behavior model to a 3D single coating profile and fit the converted profile by a Gaussian distribution. The last step is to apply the Gaussian distribution and simulate the coating thickness with a spray path through a proposed linking method. The details of each step are presented in the following subsections.

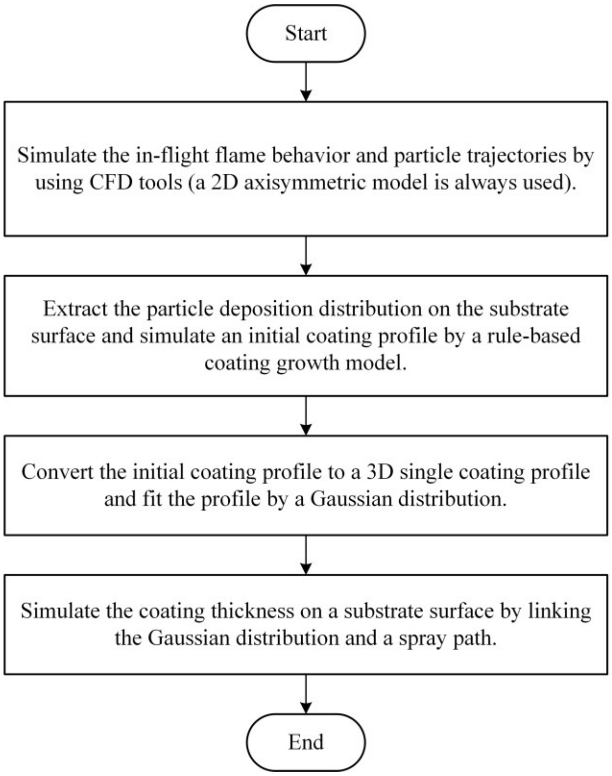

Figure 5.1 The procedure for simulating the coating thickness in HVOF processes.

5.2.1 In-flight behavior modeling and particle trajectory simulation

5.2.1.1 HVOF in-flight behavior under a specific operating scenario

As the coating formation process in the HVOF is determined by the in-flight particle behavior prior to the impact on the substrate surface, which, in turn, is affected by the combustion, flame, and in-flight particle behavior, these physicochemical phenomenon simulations are noticeable for the coating thickness modeling. Based on the study in Chapter 4, the in-flight behavior is controlled by the operating parameters, such as the gas flow rates, spray distance, and other operational conditions, like the nozzle configuration and particle properties. Thus, for predicting the coating thickness profile, the HVOF in-flight behavior should be obtained firstly. To demonstrate the steps for modeling coating thickness, a set of operating parameters indicated in Table 5.1 (recommended by the manufacturer) is used here. The same homemade Diamond Jet Hybrid gun as shown in Figure 4.6(a) and (b) is still used in this chapter. By setting up these initial operational conditions on the developed in-flight behavior model, for example, Figure 5.2 presents partial properties of the flame under the operating parameters given in Table 5.1, the velocity magnitude contour and pressure contour of the flame flow.

Table 5.1 A specified set of operating parameters for the coating thickness model demonstration.

Case	Propane flow rate (SLPM)	Oxygen flow rate (SLPM)	Nitrogen flow rate (SLPM)	Air flow rate (SLPM)	Powder feed rate (g/min)	Spray distance (mm)
Baseline	257	954	52	469	53.3	160

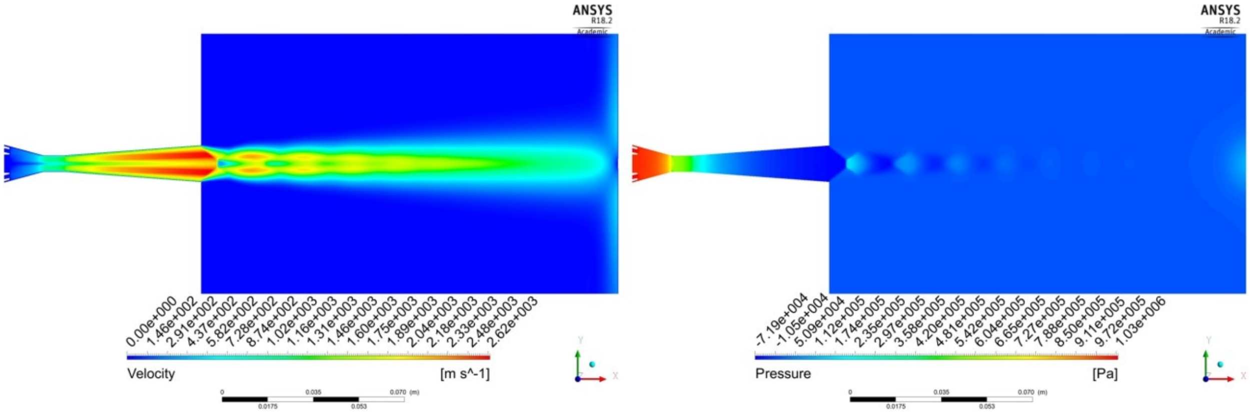

(a) (b)

Figure 5.2 Flame properties with the specified operational parameters: (a) velocity magnitude contour of the flame flow; (b) pressure contour of the flame flow.

As mentioned in the literature review, owing to the very low particle loading (less 4% usually) [81], a one-way coupling between the gas phase and the particle phase is assumed, in other words, the momentum and heat of the particle are solved by the Lagrangian approach after the gas flow fields are determined, and the particles have no influence on the gas phase [82,83]. It should be noted that this model for computing the in-flight particle behavior was widely used in previous studies, and partial particle properties have been tested against experimental results [72,77,81]. For example, the simulated particle velocity and temperature at impact in Li and Christofides's work [80,81] are consistent with experimental observations of Zhao et al. [126]. In a more recent publication, this algorithm, computing particle behavior after solving the gas phase, was further tested in a more advanced HVOF technology, suspension HVOF [77]. In this publication, the simulated particle velocity and temperature at different standoff distances were in good agreement with the experiment, and the variation trend was similar. Collectively, this model is adequate for simulating particle behavior.

Therefore, in this work, once the flame behavior simulation reaches a certain stable state, powder particles can be inserted into the model through the corresponding boundary condition as shown in Figure 4.6(c) and released from the grid nodes. The length of releasing particles along the feedstock inlet boundary shown in Figure 4.6(a) and (c) and the initial particle velocity are carefully set up according to considerations of the real scenario and may need to be reasonably tuned to provide results for important characteristics of the coating profile (such as the width of the single coating profile) that are consistent with the available experimental results. For the homemade HVOF system used in this work, this length is set up as 3.5 mm from the axis of the gun along the radial direction, and the particles are released from the feedstock inlet boundary with an initial velocity of 0.01 m/s. The powder particles should be evenly dispersed on the area of the feedstock inlet. Their thermophysical properties and shape equivalent factors can be correspondingly assigned to the parameters shown in Appendix 1. In this work, WC-12Co powder particles are still used to demonstrate the modeling process. Table 4.2 [118] shows their thermophysical properties. However, for getting an obvious bead-like shape for the coating profile measurement, the particle size distribution is different. The particle size distribution used in this chapter's work is given in Figure 5.4 in the next subsection. Figure 5.3 is a scanning electron microscope (SEM) image of the WC-12Co powder particles, which indicates the spherical particles should have a shape factor of 1. Apart from these parameters, particle size distribution is a critical factor affecting the coating profile [85]. The following subsection introduces the particle size discretization and gives a demonstration of the in-flight particle behavior simulation.

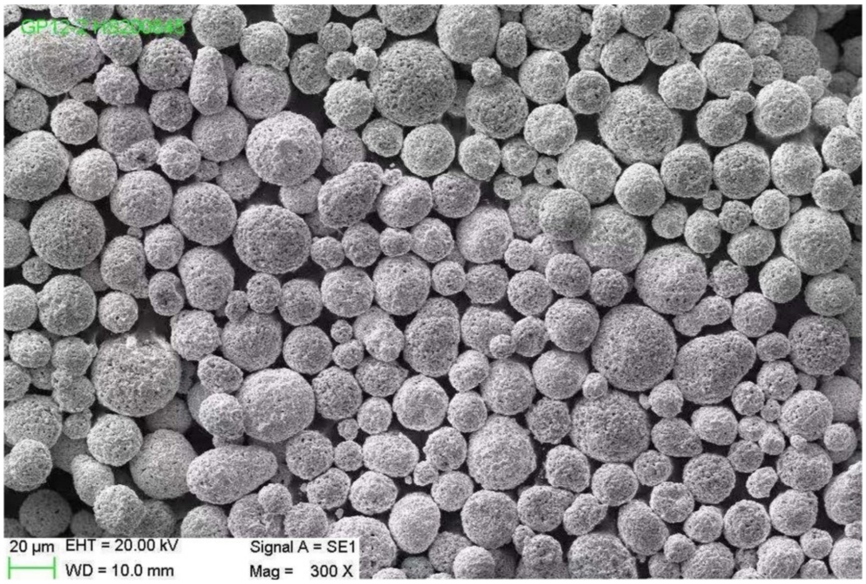

Figure 5.3 SEM image of the WC-12Co powder particles.

5.2.1.2 Particle size distribution and the in-flight particle behavior simulation

Because the size distribution of the powder particles used in HVOF thermal spraying is polydisperse, and particles of different sizes have different dynamic behavior during the flight due to different momentum, the particle size distribution [81] should be taken into account for accurately calculating the particle deposition distribution on the substrate. The Rosin-Rammler distribution of cumulative mass [127] widely exists in the literature and industry for describing the powder particle size [81,124]. To simulate this effect, this approach discretizes the particle size range into numerous groups of different sizes with the same number of particles firstly. Then these groups are separately inserted into the stable flame simulation for computing the in-flight trajectory of particles of different sizes. Meanwhile, the Rosin-Rammler distribution of cumulative mass is converted to the count distribution of particles [127], which will be introduced in the next subsection to simulate an initial coating thickness by combining a rule-based coating growth model.

For further demonstrating this step, taking the WC-12Co powder particles as an example, however, it should be noted that the particle size is from 7.5 μm to 50 μm, which is different from the size in Section 4.6.1 and follows a Rosin-Rammler distribution of cumulative mass as shown in Figure 5.4. The model computes the trajectories of 30 groups of different particle diameters. The discretized particle sizes are represented by the orange circles in Figure 5.4. The star signs are the measurement result from a laser diffraction analyzer, which validates this Rosin-Rammler distribution. Figure 5.5 shows the trajectories of the partial particles under the above flame behavior. Please note that, for including the effect of turbulent velocity fluctuations on the particle trajectories, the particle motion in the turbulent flow is calculated in a stochastic tracking approach [124] and up to 15 independent stochastic particle tracking calculations are performed to obtain the statistical description of the particle trajectories in the gas flame. Therefore, in the simulation, 480 particles per group are released on the boundary condition and computed in the gas flame (this number is also relevant to the node number at the particle-insert boundary condition). Appendix 4 is the MATLAB code for automatically carrying out the simulation of the particle trajectories.

Apart from the particle trajectories, other in-flight particle parameters with the consideration of the particle size distribution, e.g., temperature, melting ratio, and flight time, can be computed according to the equations shown in Appendix 1.

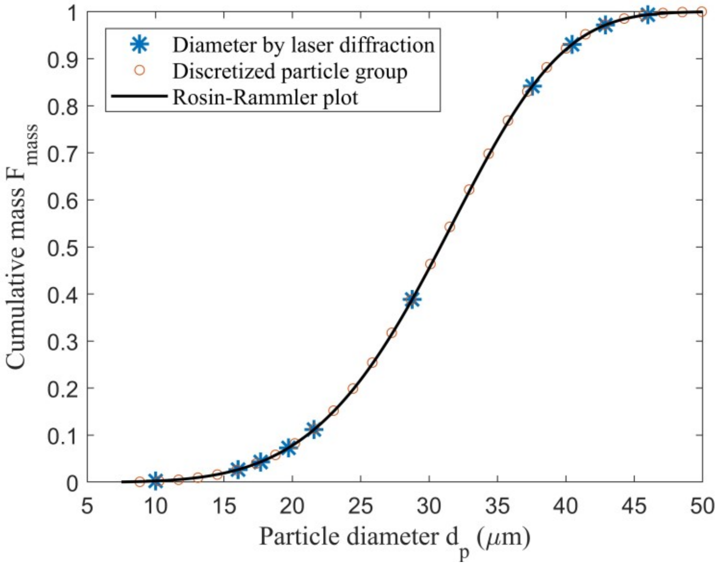

Figure 5.4 Cumulative mass distribution of the WC-12Co powder particles and particle size discretization for the demonstration of the coating thickness modeling.

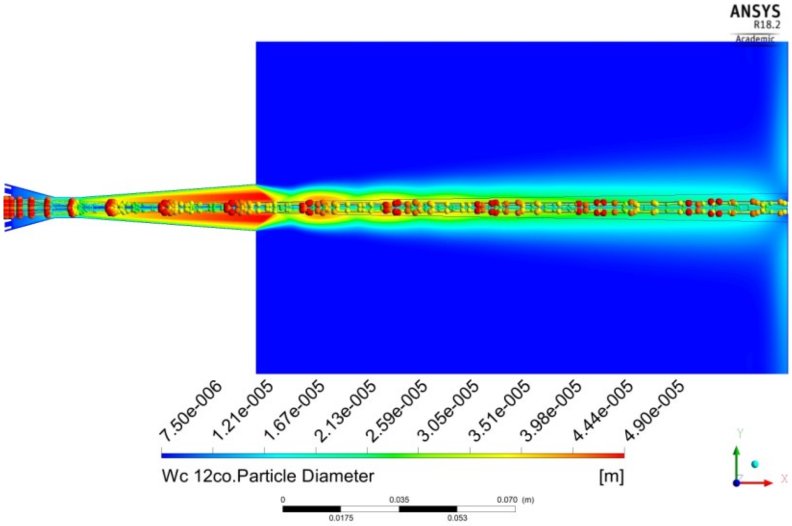

Figure 5.5 Trajectories of the partial particles under the specific operating parameters and conditions.

5.2.2 The coating profile based on the in-flight behavior model

5.2.2.1 Splat morphology approximation and coating growth

Once the particle trajectory calculations are completed, the particle physics behavior and distribution at impact (on the substrate surface as shown in Figure 4.6(a)) can be extracted from the HVOF in-flight particle feature. Then, based on the extracted data, an initial coating thickness on the area in the red rectangle shown in Figure 5.6 can be computed by modeling the coating growth.

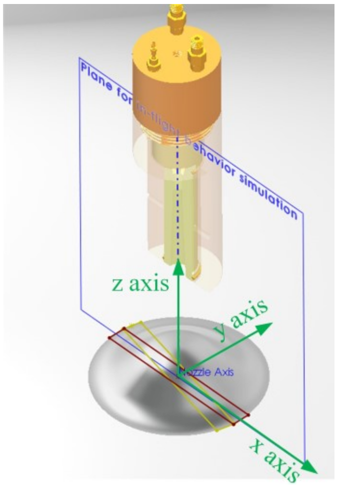

Figure 5.6 Schematic depiction of the single coating profile calculation.

However, coating growth is a complicated process. Generally, thermally sprayed coatings mainly consist of lamellar splats interspersed with a small number of pores and unmelted particles as shown in Figure 5.7(b). The splats are the major building blocks of the coating, which are formed by the impact, deformation, spreading, and solidification of the individual powder particles [94,128]. Each particle is accelerated and heated in the flame during the process, after which it impinges on the substrate or previously deposited coating layer in a molten, partially molten, or solid state. At impact, the sudden stagnation of the particles leads to a pressure buildup and deformation occurs. Then the molten part of particles spreads outward from the point of impact and forms a splat [94,129]. Figure 5.7(a) gives a scanning electron microscope (SEM) image of a single splat on a flat substrate surface. These pores as shown in Figure 5.7(b) are deformed by the interaction of the new deposited particles and the previously deposited coating layers. The coating growth process can be treated as the pile-ups of these compositions as depicted in Figure 5.7(c).

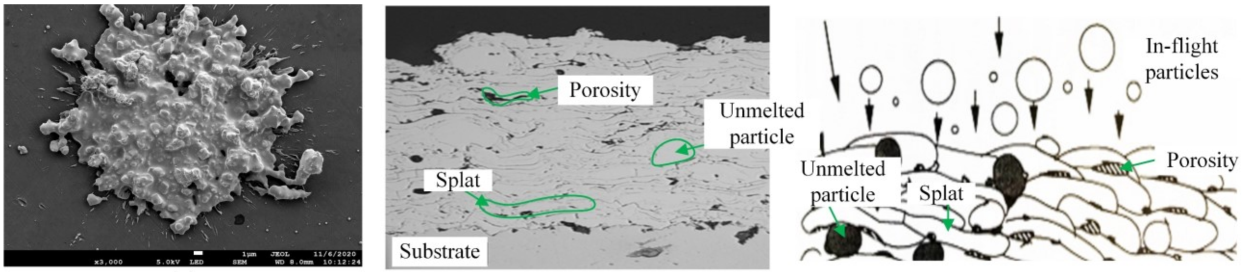

(a) (b) (c)

Figure 5.7 The major characteristics of coating formation: (a) SEM image of a single splat under a set of specific operating parameters; (b) microstructure of a thermal spray coating; (c) schematic of the coating formation.

It is obvious that the complete virtual model with the consideration of all physics phenomena involved is hard to be realized. Moreover, modeling the impact and solidification of just a single drop even requires many hours of computing time. Simulating the pile-ups of a huge number of particles is impractical. Since this work concentrates on the macro coating thickness profile (the radius of a single coating profile is typically several millimeters), the micro-level splat morphology (the radius of a single splat typically ranges from several micrometers to several hundred micrometers) is simplified with reasonable assumptions, which are discussed in the following paragraphs. Here the splat morphology [130] is the final shape of a single particle on the substrate or previously deposited coating layer after the impact, spreading, and solidification. In addition, according to the above major characteristics of the coating formation, some rules for calculating the pile-ups of particles are adapted in this work on the basis of previous related research works [72,80,94].

Regarding the particle deformation at impact, there are two assumptions in HVOF processes. As shown in Figure 5.8(a), if a particle can reach a fully melted state just prior to impact, the droplet becomes a lamellar splat as a result of deformation which can be treated approximately as a cylinder shape [131,132]. The splat flattening degree ξ is defined by the following equation:

$$\xi = \frac{D}{d_p} \tag{5.1}$$

where D is the approximated diameter of the splat and d_p is the particle diameter prior to impact. The previous research indicated that for HVOF coatings ξ predominantly depends on the Reynolds number which represents the viscous dissipation of the inertia forces [94,131]. The flattening ratio can be approximated by a function of this parameter as follows [94,131]:

$$\xi = 1.2941Re^{0.2} \tag{5.2}$$

where, Re is the Reynolds number of the droplets. ($Re = d_p\upsilon_p/\nu_p$, where ν_p is the kinematic viscosity of the droplets, υ_p is the droplet velocity prior to the impact on the substrate surface.)

If a particle is partially melted, the unmelted particle will form a hemisphere with the equivalent volume and the melted part will form a ring around the hemisphere as depicted in Figure 5.8(b) [94,133]. The flattening ratio of the melted part can be calculated by using the above equation.

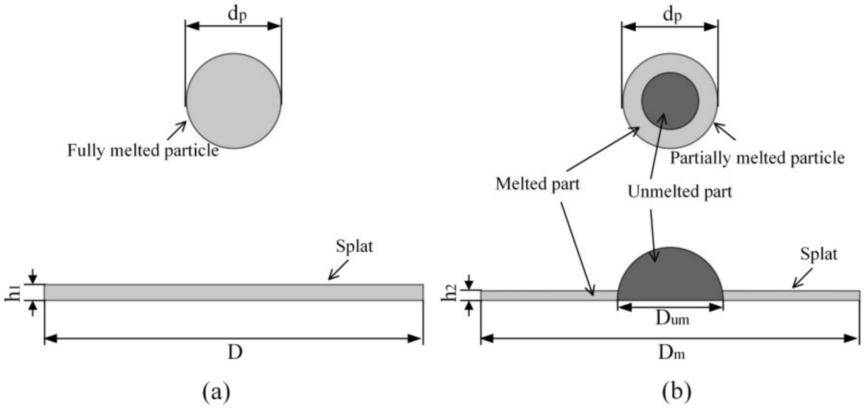

Figure 5.8 Deformation of a fully melted particle (a) and partially melted particle (b) upon impact on the substrate (adapted from [94]).

To simulate the pile-ups of splats, some rules are adapted in this work on the basis of the related research works [72,80,94] to program different events that might take place when a particle hits the substrate and previously deposited coating layer. A brief summary of these rules is given here. For a more detailed interpretation, the reader could refer to [94].

1. As shown in Figure 5.9(a), if a particle at impact is partially melted, the unmelted part will form a hemisphere on the previously deposited layer, and the melted part will form a ring around this hemisphere. Besides, if the unmelted part of the particle locates at the previously deposited layer where cavities exist, pores will form under the hemisphere.

2. If the unmelted part of the particle hits at the previously deposited layer that is formed by an unmelted particle, it will bounce off and only the melted part will be deposited (Figure 5.9(b)).

3. If the particle is able to cover a whole step and the splat encounters a dead end, it will break at the corner of the step as shown in Figure 5.9(c).

4. If the particle impinges at the corner or boundary of a step, and the ratio of the height of the step to the thickness of the splat is not great, the splat will flow over the corner and outer surface as shown in Figure 5.9(d).

5. If the splat comes to the previously deposited layer with small gaps as shown in Figure 5.9(e), the splat will cover the gaps, and pores will form.

6. In the fourth rule, if the ratio is large enough, the splat will flow over the corner and form a slope at the corner as shown in Figure 5.9(f).

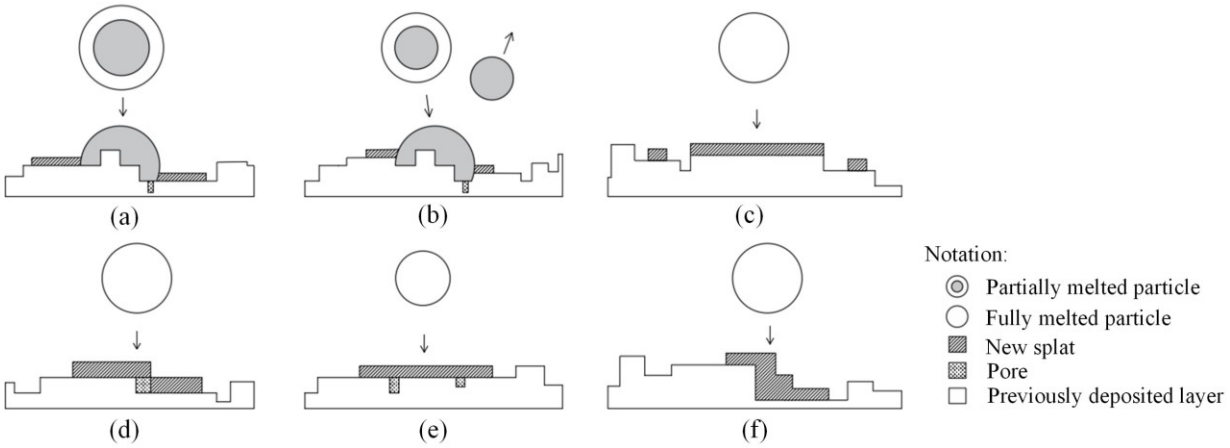

Figure 5.9 Splat formation rules (adapted from [94]).

5.2.2.2 Combination of the in-flight particle behavior and the splat morphology approximation

By combining the above rules and the particle parameters at impact from the in-flight behavior model (e.g., Reynolds number, melting ratio, particle distribution), the coating growth can be calculated. Finally, an initial coating height based on the 2D numerical model with the consideration of the particle size distribution is the summation of these groups by multiplying their corresponding count distribution, as shown in Figure 5.10, derived from the abovementioned cumulative mass distribution. The result of this step is corresponding to the initial coating height on the area highlighted by the red rectangle in Figure 5.6.

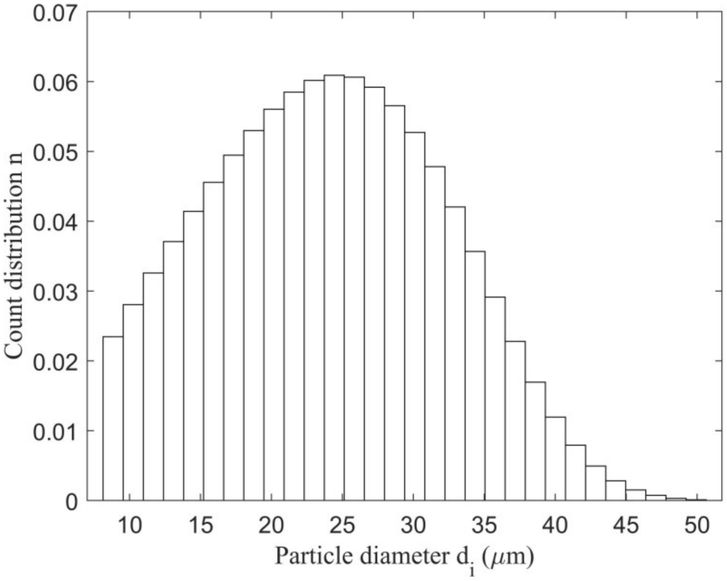

Figure 5.10 Count distribution of the WC-12Co powder particles.

5.2.3 Single coating profile construction

5.2.3.1 Initial single coating profile calculation

After getting the initial coating height on the area of the red rectangle in Figure 5.6, the next step is to create a circular pattern of the initial coating height model using the axis of the nozzle and calculate the overlapping parts, like the overlapping area of the red and yellow rectangles as shown in Figure 5.6. It is worth noting that, for getting a continuous coating distribution, the instances in the circular pattern could be evaluated by Equation (5.3)-(5.6).

$$number\ of\ instances = \frac{2\pi}{Width\ of\ sample/Length\ of\ sample} \tag{5.3}$$

where *Length of sample* can be estimated by the maximum radial distance of the particle distribution at impact, *Width of sample* can be calculated by using the average diameter of particles as the following equations:

$$CMD = \frac{\sum n_i d_i}{N} \tag{5.4}$$

where CMD is the count mean diameter; d_i is the median value of the particle diameter in the groups in Figure 5.10; n_i is the count distribution; N is the total count of the particles.

$$Width\ of\ sample = 2 \times \left(\frac{4/3\pi (CMD/2)^3}{\pi h_{splat}(CMD)} \right)^{1/2} \tag{5.5}$$

where h_{splat} is the function of the equivalent height of the splat which can be derived from Equations (5.1) and (5.2).

Figure 5.11(a) presents the initial coating model after the circular pattern construction. Through numerical and experimental validations, for most thermal spray processes, the Gaussian distribution can be used to accurately represent the single coating profile [91,122,134]. Hence, a symmetric Gaussian distribution is applied to characterize the cross-sectional profile of the coating model, as illustrated in Figure 5.11(b). Equation (5.6) is its mathematical expression.

$$\varphi = \delta(\dot{m}, \gamma) a e^{-\left(\frac{r-b}{c}\right)^2} \tag{5.6}$$

where φ, called the single coating profile, is the coating height of the position r meters away from the position of the center of peak (b) where the nozzle stationarily stays at a position for one second. Thus, the unit of φ is m/(m^2·s). a is the height of the curve's peak and c is the standard deviation. For the scenario described above, a equals 4.271×10^{-5}, b is 4.292×10^{-7}, and c is 3.743×10^{-3}.

$\delta(\dot{m}, d_{\bar{m}}, \gamma)$ is a function relevant to the powder feed rate ($\dot{m}$) and the deposition efficiency (γ) [135]. Their estimations will be introduced in the following subsection.

In the Cartesian coordinate system, the distance away from the position of the center of the peak, *r*, can be calculated by the following equation:

$$r = \sqrt{(x - u_x)^2 + \left(y - u_y\right)^2} \tag{5.7}$$

where (u_x, u_y) is the center coordinate of the coating profile on a substrate surface.

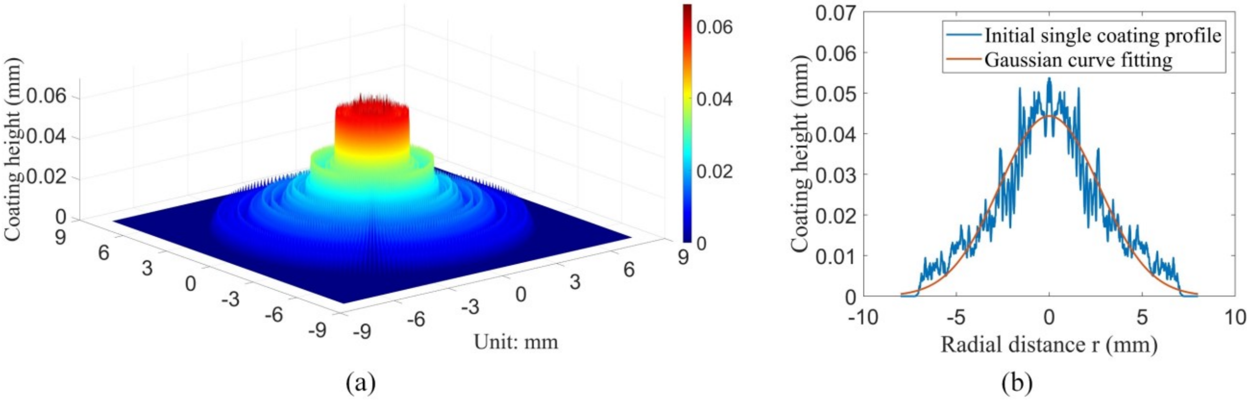

Figure 5.11 Gaussian fitting of the coating profile: (a) Initial single coating profile; (b) Gaussian curve fitting of the cross-sectional profile.

5.2.3.2 Deposition efficiency determination

So far, the mass rate of the powder particles and the deposition efficiency have not been considered in the modeling. In HVOF processes, in addition to the unmelted particles bouncing off the substrate, the deposition efficiency is affected by many other parameters and factors, like the spray distance, gas flow rates, robot kinematic parameters. Among these parameters, the fuel flow rate is a critical one. A low fuel flow cannot heat the particle to reach a molten state, which results in deposition efficiency reduction. On the other side, a high fuel flow may overheat particles and cause particle oxidation, which also leads to a low deposition efficiency. For simplification, in this work, only this critical parameter, fuel flow rate, was studied to quantify the variation of the deposition efficiency. A series of fuel flow rates changing from 80 to 380 SLPM were implemented for measuring their deposition efficiencies. The experimental measurement results and the regression model are given in Figure 5.12.

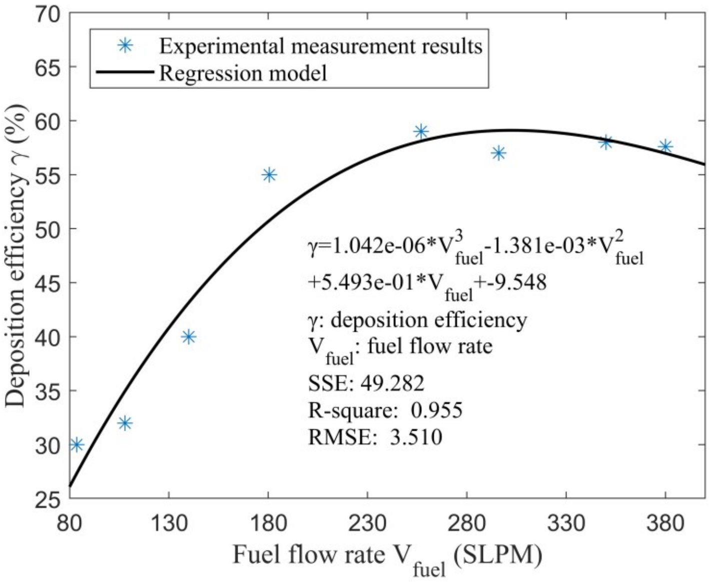

Figure 5.12 Empirical model of the fuel flow rate and the deposition efficiency.

5.2.3.3 Single coating profile model

After determining the deposition efficiency under a specific gas flow rate, the number of the deposited particles can be estimated by using Equations (5.8) and (5.9). The unmelted particles bouncing off the substrate, which is introduced in Section 5.2.2.1, should not be considered as the deposited particles.

$$\dot{N}_{deposited} = \gamma \dot{N}_{total} \tag{5.8}$$

where $\dot{N}_{deposited}$ is the number of deposited particles per second, and $\dot{N}_{total}$ is the total number of particles fed into the nozzle per second, which can be approximated by the following equation:

$$\dot{N}_{total} = \frac{\dot{m}}{\frac{4}{3}\pi\rho_p\left(\frac{1}{2}d_{\bar{m}}\right)^3} \tag{5.9}$$

where ρ_p is the density of powder particles, $\dot{m}$ is the powder feed rate, and $d_{\bar{m}}$ is the diameter of mass average [127], which can be derived by using the count distribution.

$\delta(\dot{m},\gamma)$ used in Equation (5.6) is a function to include the effect of the powder feed rate and the deposition efficiency on the single coating profile. Its analytical derivation is given by Equations (5.10) and (5.11).

$$\delta = \frac{\dot{N}_{deposited}}{\sum n_i N_{group}} \tag{5.10}$$

where n_i is the count percentage of different size particles, for example, for the WC-12Co used in this work, the count percentage of different size particles is given in Figure 5.10. N_{group} is the number of particles in the groups of discretized particle sizes.

Then, substitute Equations (5.8) and (5.9) into Equation (5.10). $\delta(\dot{m},\gamma)$ is given as:

$$\delta(\dot{m},\gamma) = \frac{\gamma\frac{\dot{m}}{\frac{4}{3}\pi\rho_p\left(\frac{1}{2}d_{\bar{m}}\right)^3}}{\sum n_i N_{group}} \tag{5.11}$$

Finally, by substituting Equation (5.11) into Equation (5.6), a single coating profile model can be obtained. Figure 5.13 shows the 3D model of the single coating profile under the scenario described above. Equation (5.12) is its mathematical expression. The algorithm is performed in the software Matlab 2020b on a 64-core CPU with a utilization of 70-80%.

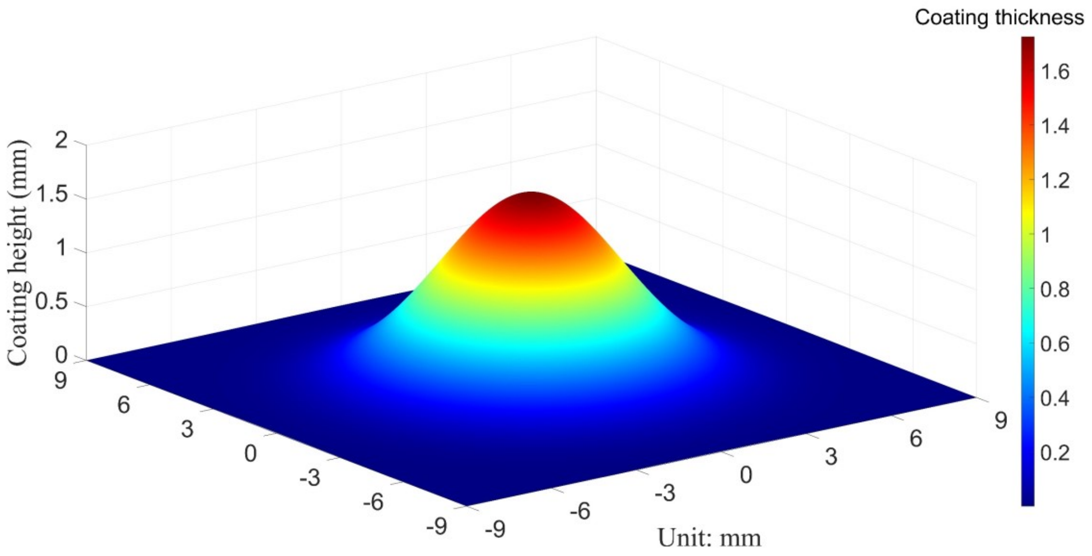

Figure 5.13 3D model of the single coating profile under the specific scenario.

$$\varphi = 1.790 \times 10^{-3} e^{-\left(\frac{\left(x^2+y^2\right)^{1/2} - 9.205\times10^{-7}}{3.809\times10^{-3}}\right)^2} \tag{5.12}$$

5.2.4 Integration of the spray path for the coating thickness simulation

By combining the numerical model of the single coating profile with the parameters relevant to the nozzle movement, e.g., scanning speed and scanning step, it is able to build the model of coating thickness distribution on a substrate surface deposited by a nozzle path. Firstly, the substrate surface needs to be meshed by refined grids. Secondly, the spray path should be dispersed into a series of target points (nozzle trajectory). Then, the target points on the nozzle path are transformed into mapped target points on the substrate surface along with the orientation of the spray nozzle. After the target point transformation, for a moment that the nozzle passes through a target point, the coating height at each grid node can be calculated by substituting the node coordinate (x, y) into the integral in Equation (5.13). Lastly, by repeating this step with the progress of the nozzle movement, coating thickness distribution on the entire substrate surface can be simulated. In this way, it can simulate the effect of the nozzle movement parameters on the coating thickness distribution, such as scanning step and scanning velocity. The schematic depiction of the spray path integration will be further discussed in the next chapter. For a more detailed explanation of this part, the reader could refer to Section 6.3 and 6.3.2.

$$\emptyset_i = \emptyset_{i-1} + \int \left(\int \delta(\dot{m},\gamma) a e^{-\left(\frac{\left((x-u_{xi})^2+(y-u_{yi})^2\right)^{1/2}-b}{c}\right)^2} dxdy \right) dt \tag{5.13}$$

where $\emptyset_i$ is the coating height at the node coordinate (x, y) when the nozzle passes through the ith mapped target point (u_{xi}, u_{yi}).

5.3 Experimental Verification for the Coating Thickness Model

5.3.1 Experimental setup

For verifying the integrated modeling method, its simulation and corresponding experimental investigations under different operating parameters were implemented. The experiments were carried out by a homemade Diamond Jet HVOF spray system and a YASKAWA DX200 MA2010 robot system. For keeping the information consistency between the experiments and simulations, this section keeps using the feature-based in-flight behavior model in Section 4.6.1 for obtaining the flame behavior under different operating parameters. The building elements and geometries of the nozzle are the same as the ones used in Section 4.6.1, as depicted in Figure 4.6(a) and (b). The WC-12Co powder particles used in Section 5.2 for the modeling demonstration were kept on using in the experiments as feedstock to coat a flat-plane steel substrate (size: 200 mm × 200 mm × 20 mm). To reduce the effect due to the robot kinematics as much as possible, the spray path used for coating is designed as simple as possible, which is a straight line shown in red in Figure 5.14.

Besides, to avoid the deformation of the coating profile due to gravity during the coating formation, the substrate was placed horizontally. The impact of gravity on the in-flight particles can be neglected due to the high velocities and high-velocity gradients [81,136]. In order to obtain an obvious bead-like shape for observation and measurement, the nozzle reciprocated up and down along the red path with a scanning velocity of 300 mm/s for12 passes. Furthermore, the lateral distance is 100 mm, which is far away from the substrate edge, so that the robot can reach a stable motion before passing through the substrate. The spray distance was kept constant during each experiment. Table 5.2 shows the detailed spray distance and operating parameters for different experiments. Apart from the parameters (baseline) for the model demonstration in Section 5.2, three additional sets were conducted to further evaluate the predictive capability of the proposed model. Two of them were conducted respectively above and below the gas flow rates of fuel and oxygen in Case 1, and one is a set of parameters with a shorter spray distance.

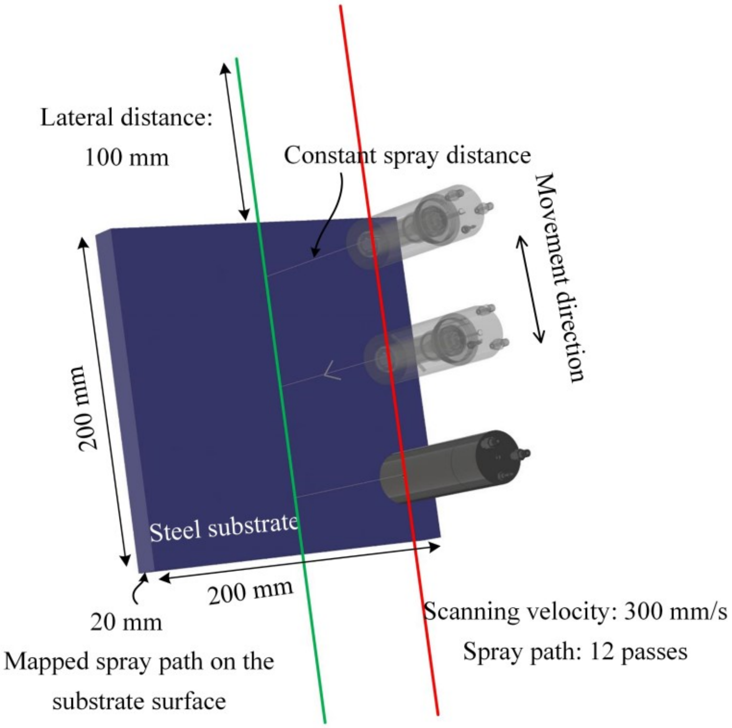

Figure 5.14 Experiment setup for the verification of coating thickness.

Table 5.2 Operating parameters in the experiments and simulations.

Case	Propane flow rate (SLPM)	Oxygen flow rate (SLPM)	Nitrogen flow rate (SLPM)	Air flow rate (SLPM)	Powder feed rate (g/min)	Spray distance (mm)
1 (Baseline)	257	954	52	469	53.3	160
2	353	1105	52	469	53.3	160
3	257	954	52	469	53.3	100
4	150	580	52	469	53.3	160

5.3.2 Results and discussion

The results of experiments and simulations under the scenarios in Table 5.2 are introduced in this subsection. The left side from top to bottom in Figure 5.15 respectively shows the top views of the coatings after 12 passes in the experiments of Case 1, Case 2, Case 3, and Case 4. The right side in Figure 5.15 is their corresponding simulation results. It is known that the simulated coating thickness along the path direction is almost continuous and same due to the very short time step (0.1 ms). Thus, only partial lengths of the coatings are displayed in Figure 5.15 as the representatives of the simulation results. To conveniently compare the width of the coating profile, the origin of coordinates lies at the entry point of the nozzle on the substrate surface. The positive and negative values of the width all mean the radial direction of the coating profile. From Figure 5.15(a) and (b), it can be observed that the width of the coating bead in the experiment is around 17 mm, which is very closed to that of the simulation. Similarly, in Figure 5.15(c)-(h), we can observe the widths of Case 2, Case 3, and Case 4 are about 15 mm, 12 mm, and 16 mm, which are also in good agreement with the simulated widths. From these observations, it can be confirmed that the developed model is able to simulate the coating distribution.

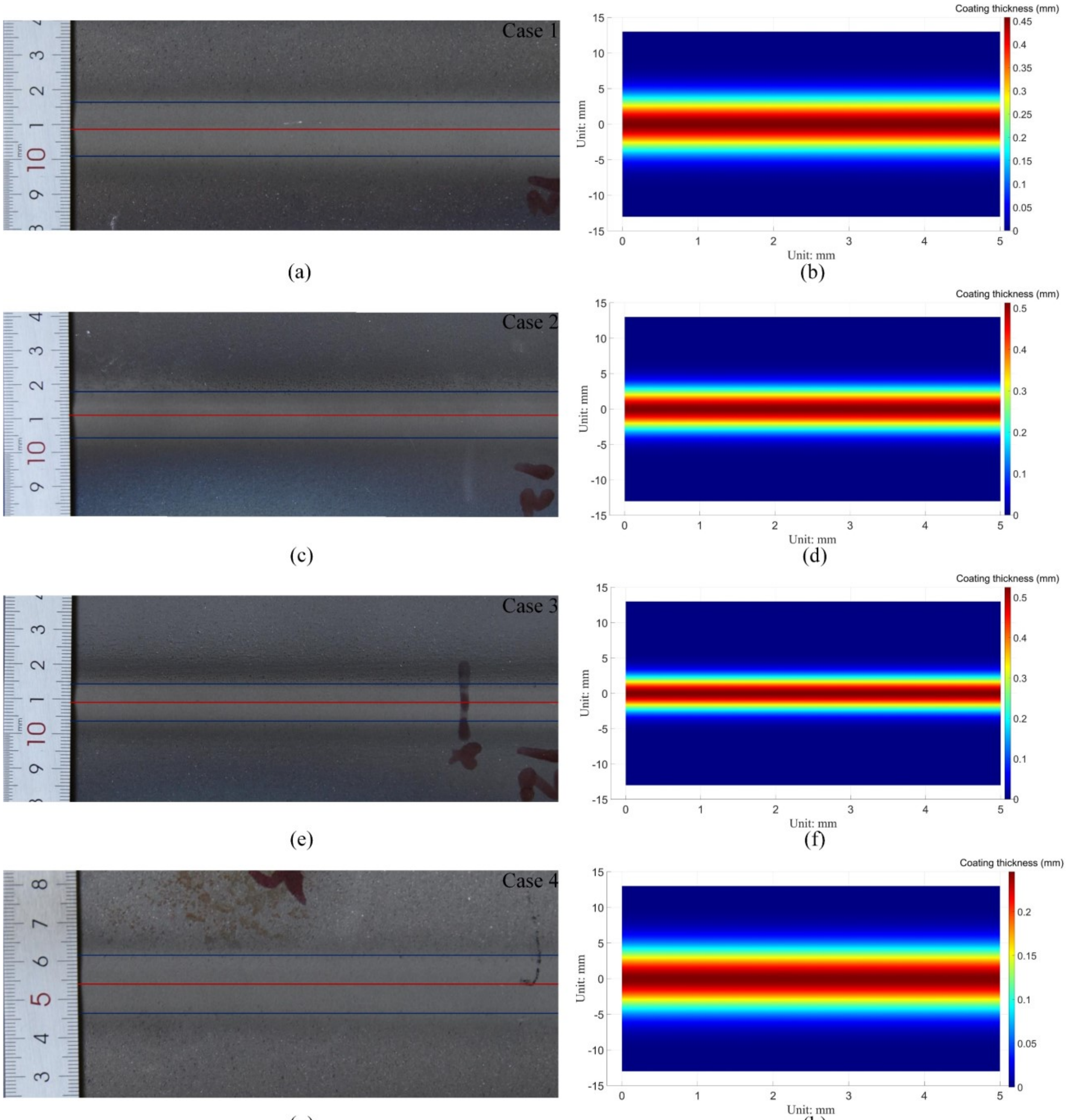

(a) (b)

(c) (d)

(e) (f)

(g) (h)

Figure 5.15 Coating distribution comparison of experiment and simulation: (a) Experiment result of Case 1; (b) Simulation result of Case 1; (c) Experiment result of Case 2; (d) Simulation result of Case 2; (e) Experiment result of Case 3; (f) Simulation result of Case 3; (g) Experiment result of Case 4; (h) Simulation result of Case 4.

For accurately evaluating the capability of the developed model, in the experiments, the cross-section at the middle of the length of the coating beads was measured by contour measuring equipment (HOMMEL ETAMIC nanoscan 855). These measurement results were compared with the corresponding simulation results, as shown in Figure 5.16. The measurement results under the 4 sets of parameters (Case 1, Case 2, Case 3, and Case 4) are displayed in orange in Figure 5.16(a)-(d) respectively. The blue plots in Figure 5.16(a)-(d) are their simulated cross-sections. Obviously, the simulated coating profiles fit well with the measured ones. It also can be found that the coating thickness of Case 2 (Figure 5.16(b)) is higher than that of Case 1 (Figure 5.16(a)), but the width is narrower than that of Case 1 (Figure 5.16(a)). This was because the higher gas flow rates in Case 2 generated a flame jet with a higher axial velocity, which, in turn, accelerated the powder particles along the axial direction. Hence, the radial displacement of powder particles was relatively reduced, and the particles tended to impact around the center of the coating profile. A similar phenomenon was found in Case 3 (Figure 5.16(c)). The short spray distance in Case 3 also reduced the radial displacement of the powder particles. Case 4 (Figure 5.16(d)) has a flat coating profile with the lowest peak value due to a low deposition efficiency. When the gas flow rates came to a low level, most powder particles did not reach a molten state, so they could not stick on the substrate. Besides, the low gas flow rates generated a low-power flame which could not restrain the particle from depositing around the center of the coating, so the profile tended to be flat. For quantitatively assessing the capacity of the model, the mean absolute error (MAE) and root-mean-square error (RMSE) of the cross-section profile heights were calculated via more than 10,000 measurement points, where MAE represents the average of the absolute difference between the actual and predicted values in the dataset, and RMSE represents the square root of the average of the squared difference between the original and predicted values. Further, for providing an intuitive understanding of the accuracy, the normalized root-mean-square error (NRMSE) of the cross-section profile heights was calculated to interpret the error as a fraction of the overall range. Table 5.3 shows the calculation results. The MAE, RMSE, and NRMSE are around 0.04, 0.05, and 10% for the first three cases, which is acceptable. Case 4 has a relatively large error. In general, these results and analysis indicate that the proposed model enables the prediction of the coating thickness in HVOF processes with respect to the kinematic parameters for describing the spray path and HVOF specific operating parameters.

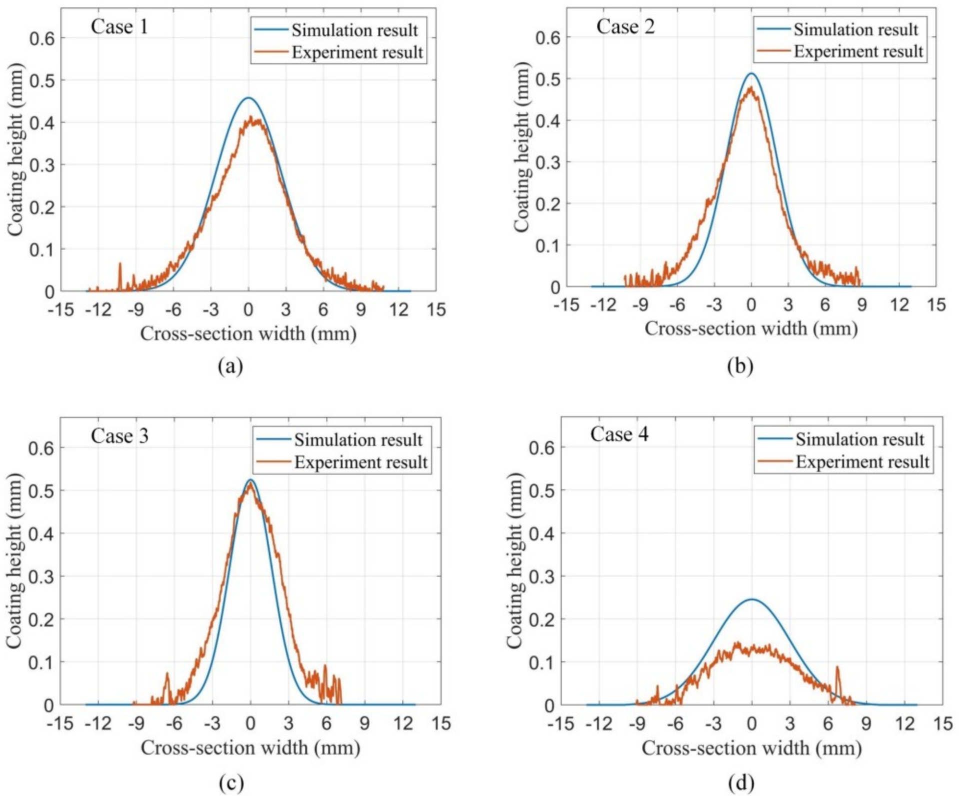

Figure 5.16 Cross-sectional profile comparison: (a) Cross-sectional profiles of Case 1; (b) Cross-sectional profiles of Case 2; (c) Cross-sectional profiles of Case 3; (d) Cross-sectional profiles of Case 4.

Table 5.3 Quantitative estimation of the accuracy of the developed model.

Case	Number of measurement points	MAE	RMSE	NRMSE
1	20778	0.0244	0.0343	8.28%
2	18107	0.0351	0.0417	8.67%
3	12068	0.0507	0.0606	11.68%
4	12068	0.0472	0.0608	41.55%

However, due to the complexity of the technology, there exist differences between the experimental and numerical results. Multiple reasons induce the differences. From the experimental point of view, the continuously high-energy jet during the coating may lead to the substrate to deformation, which affects the measurement accuracy. It can be found that, due to the thermal deformation, the experimental profiles, especially in Figure 5.16(a) and (b), are not symmetric and tend to be rightward. From the simulation point of view, the particle trajectories were solved by the stochastic tracking approach under the Reynold and Favre averaging flame. The particles may tend to land around the center of the profile. Thus, it can be observed that the simulated coating profiles are narrower and higher than the experimental results. In addition, the particle deformation at impact and the coating growth is approximately modeled with the consideration of very limited factors. However, the process is very complicated and affected by a number of factors. In the future, more factors can be consolidated in the empirical function to enhance the accuracy of the model.

5.4 Conclusions

This chapter contributes to an integration mechanism of multiple modules for simulating the coating thickness in HVOF processes. The kinematic parameters for describing spray paths are incorporated into the coating thickness model, thus the effect of spray paths on the coating thickness can be studied. Besides, the Gaussian coating profile is obtained via the feature-based in-flight behavior model. The HVOF specific parameters, such as fuel type and gas flow rates, and working conditions, like nozzle chamber geometry and powder particle property, are used to construct the Gaussian coating profile. Hence, the developed model can also analyze the influence of the HVOF specific parameters and conditions on the coating distribution. Through experimental investigations, the capacity of the model has been verified in this work.

Although some models built on experiments [92,93] also provide good accuracy, these models are usually reliable for a specific industrial scenario. When the working conditions change, the adjustment of these models will be expensive and time-consuming. The results in this chapter indicate that my model can flexibly simulate the coating thickness while considering different HVOF scenarios, like different operating parameters, different system configurations, and so on. This flexibility provides a possibility for developing a fully digital-twin model of this phenomenon, which will be further explained in the next chapter.

Chapter 6: Synchronization of Physics Phenomena

6.1 Chapter Overview

To face the challenges from digital twins, except the multiple-view integration, closed-loop optimization, and inter-module associations introduced in the above chapters, another important function in the proposed framework for constructing digital-physics phenomenon counterpart is the synchronization of phenomena and time-sensitive mutual supports among different models. The theoretical introduction about this function has been given in Sections 3.3.2 and 3.4. In this chapter, to validate the proposed function mechanism and the user-defined boundary condition feature, a feature-based model of synchronized coating performance is developed.

As introduced in Section 3.3.1, a robotized HVOF process usually consists of three major units, a Diamond Jet spray gun system which essentially contains the physicochemical phenomenon of the in-flight behavior of the flame and particles [72,80,81], a robot arm for handling the spray gun which usually concerns the dynamics and control [88,137,138], and a substrate to be coated which mainly involves the dynamic effect of the substrate and coating layers [87,88,139], for example, the temperature distribution of the substrate, and the coating growth. Regarding the Diamond Jet spray gun system, a feature-based model has been expanded upon in Chapter 4. The results from this model are used here directly. For a more detailed interpretation, the reader could refer to Chapter 4. The robot arm system does not have too many physics phenomena, so it is not the concern of this work. In this chapter, major attention is paid to the construction of a feature-based digital model for the coating layer and substrate.

In the following sections, the substrate temperature and coating thickness are selected as the main simulation intents while considering the synchronized physics phenomena which are obtained from the models developed in the above chapters. Here, the data processing among these models is the offline mode depicted in Figure 3.3. The remainder of this chapter is organized as follows: Section 6.2 presents a hierarchical key characteristic flow of HVOF processes. Section 6.3 demonstrates the offline mode of the data processing for the substrate temperature and coating thickness simulation. Section 6.3.1 describes the implementation of the feature-based modeling for the substrate temperature and coating thickness simulation. In Section 6.3.2, the user-defined boundary condition feature is further schematically depicted. Section 6.3.3 gives the simulation results with the synchronization of nozzle trajectory, coating thickness growth, and substrate temperature distribution. Section 6.4 is a branch of this study that compares two different turbulence models for the dynamic temperature performance of the HVOF process with experimental verification.

6.2 Hierarchical Key Characteristic Flow of HVOF Processes

As shown in Figure 6.1, the key parameters are marked in blue and the red color represents the key physics properties and a partial hierarchical information flow, which assist to build the inter-model associations for the phenomenon of the substrate temperature and coating thickness. For example, the substrate temperature field is determined by the heat flux on the substrate surface. The heat flux is contributed by two components, the flame, and the coating layer. As outlined in Figure 6.1, the heat flux from the flame can be extracted from the substrate wall in the feature-based in-flight behavior model developed in Chapter 4. Besides, as described in Chapter 5, a single coating profile can be developed via the particle landing distribution on the substrate wall in this model and a rule-based coating growth model. In terms of the coating profile, a transient thermal analysis model for estimating the change of the heat flux from the coating material is established with the initialization of the coating temperature by using the particle temperature prior to the substrate surface, where the particle temperature is also extracted from the in-flight behavior model. In the substrate temperature model, the changing heat flux from the coating materials, the constant heat flux from the flame, and the spray gun trajectory are read by a user-defined boundary condition which enables to update the boundary condition every time step. Meanwhile, the coating thickness distribution with the progress is computed based on the coating profile obtained from the in-flight behavior model.

The green marks explain the links between the real-world system and the virtual models. For instance, the operating parameters, e.g., gas flow rates and powder feed rate, can be monitored by the controller system. Their real-time values link the corresponding setup parameters of the CAE model via the proposed CAD functional feature and CAE boundary feature. The intelligent solver enables to deal with their changes. Based on the developed closed-loop and optimization-driven mechanism (Section 4.6.1)[129], a set of optimal operating parameters for improving the coating quality can be obtained and transmitted to the real system. Apart from this, the real-time trajectory from the robot is converted by the robot communication protocol and stored into a temporary file which is periodically read by the user-defined boundary condition feature.

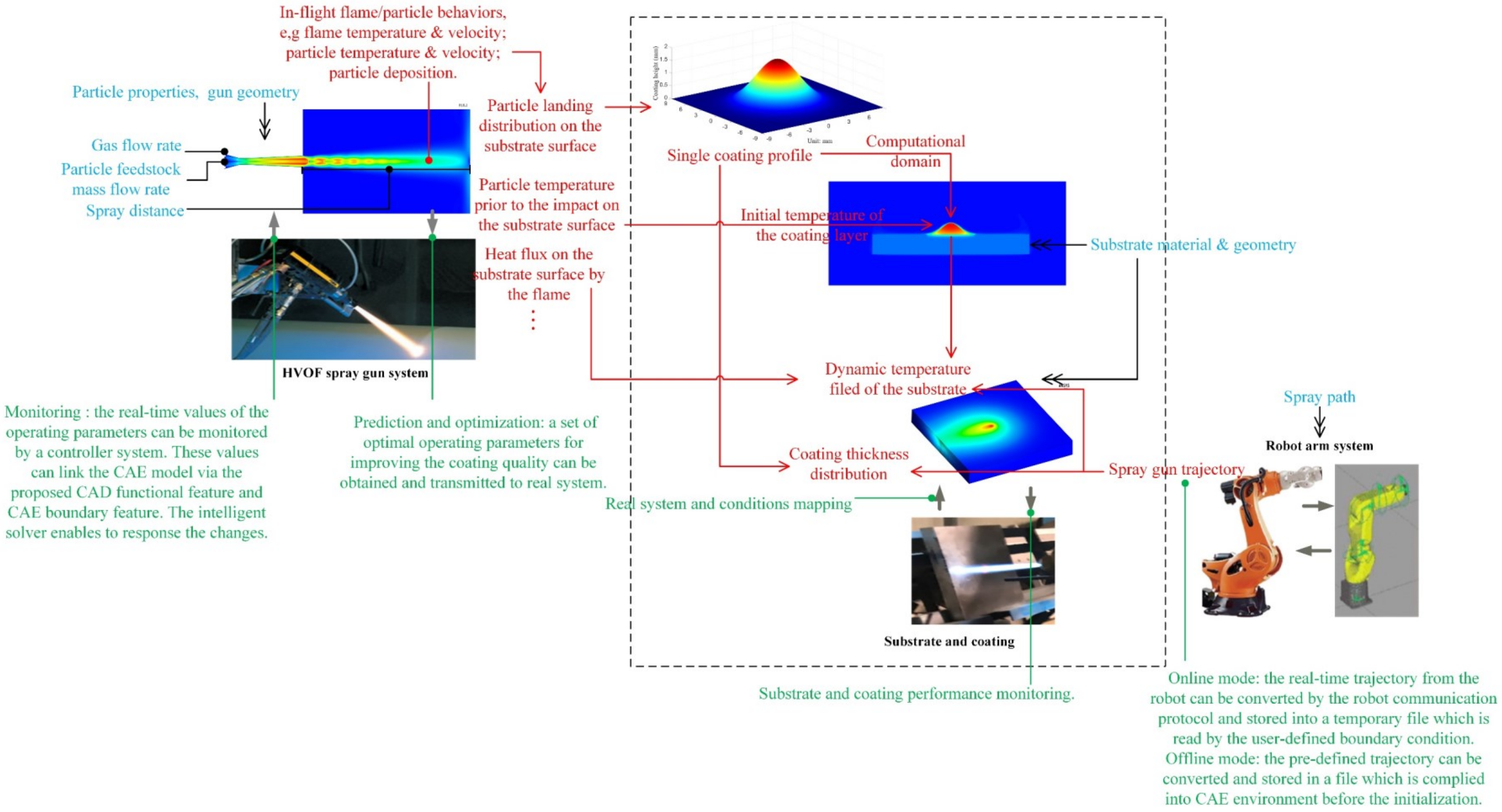

Figure 6.1 A hierarchical key characteristic flow of an industrial HVOF process with the links between the real and virtual world.

According to the above hierarchical characteristic flow, the following subsections present the digital modeling process for the substrate temperature and coating thickness distribution in the scenario given in Figure 6.2 under the proposed feature-based environment. The nozzle started from the left and reciprocated along the spray path with a scanning velocity of 300 mm/s for 10 passes. The building elements and geometries of the spraying nozzle are the same as the ones used in Section 4.6.1, as depicted in Figure 4.6(a) and (b) (which were accurately measured from the real spray gun directly). To provide a mirrored space on the virtual side for the computation, this information was still used in this chapter to construct the in-flight behavior model. Table 6.1 gives the corresponding operating parameters used here, which were obtained from the developed closed-loop and optimization-driven mechanism (Section 4.6.1) and are the optimal solution for improving coating properties, e.g., adhesion, porosity, and deposition efficiency. WC-12Co particles used in Section 4.6 were still used as the feedstock (Table 4.2 presents the thermophysical properties of the particle feedstock and the particle size distribution), which were inputted to the in-flight behavior model and the rule-based coating growth model for obtaining the particle temperature prior to the impact, particle landing distribution, and the single coating profile.

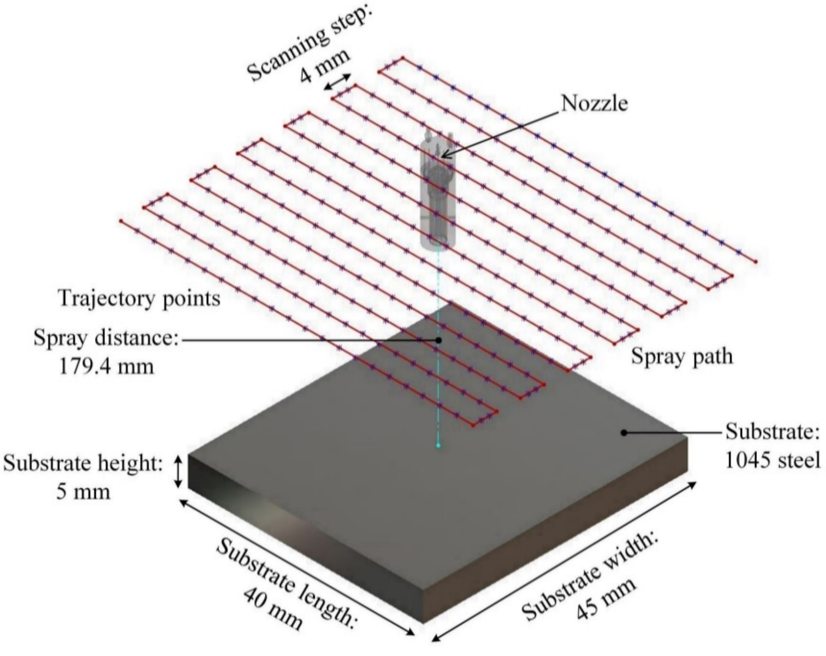

Figure 6.2 A spray path and an AISI-1045 steel substrate.

Table 6.1 A specified set of operating parameters for the demonstration of the phenomenon synchronization.

	Propane flow rate (SLPM)	Oxygen flow rate (SLPM)	Nitrogen flow rate (SLPM)	Air flow rate (SLPM)	Powder feed rate (g/min)	Spray distance (mm)
Operating parameters	180.6	625.6	39.0	577.9	47.1	179.4

6.3 Application of the Real-world Data Processing and Mutual Supports among Different Models

6.3.1 Implementation of the Feature Concepts for the Synchronized HVOF Phenomena

As described in Section 3.4, with the feature-based CAD/CAE integration mechanism, the functional geometry attached in the substrate CAD functional feature can be itemized as the CAE boundary elements enclosing the computational domain. For example, in the substrate temperature model, as shown in Figure 6.3(b), the lateral faces and the bottom face of the substrate are recognized as the boundary condition of a wall with external radiation at room temperature. The face to be coated is recognized as the user-defined boundary due to the change of the coating layer with the progress. The volume enclosed by all faces forms the computational domain. Except for the basic capacity, the substrate CAD functional feature is capable of storing non-geometrical information which is associated with other models and periodically updated via the digital identifier. In this example, it can read LS files from robotic software packages and extract the nozzle trajectory information. Typically, the nozzle trajectory is a series of target points with the corresponding nozzle movement speeds. In terms of these data, for describing the movement of the coverage area of the heat flux from the flame and coating layer, the target points on the nozzle path (nozzle trajectories) are transformed into mapped target points (mapped trajectories) on the substrate surface along with the orientation of the spray nozzle, as depicted in Figure 6.4. Besides, the "non-geometrical data model" associates with two other external models as well, the in-flight behavior model and the transient thermal analysis model of the heat flux from the coating layer to the substrate, so that the physics information can be inputted into the substrate temperature model. All information coming to the substrate CAD functional feature should assign with the faces IDs of the space geometry so that it can be transferred to the corresponding elements in the subsequent views periodically and exactly. Keeping using the same example of nozzle trajectories, these mapped points organized and stored into the non-geometrical information of the substrate CAD functional feature are transferred to the substrate physics feature via the associated geometric entity, the substrate surface to be coated. During this process, the user-defined boundary condition plays a critical role to convert these mapped points to a changing boundary condition of heat flux via a series of data processing. The detailed application of the user-defined boundary condition will be demonstrated in the next subsection.

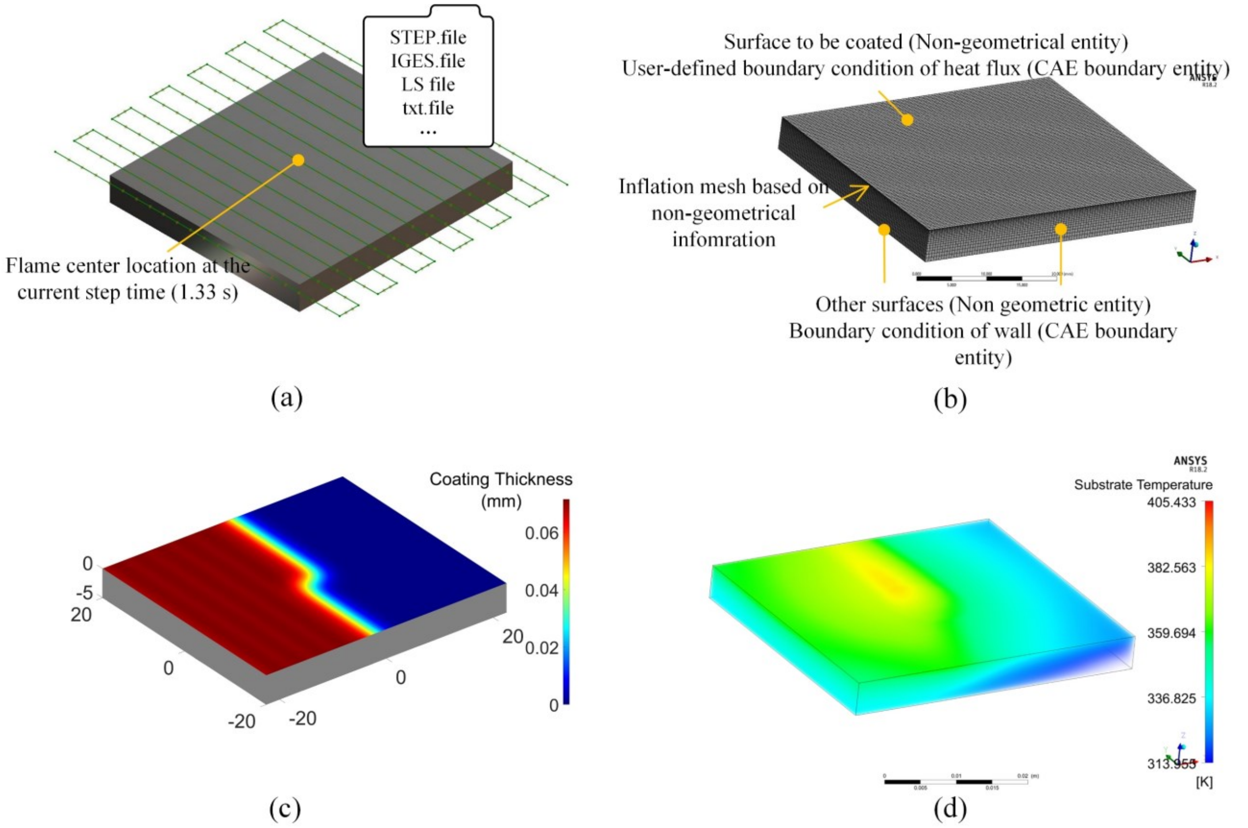

(a) (b)

(c) (d)

Figure 6.3 Schematic representation of the feature conversion in the CAD/CAE integration view and analysis view: (a) partial geometrical entities and non-geometrical information; (b) parametrized CAE boundaries of the domain; (c) the physics feature (coating thickness) at the corresponding time; (d) the physics feature (substrate temperature) at the corresponding time.

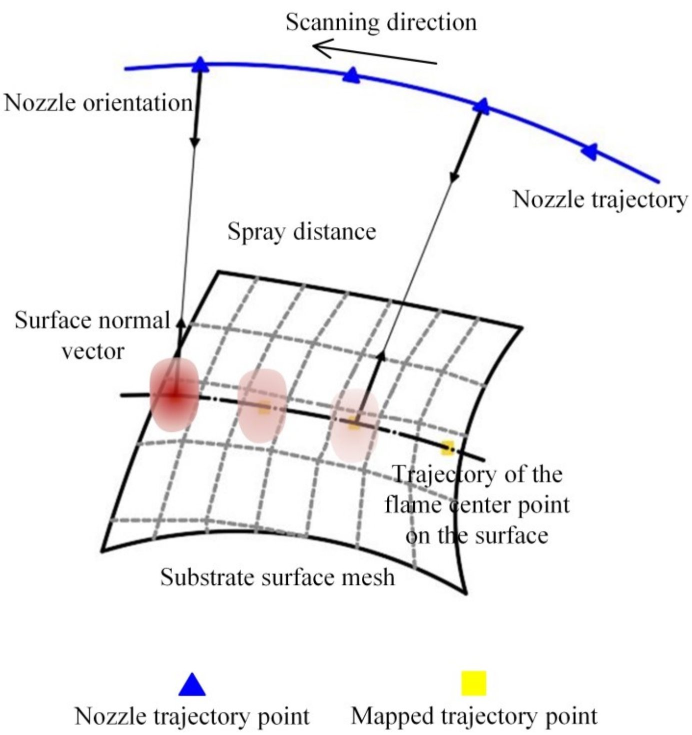

Figure 6.4 Transformation of the nozzle trajectory.

When the computational domain of the substrate component is transfer to the CAE analysis view and the user-defined boundary condition is activated, the solver setup is relatively simple for the temperature simulation. According to the changing boundary condition, the transient model needs to be turned on firstly, which means all parameters are time-dependent. Then the related modeling parameters and the corresponding governing equations for the heat conduction, convection, and radiation should be defined as attributes and constraints in the substrate physics feature separately. Apart from the modular solvers for understanding the phenomenon, the substrate physics feature also guarantees the stability and accuracy of the model via checking grid independence verification. This step can be completed by inspection of plotting the sensitive parameters against the number of nodes [114], or an estimation of the order p of the discretization scheme [115]. Finally, the modular solvers will run before the next view to generate time-periodic simulation results of the substrate temperature field and coating thickness distribution. Figure 6.3(c) and (d) present the coating thickness distribution and the substrate temperature with the specific operating parameters given in Table 6.1 at a moment when the nozzle is passing the point in Figure 6.3(a). These time-periodic results are stored in the phenomenon feature with their time sequence and waited to be further processed in the optimization view. The phenomenon feature also contains the visualization methods of the computational results, which allows the understanding of the data.

After obtaining the data for the physics phenomenon, the last view aims to provide engineering solutions, like coating thickness uniformity optimization and substrate temperature optimization. For example, the thickness uniformity can be optimized via controlling the parameters of scanning velocity, scanning step, and spray distance based on the “surface of equivalent area” theory [140]. However, this falls out of the scope of the case study. This section concentrates on the validation of the feature concepts in the HVOF process and user-defined boundary condition for synchronously associating information from other models.

Finally, a feature-based digital model for describing the coating layer and substrate performance is formed. By connecting with the feature-based digital model of the in-flight behavior (Chapter 4) and robot system, a digital twin class is created. An instance could be generated by carrying out an actual scenario, such as the operating parameters, spray gun, and spray path given at the beginning of this section. A major advantage of implementing these feature concepts is to provide outstanding flexibility. The developed model satisfies the demand of the DT concept on the flexible response to the changing real-world scenario. For example, in the real process, when a different substrate material is used, by replacing the values of the attributes attached to the CAD functional feature, the developed model is able to fast mirror the change in the real process without redundant adjustments.

6.3.2 Application of the User-defined Boundary Condition in HVOF processes

In this study, the user-defined boundary condition proposed in Chapter 3 is to transfer the non-geometrical information from the substrate CAD functional feature, including the mapped trajectory points, heat flux from the deposited coating material, and heat flux from the flame to a time-related boundary condition in a CAE environment for the substrate temperature simulation. As introduced at the beginning of Section 6.2, the temperature is contributed by two components, the heat flux generated by the flame and the heat flux from the coating materials. Due to the revolved structure of the nozzle chamber, the heat flux from the flame has an axisymmetric characteristic. Theoretically, such physics property can be represented by a mathematical function of the radial distance from the flame center on the substrate surface. Through numerical and experimental validations, for most thermal spray processes, the Gaussian distribution can be used to represent this physics property. The coverage area of this Gaussian distribution moves with the trajectory of the flame center point, as shown in Figure 6.5. In this designed user-defined boundary condition, every time step, the flame center location is updated and the amount of the flux on each cell is recalculated. Regarding the heat flux from the deposited coating materials, the difference is that, once they are deposited on the substrate, they continuously heat the substrate until their energy dissipate eventually. To simulate this behavior, the heat flux from the deposited materials is described by a time-related function, like *heat flux source_i* ($\Phi_i(t_i,r_i)$) in Figure 6.5. Once the materials are deposited, the center location of the heat flux from these materials will not change with the movement of the nozzle and this moment will be recorded and set up as the time reference for calculating the amount of heat flux in the subsequent time steps. In the user-defined boundary condition, as illustrated in Figure 6.5, a number of the heat flux sources of the deposited materials for different time steps are coded, where the number is estimated by the time step length and the duration for the energy dissipation of the deposited materials. Every time step the heat flux source of the new deposited materials will replace the oldest one whose energy can be ignorable.

However, the time step in a CAE model may not be the same as the time interval between nozzle trajectory points. To overcome this barrier, the user-defined boundary condition calculates the heat flux source center point at the time steps in the CAE model. Due to the extremely short distance and the time interval between two adjacent nozzle trajectory points, the nozzle movement between the two adjacent points can be assumed to be uniform-rectilinear. Correspondingly, the center location of the heat flux source at the CAE time step can be calculated by Equation (6.1):

$$\begin{gathered}\boldsymbol{X}_s(i) = \boldsymbol{X}_M(k) + \frac{t_T(k+1) - t_T(k)}{t(i) - t_T(k)} \cdot [\boldsymbol{X}_M(k+1) + \boldsymbol{X}_M(k)], \\ t_T(k+1) < t(i) < t_T(k)\end{gathered} \tag{6.1}$$

where $\mathbf{X}_{S}(i)$ is the flame center location on the substrate surface at the i^{th} time step in the CAE model, $\mathbf{X}_{M}(k)$ is the location of the k^{th} mapped trajectory point, $t_T(k)$ is the time corresponding to the k^{th} nozzle trajectory point, $t(i)$ is the time at the i^{th} time step.

Finally, at the current time step, the total heat flux on the substrate surface is the sum of these heat fluxes from the coating materials and the flame. For example, the total heat flux on the surface cell highlighted in green shown in Figure 6.5 is calculated by Equation (6.2):

$$\Phi_{cell}(n) = \Phi_{flame}(r_1(n)) + \sum_{j=1} \Phi_j\big(t_j, r_j(n)\big) \tag{6.2}$$

where $\Phi_{\mathrm{cell}}(\mathrm{n})$ is the total heat flux on the n^{th} surface cell at the current time step, $\Phi_{\mathrm{flame}}(\mathrm{r}_1(\mathrm{n}))$ is the heat flux from the flame, $\mathrm{r}_1(\mathrm{n})$ is the distance from the cell location to the flame center, this distance is also the distance from the cell location to the center location of the heat flux from the newest deposited materials, $\Phi_{\mathrm{j}}(\mathrm{r}_{\mathrm{j}}(\mathrm{n}))$ is the heat flux from the coating materials which are deposited at previous time steps, and $r_j(n)$ is the distance from the cell location to the center location of the heat flux from deposited materials.

The pseudocode of the user-defined boundary condition for the scenario above is provided in Appendix 5.

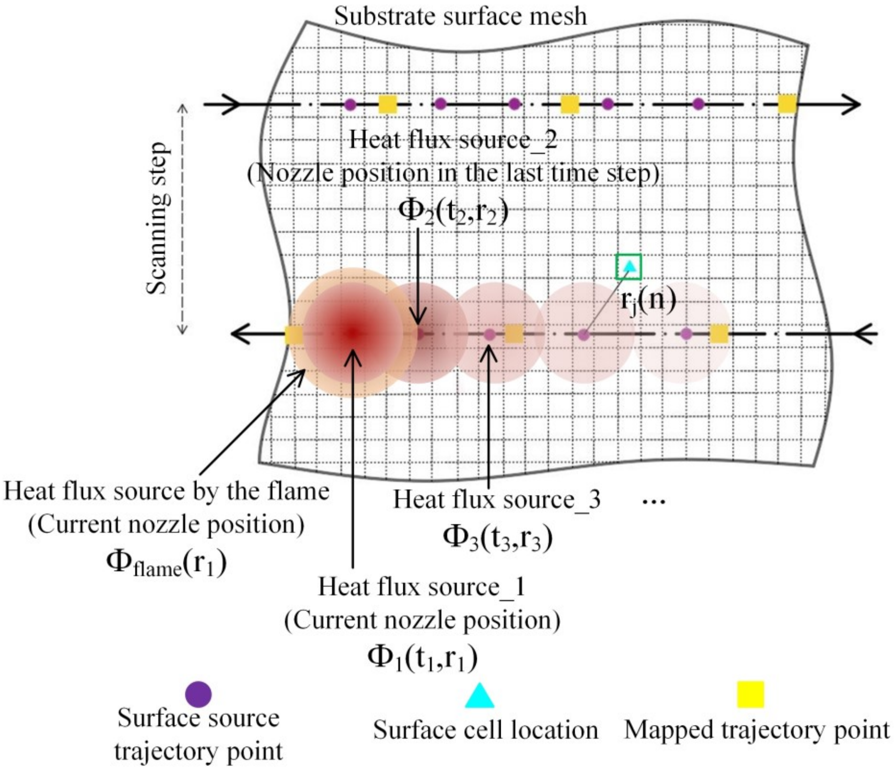

Figure 6.5 Schematic representation of the user-defined boundary condition.

Regarding the coating thickness calculation, the mechanism is similar. The flame heat flux source on the substrate surface can be replaced by a single coating profile (typically in the thermal spray process, a Gaussian distribution is widely used to describe this profile). Then the transient coating thickness distribution on the substrate surface can be calculated according to the algorithm given in 5.2.4.

6.3.3 Synchronization of Nozzle Trajectory, Coating Thickness Growth, and Substrate Temperature Distribution

Based on the works in Chapter 4 and Chapter 5, the operating parameters in Table 6.1 were inputted to the in-flight behavior model for computing the behaviors of the fuel-oxidant combustion and flame jet. Then, the particle size range in Table 4.2 was discretized into 30 groups of different particle diameters. Appendix 3 is the MATLAB code for discretizing the particle size distribution. As shown in Figure 6.6, the discretized particle sizes are marked by the orange circles and the star signs are the measurement result from a laser diffraction analyzer. These particle groups were separately inserted into the obtained flame model for computing the particle landing distribution on the substrate surface, meanwhile, the thermal thermophysical properties in Table 4.2 were correspondingly set up in this model for accurately simulating the in-flight behavior of the particles. With the particle landing distribution, the particles' morphology after impacting and coating growth was modeled based on the series of rules introduced in Section 5.2.2.1. Finally, a 3D single coating thickness profile model was developed by constructing a circular pattern using the axis of the nozzle. Further, this profile was smoothened by a Gaussian model and its mathematical expression was obtained in Equation (6.3).

$$\varphi = 2.955 \times 10^{-3} e^{-\left(\frac{\left(x^2+y^2\right)^{1/2}-1.665\times10^{-5}}{3.016\times10^{-3}}\right)^2} \tag{6.3}$$

To estimate the change of the heat flux from the deposited materials with time, this single coating profile formed a computational domain of a transient thermal analysis model. As shown in Figure 6.7(a), due to the axisymmetric profile of the single coating model, a 2D axisymmetric model was used to reduce the computation cost. The shape of the cell zone of the coating was generated according to the obtained Gaussian function (Equation (6.3)). The thermal thermophysical properties of WC-12Co were assigned to the coating zone. The bottom of the coating zone contacts with a zone assigned with the substrate material, AISI-1045 steel. The height of the substrate zone is 5 mm, which is the same as the height in the aforementioned scenario. The coating and substrate zone were enveloped by an external flow zone which was filled with air. The radial extent of the external flow field was chosen to be twice the substrate width. The coating zone was initialized with a temperature of 1523 K, which was the temperature of the powder particles prior to the impact on the substrate surface. As the coverage area of the flame on the substrate surface is larger than the coating distribution, the substrate is heated by the flame for a short period before the deposition of the particles. Therefore, the temperature of the substrate zone was initialized with a value of 350 K. The surrounding air was initialized with a temperature of 300 K. For exactly capturing the change of the heat flux on the substrate surface, the time step for the transient analysis was set up as 0.005 s. Figure 6.7(b)-(f) show the temperature contour of the coating layer and the substrate at 0.005 s, 0.025 s, 0.05 s, 0.075 s, and 0.1 s separately.

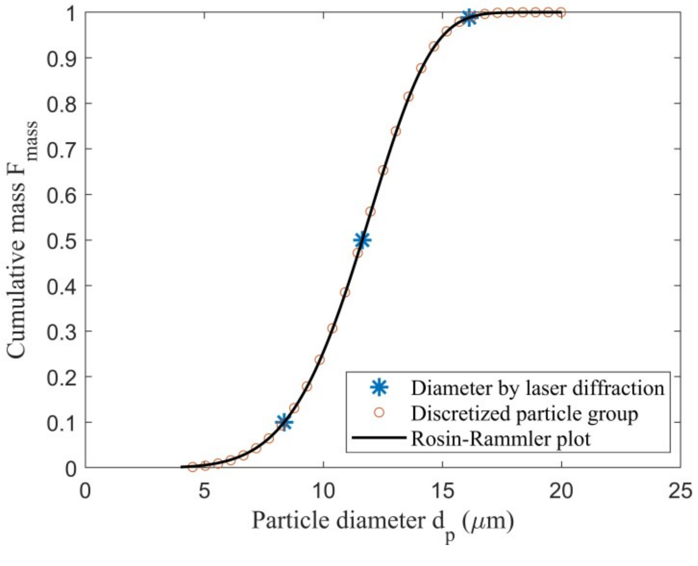

Figure 6.6 Cumulative mass distribution of the WC-12Co powder particles and particle size discretization for the demonstration of the phenomenon synchronization.

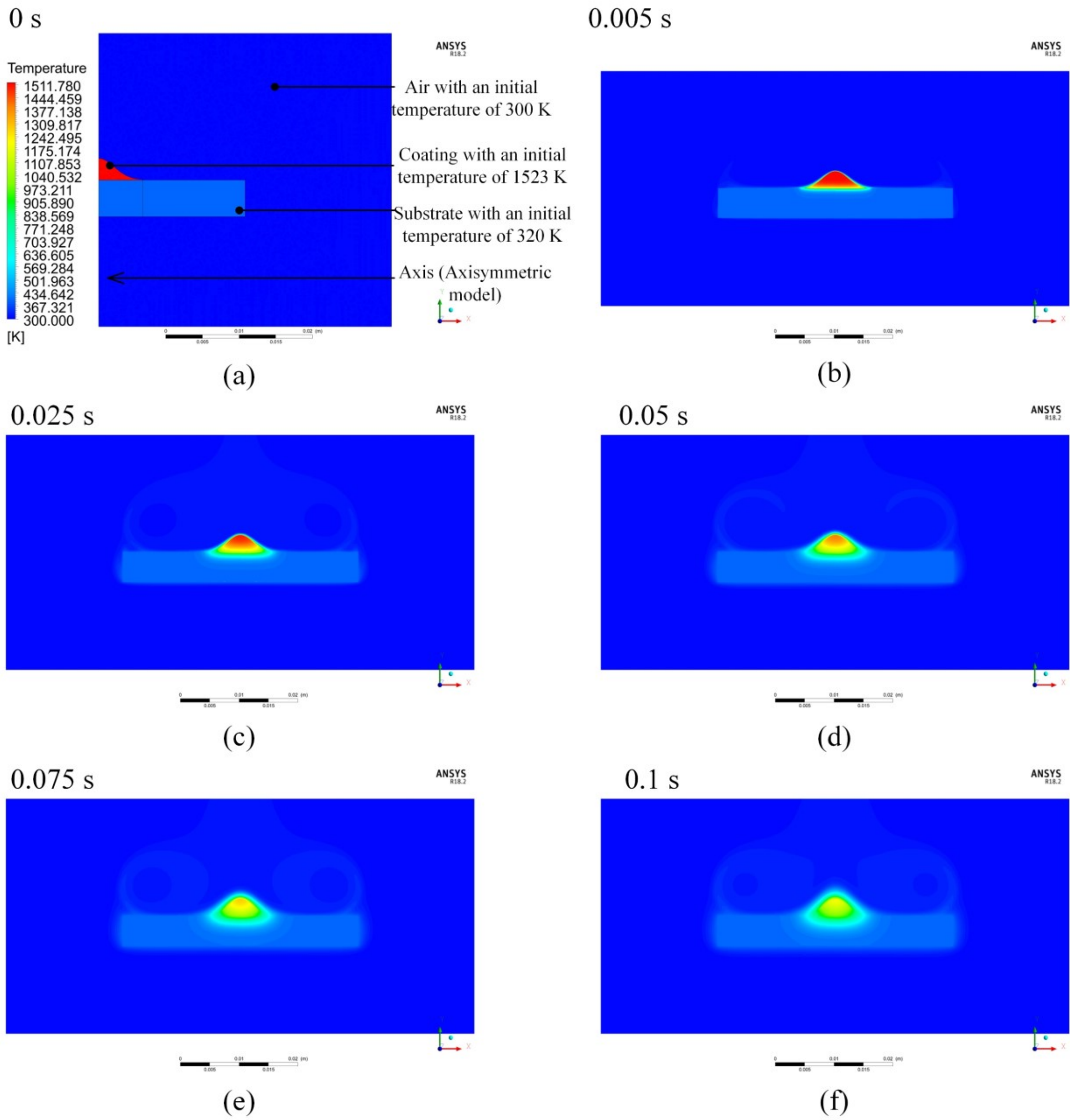

(a) (b) (c) (d) (e) (f)

Figure 6.7 Transient temperature contour of the coating layer and the substrate: (a) initial conditions of the model; (b) temperature contour at 0.005 s; (c) temperature contour at 0.025s; (d) temperature contour at 0.05 s; (e) temperature contour at 0.075 s; (f) temperature contour at 0.1 s.

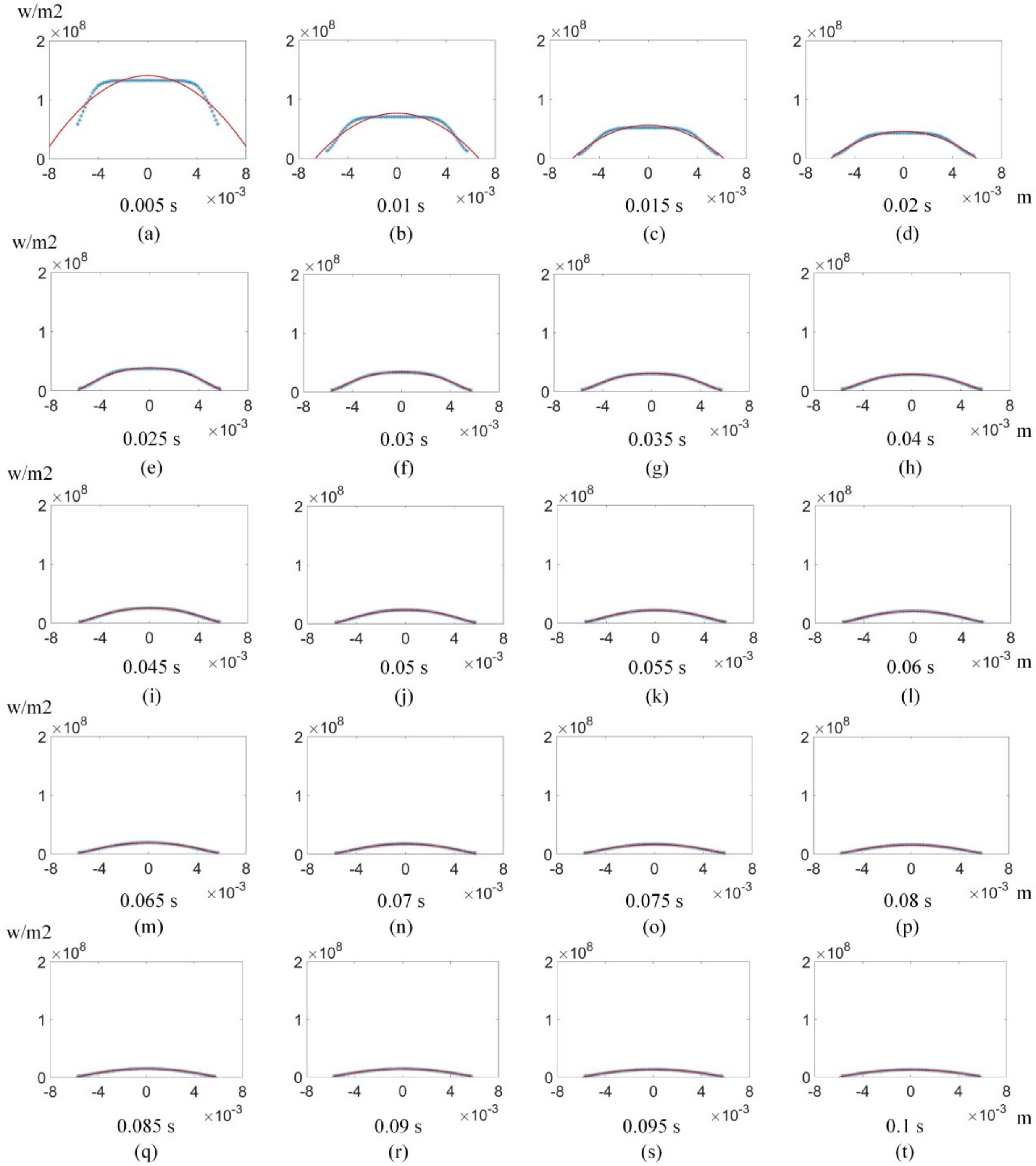

0.005 s (a) 0.01 s (b) 0.015 s (c) 0.02 s (d)

0.025 s (e) 0.03 s (f) 0.035 s (g) 0.04 s (h)

0.045 s (i) 0.05 s (j) 0.055 s (k) 0.06 s (l)

0.065 s (m) 0.07 s (n) 0.075 s (o) 0.08 s (p)

0.085 s (q) 0.09 s (r) 0.095 s (s) 0.1 s (t)

Figure 6.8 Heat fluxes on the coating-substrate interface at different moments.

Further, to associate this transient model with the substrate temperature simulation, the data of the transient heat fluxes at more moments were extracted from the log file recording the transient physics property. The blue star signs in Figure 6.8 are the node values of the heat flux on the interface. The x axis is the radial distance from the center of the coating profile and the y axis is the heat flux at the corresponding location. Here only the heat flux in the first one-tenth second is used since the heat flux after this time is too short when compared with the value in the first one-tenth second. To save the computational resource, its effect on the substrate temperature can be ignorable. For this physics property at different moments, it is obvious that a second-order polynomial function, as Equation (6.4), is able to represent the relationship between the heat flux and the radial distance, where the coefficients of the function should be changed with time.

Therefore, the data presented in Figure 6.8 were used to fit the second-order polynomial model, and the coefficients corresponding to different moments were further recorded as marked by the blue star signs in Figure 6.9. To mathematically represent this changed heat flux, the changes of its coefficients with time were modeled by several functions, like the second-order polynomial function, the Gaussian function, and the exponential function. By the visual investigation, the exponential function provided a best fitting result and was used to model these changes, as shown by the black line in Figure 6.9. The x axis is the time in the transient model and the y axis is the value of the coefficients. The regression models are expressed as Equations (6.5)-(6.7).

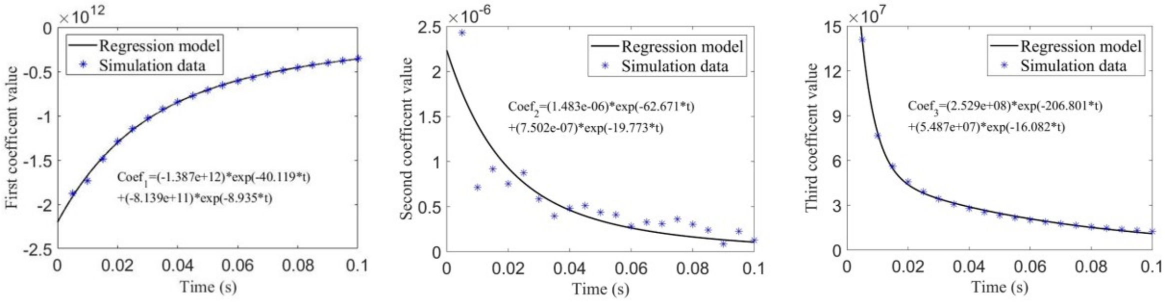

(a) (b) (c)

Figure 6.9 Regression models of the coefficients of the heat flux from the coating materials.

$$\Phi_j\big(t_j, r_j(n)\big) = Coef_1\big(t_j\big) * r_j(n)^2 + Coef_2\big(t_j\big) * r_j(n) + Coef_3\big(t_j\big) \tag{6.4}$$

where,

$$Coef_1\big(t_j\big) = -1.387 * 10^{12} * e^{\left(-40.119 * t_j\right)} - 8.139 * 10^{11} * e^{\left(-8.935 * t_j\right)} \tag{6.5}$$

$$Coef_2\big(t_j\big) = 1.483 * 10^{-6} * e^{\left(-62.671 * t_j\right)} + 7.502 * 10^{-7} * e^{\left(-19.773 * t_j\right)} \tag{6.6}$$

$$Coef_3\big(t_j\big) = 2.529 * 10^{8} * e^{\left(-206.801 * t_j\right)} + 5.487 * 10^{7} * e^{\left(-16.082 * t_j\right)} \tag{6.7}$$

The heat flux generated by the flame was extracted from the boundary condition of the wall in the static in-flight behavior model. Through an iterative coupling method (which will be introduced and verified in Section 6.4), this heat flux is precisely expressed as Equation (6.8).

$$\begin{aligned}\Phi_{flame}(r_1(n)) = {} & 6.18 * 10^3 * e^{-\left(\frac{r_1(n)-8.81*10^{-10}}{1.26*10^{-4}}\right)^2} + 40716.15 * e^{-\left(\frac{r_1(n)-6.94*10^{-7}}{4.80*10^{-3}}\right)^2} \\ & + 3.51 * 10^5 * e^{-\left(\frac{r_1(n)-10.00*10^{-7}}{0.01}\right)^2} + 1.75 * 10^5 * e^{-\left(\frac{r_1(n)-6.42*10^{-3}}{0.02}\right)^2} \\ & + 1.67 * 10^5 * e^{-\left(\frac{r_1(n)-6.76*10^{-3}}{0.02}\right)^2} + 4.30 * 10^5 * e^{-\left(\frac{r_1(n)-1.99*10^{-7}}{0.05}\right)^2}\end{aligned} \tag{6.8}$$

Under the feature-based environment, all the above information was stored into a common data model named "model specifications" (non-geometric information) and permanently stored as data files which can be updated periodically by other models, like the transient thermal analysis model and the static in-flight behavior model. After converting this special knowledge into mathematical expressions, the user-defined boundary condition can identify this data via the associated geometrical entity (the substrate surface to be coated). The mechanism introduced here has been coded in C language, which was embedded in the user-defined boundary condition. All algorithms have been parametrically designed in this code so that the data, like the coefficients from the other models, can be directly implemented in a CAE environment. Finally, in the programming, by substituting Equations (6.4)-(6.8) into Equation (6.2), the boundary condition of the heat flux was yielded. The transient temperature simulation of the substrate was constructed via loading this boundary condition in the corresponding thermal analysis models. In this case study, the thermal analysis was solved by ANSYS Fluent [141]. The code for constructing the changed boundary condition was compiled by ANSYS Fluent. Besides, by substituting Equation (6.3) into Equation (5.13) and setting up the same time step, a synchronized coating thickness distribution was also obtained. For acquiring the continuous physics phenomena and reliable transient results, a time step of 0.01 seconds was used in this case study. Figure 6.10 just shows the synchronized coating thickness distribution and the substrate temperature at partial moments. The maximum temperature of the substrate reaches 1032.709 K. The range of the substrate temperature at the end of the process is 67.437 K. The maximum thickness is 0.7142 mm and the maximum thickness tolerance is 0.0293 mm.

From the above demonstration, excellent comprehensiveness is achieved by executing the user-defined boundary condition feature, which caters to the demand of the DT concept on high fidelity and comprehensiveness. Concerning the model capacity of timeliness, a single time step for the substrate temperature simulation on a 4-core parallel-processing CPU with the residuals of absolute criteria of $10e^{-8}$ needs around 0.01 s, which is close to the time step size (0.01 s). Thus, the model even on a low-performance CPU is able to support a near-real-time physics phenomenon synchronization with an approximate 0.01 s delay.

On the basis of the near-real-time physics phenomenon synchronization, when an online trajectory planning (as depicted in Chapter 3 by the left flow in Figure 3.3) has to be carried out, every CAE time step, the digital model is capable of carrying out the synchronization of the substrate temperature and coating thickness distribution via adding the data transmission with an ignorable delay. That means, without expensive temperature and contour measuring equipment, the digital model enables the monitoring of the substrate temperature and coating thickness distribution on the virtual side.

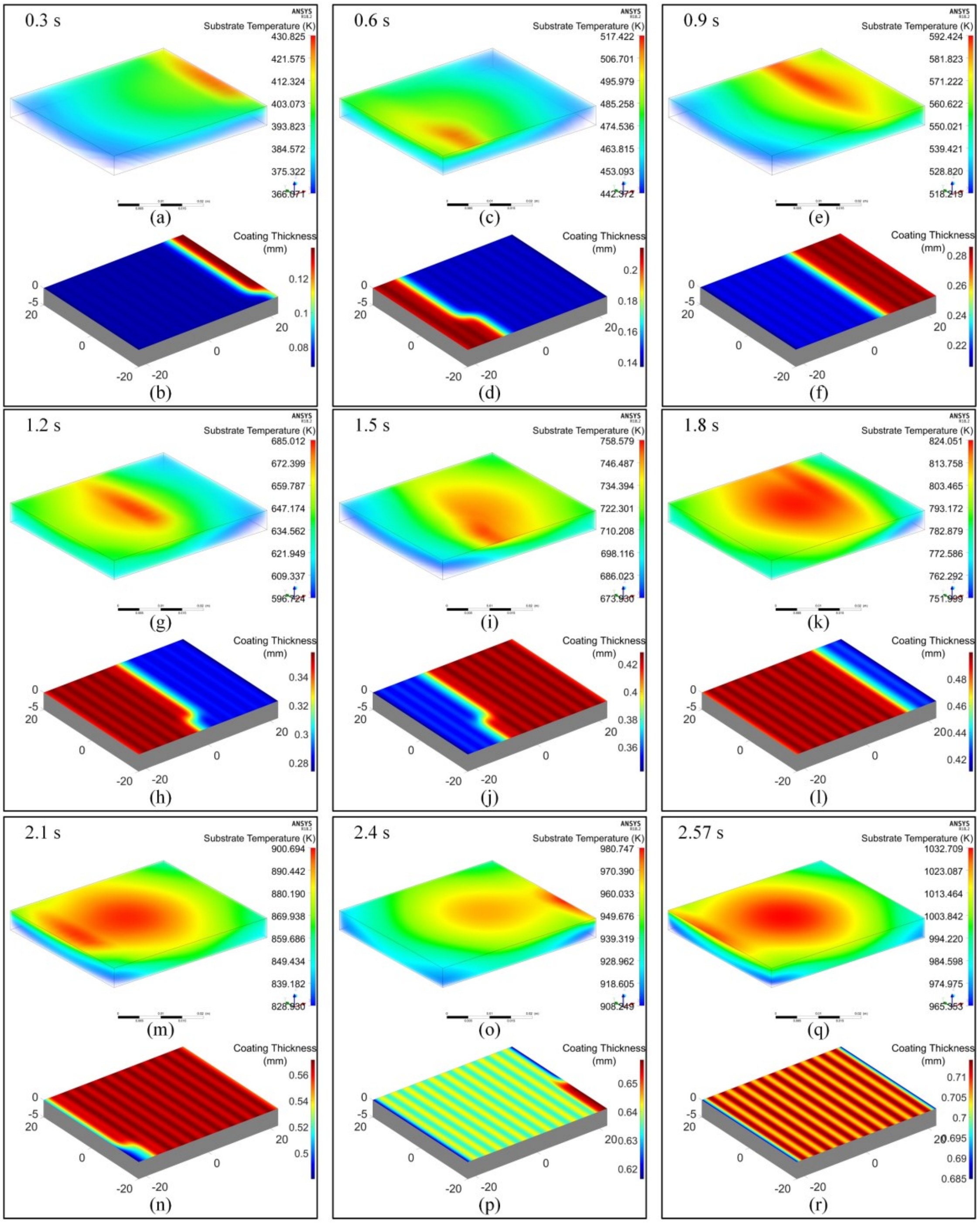

Figure 6.10 Synchronized coating thickness distribution and the substrate temperature: (a) substrate temperature at 0.3 s; (b) coating thickness at 0.3 s; (c) substrate temperature at 0.6 s; (d)

coating thickness at 0.6 s; (e) substrate temperature at 0.9 s; (f) coating thickness at 0.9 s; (g) substrate temperature at 1.2 s; (h) coating thickness at 1.2 s; (i) substrate temperature at 1.5 s; (g) coating thickness at 1.5 s; (k) substrate temperature at 1.8 s; (l) coating thickness at 1.8 s; (m) substrate temperature at 2.1 s; (n) coating thickness at 2.1 s; (o) substrate temperature at 2.4 s; (p) coating thickness at 2.4 s; (q) substrate temperature at 2.57 s; (r) coating thickness at 2.57 s.

In addition, by adding some assessment criteria for the physics performance into the code, the developed model is capable of providing signals for detecting operating errors or unexpected working performances. Further, with the implementation of the optimization view, the model enables the real-time adjustments of the real process for achieving an ideal working performance. With the assistance of a feedback controlling system, the derived solutions could be translated to execution signals which command the actuators to carry out them on the real side. For instance, as shown in Figure 6.11, when powder particles have been selected, the static in-flight behavior model derives the optimal operating parameters for reaching the best behavior of the particles [129]. These parameters are carried out by the gas flow controller. The feature-based digital model for the coating layer and substrate mirrors the real-world performance with a near-real-time capacity. If the substrate temperature reaches a critical range of damaging the substrate material, the model could provide an alarm signal to the controller. By adding some optimization algorithms, the model could also provide real-time feedback to the robot controller for adjusting the trajectory so that the substrate temperature is timely controlled within a reasonable range. If the substrate temperature is reasonable, the model could further optimize the parameters for obtaining a uniform coating layer. For example, with the "surface of equivalent area" theory, the overlapping of the single Gaussian coating profile on the substrate surface is optimized to generate a uniform coating thickness via adjusting the operating parameters, such as gas flow rates, spray distance, scanning velocity, scanning step and so on. In the future, with the assistance of physical properties, this ideal cyber-physical system can be realized without many enhancements to the virtual side.

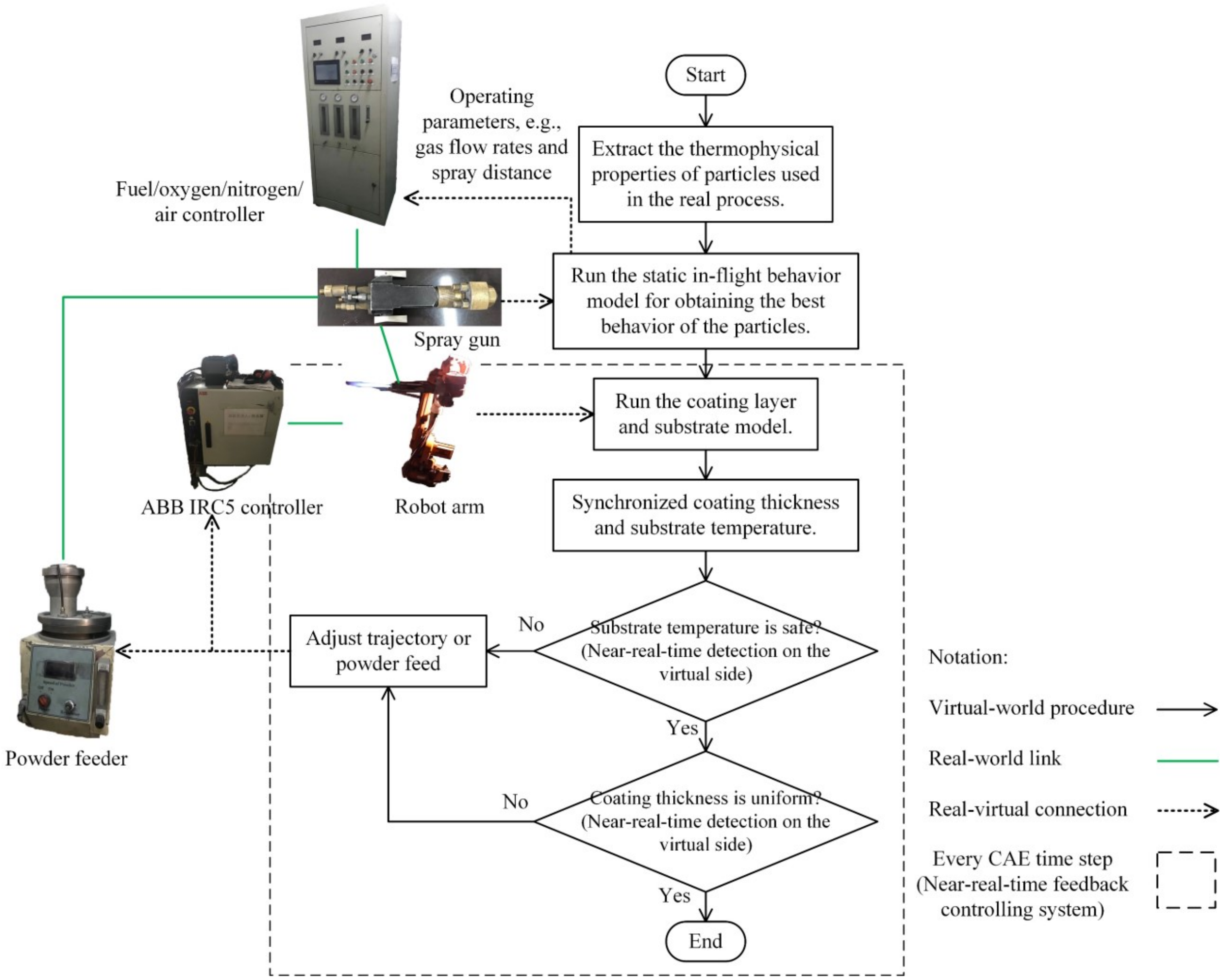

Figure 6.11 A proposed DT setup of the developed model.

6.4 A Branch of This Work: The Comparison of Two Turbulence Models for the Dynamic Temperature Performance of HVOF Process

During the HVOF process, the flame is forced to impact the substrate, which leads to a sharp rise in the substrate temperature. To avoid residual stress due to a sharp change in the temperature, the thermal prediction of the substrate is noticeable. In this section, the substrate temperature heated by the flame will be precisely simulated and verified by experimental data.

The convective heat transfer between the flame flow and substrate surface is related to two dynamic properties of the reactive flow, the velocity and temperature functions, which are affected by the turbulence model selection due to the high Reynolds and Mach numbers of the flame flow [77,83]. In the previous research works, the renormalization group (RNG) k-ε turbulence models [72] or the realizable k-ε turbulence models [6] were widely used to estimate the turbulent eddy viscosity. However, to the author's best knowledge, in the HVOF process, the best-fit turbulence model for the substrate heating by the flame has not been studied thoroughly. Before comparing these two turbulence models, to improve the robustness of the simulation result, an iterative method to calculate the dynamic characteristics of the substrate by coupling the in-flight behavior and dynamic coating process modeling is developed in this section. Regarding other turbulence models, although some of them present better results in some cases of turbulence simulations and researchers tried to use them to simulate thermal spray processes, for example, the Reynolds stress equation model (RSM) has been used to simulate the plasma spray process [142], these models have not been widely accepted in the area of the HVOF modeling [79]. Thus, this study does not consider these models.

6.4.1 Methodology

6.4.1.1 An Iterative Coupling Method

In order to coherently capture the full dynamic substrate temperature during the HVOF process, the iterative coupling method consisting of two stages, the in-flight behavior and dynamic coating process model, is illustrated in Figure 6.12, which enables the dynamic sharing of the parametric data of the flame jet physics characteristics from the in-flight behavior model with the dynamic coating process model.

The first stage is the same as the procedure of the intelligent solver for the feature-based in-flight behavior modeling (which is introduced in Section 4.4). Some steps have been omitted here for brevity. For a detailed illustration, the reader could refer to Figure 4.4. Once the in-flight behavior model reaches a certain stable state, in the second stage, the flame properties could be extracted and further fed to calculate the dynamic coating performance with the progress of a spray path. To achieve this purpose, the in-flight properties are converted into corresponding physics fields on the substrate surface, e.g., heat flux. Typically, this physics field is symmetrical about the centerline of the flame due to the axisymmetric nozzle shape, and a Gaussian distribution is used to model the distribution of these properties on the substrate surface [83,90,143]. For searching a best-fitting Gaussian model, several criteria are used to assess the model, such as coefficient of determination (R2), Mean Absolute Error (MAE), and Root Mean Squared Error (RMSE). The spray path is transformed into a mapped path on the substrate surface along with the orientation of the spray gun, as depicted in Section 6.3.2. Then the corresponding dynamic temperature of a substrate can be computed by linearly discretizing the physics field center path at the time step of CFD tools, which also has been elucidated in detail in Section 6.3.2.

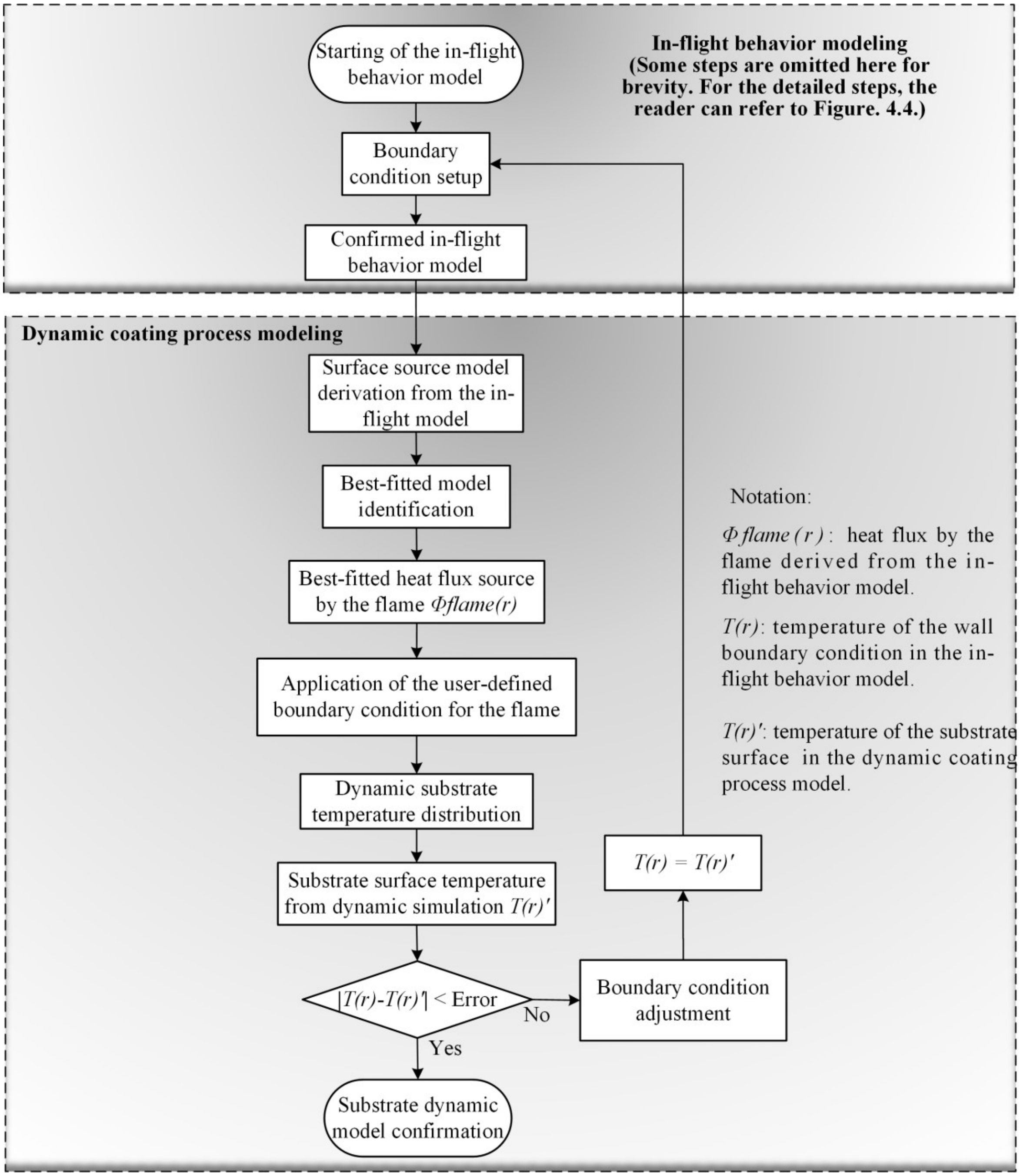

Figure 6.12 Flow chart of the iterative coupling method.

However, the temperature behavior from the dynamic coating process simulation and the corresponding one from the in-flight model may be inconsistent, because the temperature behavior from the dynamic coating process simulation is affected by the physics field derived from the in-flight model, and the derivation of the physics field relies on the state of the boundary condition of the substrate surface in the in-flight model which is unknown beforehand and expected to obtain from the dynamic coating model. To make up the gap, the boundary condition in the in-flight model is assigned a presumptive or ideal state to get a starting point for calculating the physics field. After obtaining the dynamic coating process model by using this physics field, the temperature field from the dynamic coating process simulation replaces the presumptive or ideal boundary condition in the in-flight HVOF model to recalculate the physics field, as depicted in Figure 6.12. Several iterations of this part will be carried out until an acceptable error between the property from these two models is reached. In this work, the acceptable error is simply assessed by visual inspection of plotting these properties. In this way, the dynamic physics of the coating can be captured accurately.

6.4.1.2 Turbulence Models to be Compared

It is obvious that, from the explanation of the in-flight behavior modeling in Chapter 4, the turbulence model has a remarkable influence on the simulation result of the in-flight behavior which further affects the accuracy of the substrate dynamic simulation. In this section, the RNG k-ε turbulence model and the realizable k-ε turbulence model are implemented separately with the above coupling method to investigate the effects on the dynamic behavior of the substrate, and then a better one to be chosen. According to the Boussinesq hypothesis [15],[16], the Reynolds stress term representing the effect of turbulence [18] in the governing equations can be related to the mean velocity gradients:

$$-\overline{\rho v_i'' v_j''} = \mu_t \left(\frac{\partial \tilde{v}_i}{\partial x_j} + \frac{\partial \tilde{v}_j}{\partial x_i} \right) - \frac{2}{3} \left(\bar{\rho} k + \mu_t \frac{\partial \tilde{v}_l}{\partial x_l} \right) \delta_{ij}, \tag{6.9}$$

where μ_t is the turbulent viscosity and k is the turbulence kinetic energy.

To estimate the effect of turbulence, the RNG *k-ε* turbulence model has the following form [72]:

$$\frac{\partial}{\partial t}(\bar{\rho}k)+\frac{\partial}{\partial x_i}(\bar{\rho}\tilde{v}_i k)=\frac{\partial}{\partial x_j}\left[\alpha_k(\mu+\mu_t)\frac{\partial k}{\partial x_j}\right]+G_k-\bar{\rho}\varepsilon-Y_M, \tag{6.10}$$

$$\frac{\partial}{\partial t}(\bar{\rho}\varepsilon)+\frac{\partial}{\partial x_i}(\bar{\rho}\tilde{v}_i\varepsilon)=\frac{\partial}{\partial x_j}\left[\alpha_\varepsilon(\mu+\mu_t)\frac{\partial \varepsilon}{\partial x_j}\right]+C_{1\varepsilon}\frac{\varepsilon}{k}G_k-C_{2\varepsilon}\bar{\rho}\frac{\varepsilon^2}{k}-R_\varepsilon, \tag{6.11}$$

where ε is the turbulence dissipation rate, G_k is the generation of turbulent kinetic energy arising from the mean velocity gradients, and Y_M is the contribution of the fluctuating dilatation in compressible turbulence to the overall dissipation rate. α_k and α_ε are inverse effective Prandtl numbers for the turbulent kinetic energy and its dissipation. R_ε is an additional term in the ε equation. $C_{1\varepsilon} = 1.42$, $C_{2\varepsilon} = 1.68$.

The transport equations of the realizable *k-ε* turbulence model are [77]:

$$\frac{\partial}{\partial t}(\bar{\rho}k)+\frac{\partial}{\partial x_j}\left(\bar{\rho}\tilde{v}_j k\right)=\frac{\partial}{\partial x_j}\left[(\mu+\frac{\mu_t}{\sigma_k})\frac{\partial k}{\partial x_j}\right]+G_k-\bar{\rho}\varepsilon-Y_M, \tag{6.12}$$

$$\frac{\partial}{\partial t}(\bar{\rho}\varepsilon)+\frac{\partial}{\partial x_j}\left(\bar{\rho}\tilde{v}_j\varepsilon\right)=\frac{\partial}{\partial x_j}\left[(\mu+\frac{\mu_t}{\sigma_\varepsilon})\frac{\partial \varepsilon}{\partial x_j}\right]-\bar{\rho}C_2\frac{\varepsilon^2}{k+\sqrt{v\varepsilon}}, \tag{6.13}$$

where ε, G_k, and Y_M have the same definitions as the RNG turbulence model. σ_k and σ_ε are the turbulent Prandtl numbers for k and ε, respectively. $C_2 = 1.9$, $\sigma_k = 1.0$ and $\sigma_\varepsilon = 1.2$.

From the above equations, there are three major differences between the two models: the turbulent Prandtl numbers for k and ε; the generation and destruction terms in the equation for ε; and the method of calculating turbulent viscosity. In Section 6.4.3, the substrate temperature obtained from the dynamic simulations by these two models will be compared with experimental results.

6.4.2 Experimental Procedure

To validate the modeling method and compare the accuracy of the two turbulence models, dedicated experiments were carried out and the common setup is shown in Figure 6.13, consisting of an infrared thermometer (SCIT-3S7, Beijing Sanbo Zhongzi Technology Co., Ltd), and a homemade Diamond Jet spray system with ABB IRC5 M2004 robot system. The temperature at the center point on the top surface of an AISI-1045 steel substrate (300 mm × 300 mm × 30 mm) was continuously measured by the infrared thermometer during the process. A Diamond Jet HVOF nozzle carried by the robot arm moved along the centerline of the top surface with a pre-defined spray distance and scanning velocity, which is the same as the path depicted in Figure 5.14. The nozzle orientation was always perpendicular to the substrate surface during the movement. The same homemade Diamond Jet Hybrid gun as shown in Figure 4.6(a) and (b) was still used in this experiment. Two sets of operation conditions, as shown in Table 6.2, were carried out with two scanning velocities, 5 mm/s and 10 mm/s. It is worth noticing that for the sake of the convenience of temperature measurement in the experiment, the spray velocity used here is quite lower than the real industrial process and all the spray processes were carried out without powder particles. It should also be noted that Condition 2 is the optimal solution obtained from the developed feature-based in-flight behavior model. The experiment results are presented and compared with the simulation results in the next section (Section 6.4.3).

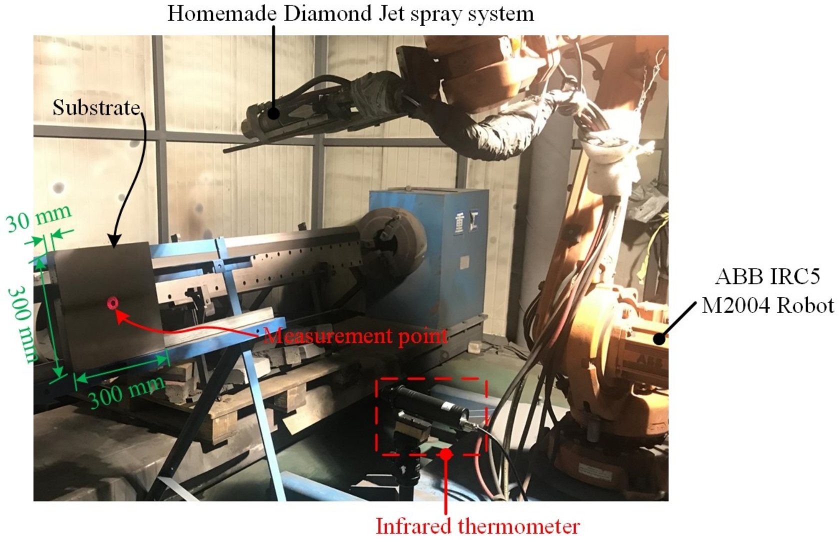

Figure 6.13 Experimental temperature measurement of the substrate surface.

Table 6.2 Simulation and experiment operating parameters.

Operating parameters	Propane flow rate (SLPM)	Oxygen flow rate (SLPM)	Nitrogen flow rate (SLPM)	Air flow rate (SLPM)	Spray distance (mm)
Condition 1	334.6	972.0	32.8	758.1	170.0
Condition 2	180.6	625.6	39.0	577.9	179.4

6.4.3 Results and Discussion

Regarding the simulation, two sets of operating conditions as shown in Table 6.2 were conducted in the developed in-flight behavior model to simulate the flame behavior. Then, the dynamic temperature field behavior of the AISI-1045 steel substrate with the two different scanning velocities (5 mm/s and 10 mm/s) were simulated based on the aforementioned spray path integration mechanism with the coupling algorithm. To illustrate the coupling method in detail, Condition 2 in Table 6.2 with a 5 mm/s scanning velocity is used as a sample here to explain the procedure for getting the simulation result.

For exactly calculating the heat flux, the substrate surface at the right end of the domain of the flame, as shown in Figure 4.6(c) was set up as a wall boundary condition with the material properties of AISI-1045. The thickness of the wall boundary condition was adjusted to 30 mm which is the same as the thickness of the substrate. Regarding the temperature of this boundary condition, the room temperature was presumed to get a starting point for calculating the heat flux on the substrate surface. The chamber wall is cooled by water. Its boundary condition was set up as a constant temperature of 300 K for the purpose of simplification. Once the in-flight model has been completely set up, the heat flux by the flame can be extracted from the simulation results. Figure 6.14(a) presents a temperature contour of the flame flow by using the RNG turbulence model.

In the dynamic coating process modeling, the obtained heat flux was derived and converted to a best-fitted Gaussian-distribution physics field. Then, by implementing the user-defined boundary condition feature, the dynamic temperature field of the substrate with the spray path was calculated at the time step of the CAE environment. However, the initial round computation result is inaccurate because the heat flux was derived based on a hypothetical boundary condition of the substrate surface of the in-flight model (room temperature). To fix this issue, the instantaneous temperature field from the dynamic coating process model corresponding to the moment when the torch moves to the center point of the top surface was reassigned into the simulation model as the boundary condition of the in-flight model to recalculate the heat flux and the temperature field of the dynamic coating process model, as depicted in Figure 6.14(a) and (b). This procedure was carried out iteratively until the heat flux dynamic properties become stabilized into an acceptable range, as shown in Figure 6.14(c). Consequently, a converged dynamic temperature field of the substrate could be obtained.

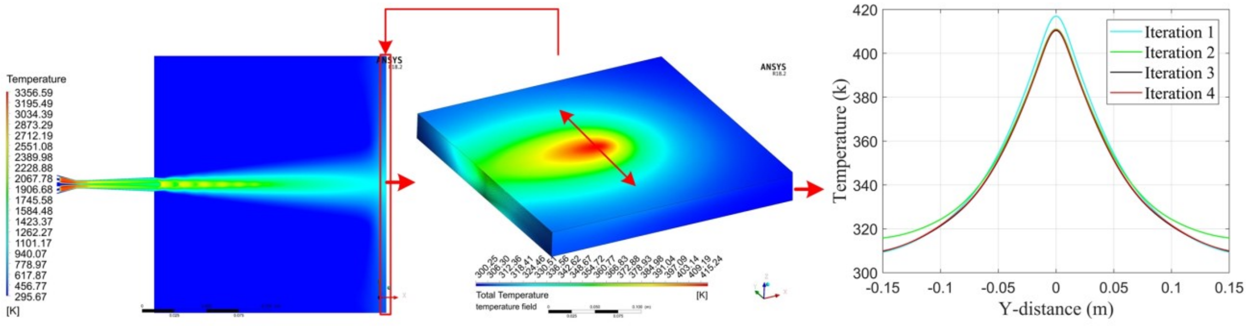

(a) (b) (c)

Figure 6.14 Schematic representation of the key steps during the modeling of Condition 2 with the RNG turbulence model and 5 mm/s scanning velocity: (a) the temperature contour of the flame flow; (b) the instantaneous temperature field corresponding to the moment when the torch moves to the center point of the top surface; (c) the iteration result of the instantaneous temperature field.

According to the procedure above, the two sets of operating conditions given in Table 6.2 with two different scanning velocities were all computed. Figure 6.15 shows the temperature of the center point changes over time. The profiles from the simulation results and experimental measurements present the same variation trend. The temperature of the measurement point increases sharply and reaches a peak value when the torch moves toward it. After the peak, the profiles experience a gradual decrease. To quantitatively estimate the error between the experimental results and the simulation results, the RMSE of the experiment temperature related to the simulation temperature is calculated. Table 6.3 shows the Root-Mean Square Error (RMSE) for each case. All cases demonstrate that the simulated temperature profiles by the RNG k-ε turbulence model agree with the experimental data, and the realizable k-ε turbulence model generated lower temperature distribution than the experimental results.

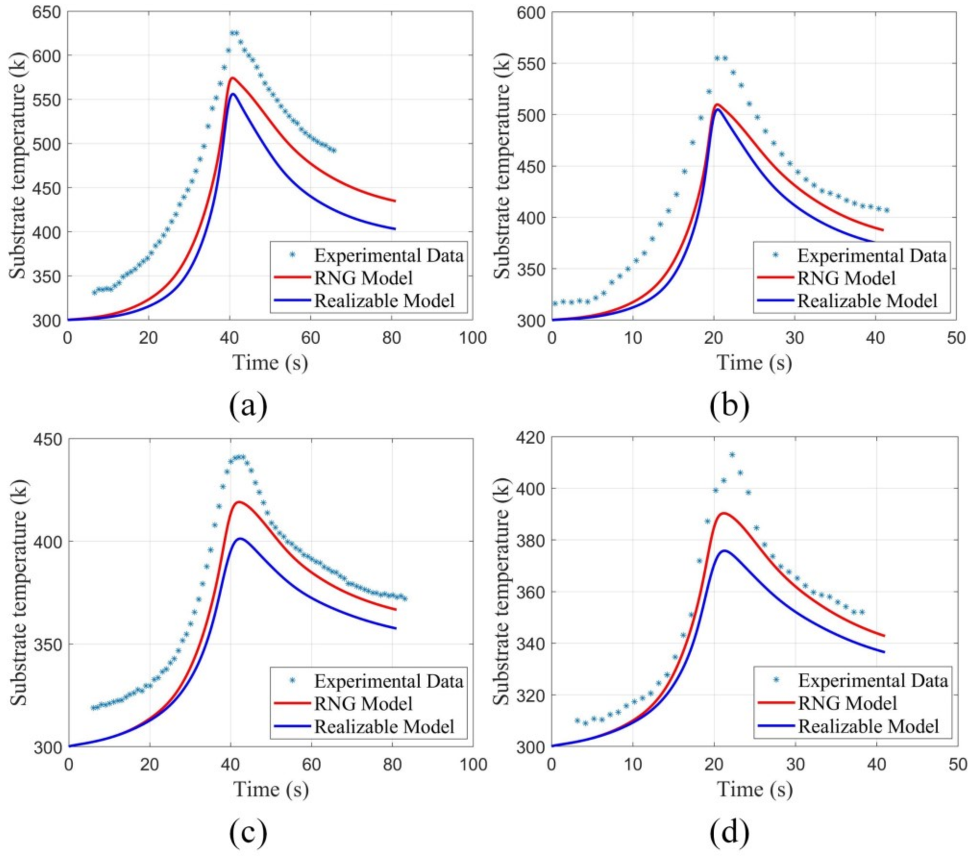

(a) (b) (c) (d)

Figure 6.15 The temperature of the center point versus time: (a) condition 1 with a 5 mm/s velocity, (b) condition 1 with a 10 mm/s velocity, (c) condition 2 with a 5 mm/s velocity, and (d) condition 2 with a 10 mm/s velocity.

Table 6.3 The RMSE of the experiment results related to the simulation results.

Cases	The RMSE related to the RNG model	The RMSE related to the realizable model
Condition 1 with a 5 mm/s velocity	50.7	72.3
Condition 1 with a 10 mm/s velocity	35.0	46.0
Condition 2 with a 5 mm/s velocity	15.7	24.2
Condition 2 with a 10 mm/s velocity	8.8	16.7

6.5 Conclusions

In this chapter, a feature-based digital HVOF model was constructed under the proposed template for acquiring the synchronized phenomena of the coated substrate temperature and coating thickness distribution, the nozzle trajectory. To demonstrate the data processing in the proposed framework, the data from the flame and the in-flight particle behavior, and the transient thermal performance of the coating layer and substrate was synchronously used. The final simulation result validates that the feature-based digital model is able to mirror the near-real-time scenarios with a light delay. It should be noted that the application of the feature-based digital model is not limited to understanding physics phenomena. With the further implementation of the proposed framework, real-time monitoring and control, prediction, and process optimization will be the outputs of the feature-based digital model. The operation data could be uploaded to a cloud platform via the proposed digital identifier for conducting the emerging technologies.

In addition, as a branch of this research work, to improve the prediction accuracy of the developed digital model, a coupling method has been developed based on the proposed user-defined boundary condition feature, which realizes an iterative link between the in-flight behavior model and dynamic coating model. For verifying this coupling method and testing the influence of two turbulence models, the RNG k-ε turbulence model and the realizable k-ε turbulence model, on the dynamic temperature simulation of the substrate, two operation conditions with two different scanning velocities were conducted in the simulation and experiment. Through the evaluation of the simulation results with experimental process measurements, it can be concluded that the RNG k-ε turbulence model works more accurately than the realizable k-ε turbulence model. The realizable k-ε turbulence model tends to generate a relatively lower temperature distribution.

The distinctions between this developed model and the traditional numerical model of the substrate temperature [87,108] are (1) the developed model aims to simulate the operational dynamics of the substrate temperature and the traditional models usually concentrate on the understanding of this physics phenomenon (they might be static simulations or the state at a moment); (2) the developed iterative coupling method increases the fidelity of the simulation, which is highly required by the DT concept.

Chapter 7: Conclusion, Discussion & Future Work

7.1 Conclusions

Our futuristic goal of the industrial process holds the promise of a state, in which real-time transmission and analysis of data from across processes, along with model-based simulation and optimization, create intelligence to yield positive impacts on all aspects of the industry. So far, some research works have contributed to this goal from different domains, like futuristic framework construction and emerging technology implementation. To date, the concerns about the DT modeling of physics phenomena in industrial processes, e.g., heat transfer, solidification, residual stress, and so on, are very limited. However, with more advanced manufacturing technologies applied to our industry, e.g., additive manufacturing and thermal spraying, this is critical to reaching the ideal state of the industry. Therefore, the research presented aims to develop a new framework that modularizes industrial processes in terms of the semantic information modules of physics in real-world phenomena and adopted CAE tools to construct achievable digital physics models of industrial processes. To achieve this goal, the following three modeling mechanisms are embedded into the framework: (1) multiple-view integration and closed-loop optimization, (2) inter-module associations, and (3) synchronization of physics phenomena.

To illustrate the above framework and the embedded modeling mechanisms, the high-velocity oxygen-fuel (HVOF) thermal spraying process is used as an example. Firstly, the physics behaviors in the spray nozzle, including the combustion in the spray nozzle, the flame, and the in-flight particle, are selected as the main concerns. For enhancing the flexibility of the model, the entities involved in the process are abstracted and modeled as different feature concepts. Through clarifying the associations among the features, a seamless information transfer is achieved. Built on these associations, a closed-loop process optimization method has been created, where the optimization intents can drive the numerical analysis for obtaining outputs specific for optimization. The effectiveness of the method is demonstrated by modeling a homemade HVOF spray system depositing WC-12Co coating. The coating properties are optimized by the developed model, which indicates that the model can provide effective solutions to the real-world system. Secondly, a parametrically controlled model for simulating the coating thickness in HVOF processes is developed by linking three individual models, the in-flight behavior model, a rule-based coating growth model, and nozzle trajectory. This integrated model considers the effect of the commonly used operating parameters, particle properties, and size range, and spray path on the coating thickness distribution, which shows excellent comprehensiveness. Meanwhile, the experiment results indicate that the modeling method can properly mirror the real scenario on the virtual side and predict the coating thickness with small errors. Thirdly, based on the real-world connections among different units, the user-defined boundary condition feature is further carried out for the synchronization of substrate temperature and coating thickness in HVOF processes. For realizing the synchronized phenomena, the data from the nozzle trajectory, the flame, and the in-flight particle behavior, and the transient thermal performance between the coating layer and substrate is synchronously used. The final simulation result validates that the feature-based digital model is able to mirror the near-real-time scenarios with a light delay.

7.2 Research Contributions

The main contributions of this research are summarized as follows:

- In the theoretical part, developed a conceptual framework that modularizes industrial processes in terms of the semantic information modules of physics in the real-world phenomena and adopted CAE tools to construct achievable digital physics models of industrial processes.
- Designed a workflow for the data acquisition, data analysis, data processing, and data validation in the proposed framework and mutual supports among different models in the CAE environment.
- Extended related feature definitions and developed a feature-based model template that can guide the modeling process to cater to the trend of digital twins in the industry by clarifying the model elements and organizing their functional relationships.
- Through applying partial feature concepts, developed a closed-loop and optimization-driven modeling method for improving HVOF coating properties under various scenarios.
- Proposed a novel approach to optimize the HVOF coating by controlling the in-flight behavior of the gas-particle jet.
- Developed a parametrically controlled HVOF coating thickness model. This model links the outputs from three individual modules, the in-flight behavior model, a rule-based coating growth model, and nozzle trajectory, so that the effect of the commonly used operating parameters, particle properties and size range, and spray path on the coating thickness distribution can be comprehensively studied.
- Developed a hierarchical key characteristic flow of HVOF processes which assists to build the inter-model links for comprehensively describe HVOF processes.
- Implemented the user-defined boundary condition feature for constructing the association of the data from the flame and the in-flight particle behavior, and the transient thermal performance between the coating layer and substrate via the nozzle trajectory.

- Realized a feature-based digital model which enables to mirror the near-real-time simulation of the substrate temperature and coating thickness with a light delay.

7.3 Limitations and Future Work

Despite the achievements, the research presented is confronted by particular limitations and can be addressed in future work:

- The proposed framework is only demonstrated by a specific industrial process, the HVOF process. Other industrial processes which have complex physicochemical phenomena need to be studied in the future to improve the generalization of the framework.
- The implementation of the framework only concentrates on partial functions concerned by digital twins, e.g., the ability to generate positive impacts on the real world, comprehensiveness of the virtual world for representing the real world, synchronization of physics phenomena. However, other functions mentioned in the framework, e.g., big-data driven optimization and real-time interaction, are not covered in this research. In the future, by running with a collaborative environment, the same data format from the same template could be easily navigated. The global information collection will support a big-data driven optimization for industrial processes. In the aspect of the real-time interaction, with the assistance of the physical properties in the future, such as a control system, the outputs from the model could be translated to execution signals which command the actuators to carry out them on the real side.
- Regarding the specific modeling process for the HVOF coating optimization, to better control the HVOF in-flight particle properties, the optimization process can be further enhanced by incorporating more objectives and specific constraints in the conceptual model (Figure 4.1),

for example, reducing spray distance can be added to optimization constraints for obtaining a concentrated deposition profile synchronously. The optimization will be extended to spray path planning so that more process parameters can be considered and optimized.

- The developed coating thickness model is still in its infancy. The modeling of the splats' morphology and coating growth is not sophisticated. In the future, it can be captured by applying a more advanced numerical model that encapsulates the more physics features of the coating formation, such as the deformation of the previously deposited coating due to the impinging of the flame and particles. In addition, the substrate surface in the HVOF in-flight behavior model will be changed to different geometries for exploring the coating distribution on different substrate shapes. A 3D CFD model for the in-flight behavior simulation can be developed so that the spray angle of the nozzle relative to the substrate surface can be adjusted.

Bibliography

[1] Tao F, Qi Q, Wang L, Nee AYC. Digital Twins and Cyber – Physical Systems toward Smart Manufacturing and Industry 4 . 0 : Correlation and Comparison. Engineering 2019;5:653–61. doi:10.1016/j.eng.2019.01.014.

[2] Tao F, Zhang H, Liu A, Nee AYC. Digital Twin in Industry: State-of-the-Art. IEEE Trans Ind Informatics 2019;15:2405–15. doi:10.1109/TII.2018.2873186.

[3] Lu Y, Liu C, Wang KIK, Huang H, Xu X. Digital Twin-driven smart manufacturing: Connotation, reference model, applications and research issues. Robot Comput Integr Manuf 2020;61:101837. doi:10.1016/j.rcim.2019.101837.

[4] Autiosalo J, Vepsalainen J, Viitala R, Tammi K. A Feature-Based Framework for Structuring Industrial Digital Twins. IEEE Access 2020;8:1193–208. doi:10.1109/ACCESS.2019.2950507.

[5] Pierlot C, Pawlowski L, Bigan M, Chagnon P. Design of experiments in thermal spraying: A review. Surf Coatings Technol 2008;202:4483–90. doi:10.1016/j.surfcoat.2008.04.031.

[6] Pan J, Hu S, Yang L, Ding K, Ma B. Numerical analysis of flame and particle behavior in an HVOF thermal spray process. Mater Des 2016;96:370–6. doi:10.1016/j.matdes.2016.02.008.

[7] Nahvi SM, Jafari M. Microstructural and mechanical properties of advanced HVOF-sprayed WC-based cermet coatings. Surf Coat Technol 2016;286:95–102. doi:10.1016/j.surfcoat.2015.12.016.

[8] Li L, Zheng Y, Yang M, Leng J, Cheng Z, Xie Y. A survey of feature modeling methods : Historical evolution and new development. Robot Comput Integr Manuf 2020;61:101851. doi:10.1016/j.rcim.2019.101851.

[9] Gujarathi GP, Ma YS. Parametric CAD/CAE integration using a common data model. J Manuf Syst 2011;30:118–32. doi:10.1016/j.jmsy.2011.01.002.

[10] Montgomery DC. Design and Analysis of Experiments. Eighth Edi. Hoboken: John Wiley & Sons,

Inc.; 2012.

[11] Bahman AS, Iannuzzo F. Computer-aided engineering simulations. 1st ed. Duxford: Elsevier Ltd.; 2018. doi:10.1016/B978-0-08-102094-4.00010-4.

[12] Bi Z. Overview of Finite Element Analysis. 1st ed. London: Katey Birtcher; 2018. doi:10.1016/b978-0-12-809952-0.00001-7.

[13] Li L, Lange CF, Xu Z, Jiang P, Ma Y. Feature-based intelligent system for steam simulation using computational fluid dynamics. Adv Eng Informatics 2018;38:357–69. doi:10.1016/j.aei.2018.08.011.

[14] Skrinjar L, Slavič J, Boltežar M. A review of continuous contact-force models in multibody dynamics. Int J Mech Sci 2018;145:171–87. doi:10.1016/j.ijmecsci.2018.07.010.

[15] Beiranvand V, Hare W, Lucet Y. Best practices for comparing optimization algorithms. Optim Eng 2017;18:815–48. doi:10.1007/s11081-017-9366-1.

[16] Rosen R, Von Wichert G, Lo G, Bettenhausen KD. About the importance of autonomy and digital twins for the future of manufacturing. IFAC-PapersOnLine 2015;28:567–72. doi:10.1016/j.ifacol.2015.06.141.

[17] Michael Grieves. Digital Twin: Manufacturing Excellence through Virtual Factory Replication 2015. https://www.researchgate.net/publication/275211047_Digital_Twin_Manufacturing_Excellence_through_Virtual_Factory_Replication.

[18] Tuegel EJ, Ingraffea AR, Eason TG, Spottswood SM. Reengineering aircraft structural life prediction using a digital twin. Int J Aerosp Eng 2011;2011. doi:10.1155/2011/154798.

[19] Tao F, Zhang M. Digital Twin Shop-Floor: A New Shop-Floor Paradigm Towards Smart Manufacturing. IEEE Access 2017;5:20418–27. doi:10.1109/ACCESS.2017.2756069.

[20] E. H. Glaessgen. The Digital Twin Paradigm for Future NASA and U.S. Air Force Vehicles. 3rd

AIAA/ASME/ASCE/AHS/ASC Struct. Struct. Dyn. Mater. Conf. - Spec. Sess. Digit. Twin, 2012.

[21] Eric J. Tuegel. The Airframe Digital Twin: Some Challenges to Realization. 53rd AIAA/ASME/ASCE/AHS/ASC Struct. Struct. Dyn. Mater. Conf., Honolulu, Hawaii: n.d.

[22] Schluse M, Rossmann J, Development S. From Simulation to Experimentable Digital Twins. IEEE Int Symp Syst Eng 2016:1–6.

[23] Schluse M, Priggemeyer M, Atorf L, Rossmann J. Experimentable Digital Twins—Streamlining Simulation-Based Systems Engineering for Industry 4.0. IEEE Trans Ind Informatics 2018;14:1722–31. doi:10.1109/TII.2018.2804917.

[24] Tao F, Zhang M, Liu Y, Nee AYC. Digital twin driven prognostics and health management for complex equipment. CIRP Ann 2018;67:169–72. doi:10.1016/j.cirp.2018.04.055.

[25] Gabor T, Belzner L, Kiermeier M, Beck MT, Neitz A. A simulation-based architecture for smart cyber-physical systems. Proc - 2016 IEEE Int Conf Auton Comput ICAC 2016 2016:374–9. doi:10.1109/ICAC.2016.29.

[26] Tao F, Sui F, Liu A, Qi Q, Zhang M, Song B, et al. Digital twin-driven product design framework. Int J Prod Res 2019;7543:1–19. doi:10.1080/00207543.2018.1443229.

[27] Tao F, Cheng J, Qi Q, Zhang M, Zhang H, Sui F. Digital twin-driven product design , manufacturing and service with big data 2018:3563–76. doi:10.1007/s00170-017-0233-1.

[28] Schroeder G, Steinmetz C, Pereira CE, Muller I, Garcia N, Espindola D, et al. Visualising the Digital Twin using Web Services and Augmented Reality. 2016 IEEE 14th Int. Conf. Ind. Informatics, Poitiers, France: IEEE; 2016, p. 522–7. doi:10.1109/INDIN35080.2016.

[29] Erkoyuncu JA, del Amo IF, Ariansyah D, Bulka D, Vrabič R, Roy R. A design framework for adaptive digital twins. CIRP Ann 2020;69:145–8. doi:10.1016/j.cirp.2020.04.086.

[30] Schroeder GN, Steinmetz C, Pereira CE, Espindola DB. Digital Twin Data Modeling with

AutomationML and a Communication Methodology for Data Exchange. IFAC-PapersOnLine 2016;49:12–7. doi:10.1016/j.ifacol.2016.11.115.

[31] Moreno A, Velez G, Ardanza A, Barandiaran I, Ruíz Á, Raúl DI. Virtualisation process of a sheet metal punching machine within the Industry 4 . 0 vision. Int J Interact Des Manuf 2017;11:365–73. doi:10.1007/s12008-016-0319-2.

[32] Iglesias D, Bunting P, Esquembri S, Hollocombe J, Silburn S, Vitton-Mea L, et al. Digital twin applications for the JET divertor. Fusion Eng Des 2017;125:71–6. doi:10.1016/j.fusengdes.2017.10.012.

[33] Söderberg R, Wärmefjord K, Madrid J, Lorin S, Forslund A, Lindkvist L. An information and simulation framework for increased quality in welded components. CIRP Ann 2018;67:165–8. doi:10.1016/j.cirp.2018.04.118.

[34] DebRoy T, Zhang W, Turner J, Babu SS. Building digital twins of 3D printing machines. Scr Mater 2017;135:119–24. doi:10.1016/j.scriptamat.2016.12.005.

[35] Zheng Y, Yang S, Cheng H. An application framework of digital twin and its case study. J Ambient Intell Humaniz Comput 2019;10:1141–53. doi:10.1007/s12652-018-0911-3.

[36] Tao F, Qi Q, Wang L, Nee AYC. Digital Twins and Cyber–Physical Systems toward Smart Manufacturing and Industry 4.0: Correlation and Comparison. Engineering 2019;5:653–61. doi:10.1016/j.eng.2019.01.014.

[37] Madni AM, Madni CC, Lucero SD. Leveraging Digital Twin Technology in Model-Based Systems Engineering. Systems 2021;7:1–13. doi:10.3390/systems7010007.

[38] Sanfilippo EM, Borgo S. What are features ? An ontology-based review of the literature. Comput Des 2016;80:9–18. doi:10.1016/j.cad.2016.07.001.

[39] Poldermann B. Surface Design Based on Parametrized Surface Features. Proc Int Symp Tools

Methods Concurr Eng 1995.

[40] Belaziz M, Bouras a., Brun JM. Morphological analysis for product design. Comput Des 2000;32:377–88. doi:10.1016/S0010-4485(00)00019-1.

[41] GINDY NNZ. A hierarchical structure for form features. Int J Prod Res 1989;27:2089–103. doi:10.1080/00207548908942677.

[42] Erden MS, Komoto H, Van Beek TJ, D'Amelio V, Echavarria E, Tomiyama T. A review of function modeling: Approaches and applications. Artif Intell Eng Des Anal Manuf AIEDAM 2008;22:147–69. doi:10.1017/S0890060408000103.

[43] Schulte M, Weber C, Stark R. Functional features for design in mechanical engineering. Comput Ind 1993;23:15–24. doi:10.1016/0166-3615(93)90111-D.

[44] Brown DC. Functional, Behavioral and Structural Features. Proc DETC'03 ASME 2003 Des Eng Tech Conf Comput Inf Eng Conf 2003:1–6.

[45] Park H, Dang X. Structural optimization based on CAD – CAE integration and metamodeling techniques. Comput Des 2010;42:889–902. doi:10.1016/j.cad.2010.06.003.

[46] Lee SH. A CAD-CAE integration approach using feature-based multi-resolution and multi-abstraction modelling techniques. CAD Comput Aided Des 2005;37:941–55. doi:10.1016/j.cad.2004.09.021.

[47] Yeol Lee J, Kim K. A feature-based approach to extracting machining features. Comput Des 1998;30:1019–35. doi:10.1016/S0010-4485(98)00055-4.

[48] Yan X, Yamazaki K, Liu J. Recognition of machining features and feature topologies from NC programs. CAD Comput Aided Des 2000;32:605–16. doi:10.1016/S0010-4485(00)00045-2.

[49] Wang L, Cai N, Feng HY, Liu Z. Enriched machining feature-based reasoning for generic machining process sequencing. Int J Prod Res 2006;44:1479–501. doi:10.1080/00207540500354119.

[50] Liu J, To AC. Topology optimization for hybrid additive-subtractive manufacturing. Struct Multidiscip Optim 2017;55:1281–99. doi:10.1007/s00158-016-1565-4.

[51] Van Holland W, Bronsvoort WF. Assembly features in modeling and planning. Robot Comput Integr Manuf 2000;16:277–94. doi:10.1016/S0736-5845(00)00014-4.

[52] Deneux D. Introduction to assembly features: An illustrated synthesis methodology. J Intell Manuf 1999;10:29–39. doi:10.1023/A:1008912429442.

[53] Ma YS, Britton GA, Tor SB, Jin LY. Associative assembly design features: Concept, implementation and application. Int J Adv Manuf Technol 2007;32:434–44. doi:10.1007/s00170-005-0371-8.

[54] IEEE Standard Glossary of Software Engineering Terminology. IEEE Std 61012-1990 1990:1–84. doi:10.1109/IEEESTD.1990.101064.

[55] Ma YS, Chen G, Thimm G. Paradigm shift: Unified and associative feature-based concurrent and collaborative engineering. J Intell Manuf 2008;19:625–41. doi:10.1007/s10845-008-0128-y.

[56] JJ Cunningham JD. Designing with features: the origin of features. ASME Comput. Eng. Conf. Exhib., New York: ASME; 1988, p. 237–43.

[57] Anderson DC, Chang TC. Geometric reasoning in feature-based design and process planning. Comput Graph 1990;14:225–35. doi:10.1016/0097-8493(90)90034-U.

[58] Sypkens Smit M, Bronsvoort WF. Integration of design and analysis models. Comput Aided Des Appl 2009;6:795–808. doi:10.3722/cadaps.2009.795-808.

[59] Bronsvoort WF, Noort A. Multiple-view feature modelling for integral product development. CAD Comput Aided Des 2004;36:929–46. doi:10.1016/j.cad.2003.09.008.

[60] Cheng Z, Ma Y. A functional feature modeling method. Adv Eng Informatics 2017;33:1–15. doi:10.1016/j.aei.2017.04.003.

[61] Cheng Z, Ma Y. Explicit function-based design modelling methodology with features. J Eng Des 2017;28:205–31. doi:10.1080/09544828.2017.1291920.

[62] Li L, Ma Y. CAD/CAE associative features for cyclic fluid control effect modeling. Comput Aided Des Appl 2016;13:208–20. doi:10.1080/16864360.2015.1084190.

[63] Brunetti G, Golob B. A feature-based approach towards an integrated product model including conceptual design information. Comput Des 2000;32:877–87. doi:10.1016/S0010-4485(00)00076-2.

[64] Li L, Lange CF, Ma Y. Association of design and computational fluid dynamics simulation intent in flow control product optimization. Proc Inst Mech Eng Part B J Eng Manuf 2017:095440541769735. doi:10.1177/0954405417697352.

[65] Xie Y, Ma Y. Design of a multi-disciplinary and feature-based collaborative environment for chemical process projects. Expert Syst Appl 2015;42:4149–66. doi:10.1016/j.eswa.2015.01.009.

[66] Oberkampf WL, Talpallikar M. (HVOF) Thermal Spray Torch Part 1 : Numerical Formulation. J Therm Spray Technol 1996;5:53–61. doi:10.1007/BF02647519.

[67] Thiruvikraman C, Balasubramanian V, Sridhar K. Optimizing HVOF Spray Parameters to Maximize Bonding Strength of WC-CrC-Ni Coatings on AISI 304L Stainless Steel. J Therm Spray Technol 2014;23:860–75. doi:10.1007/s11666-014-0091-4.

[68] Li M, Christofides PD. Modeling and Control of High-Velocity Oxygen-Fuel (HVOF) Thermal Spray: A Tutorial Review. J Therm Spray Technol 2009;18:753–68. doi:10.1007/s11666-009-9309-2.

[69] Vignesh S, Shanmugam K, Balasubramanian V, Sridhar K. Identifying the optimal HVOF spray parameters to attain minimum porosity and maximum hardness in iron based amorphous metallic coatings. Def Technol 2017;13:101–10. doi:10.1016/j.dt.2017.03.001.

[70] Congress G, Gcmm- M. Optimization Parameters of WC-12Co HVOF Sprayed Coatings on Optimization Parameters of WC-12Co HVOF Sprayed Coatings on 400 Stainless. Procedia Manuf 2019;30:506–13. doi:10.1016/j.promfg.2019.02.071.

[71] Susila A, Sarangan J, Suresh S, Channabasappa BH. Optimization and erosion wear response of NiCrSiB / WC – Co HVOF coating using Taguchi method. Ceram Int 2016;42:1094–104. doi:10.1016/j.ceramint.2015.09.036.

[72] Li M, Christofides PD. Multi-scale modeling and analysis of an industrial HVOF thermal spray process. Chem Eng Sci 2005;60:3649–69. doi:10.1016/j.ces.2005.02.043.

[73] Baik JS, Kim YJ. Effect of nozzle shape on the performance of high velocity oxygen-fuel thermal spray system. Surf Coatings Technol 2008;202:5457–62. doi:10.1016/j.surfcoat.2008.06.061.

[74] Kamnis S, Gu S. 3-D modelling of kerosene-fuelled HVOF thermal spray gun. Chem Eng Sci 2006;61:5427–39. doi:10.1016/j.ces.2006.04.005.

[75] Khan MN, Shamim T. Investigation of a dual-stage high velocity oxygen fuel thermal spray system. Appl Energy 2014;130:853–62. doi:10.1016/j.apenergy.2014.03.075.

[76] Emami S, Jafari H, Mahmoudi Y. Effects of Combustion Model and Chemical Kinetics in Numerical Modeling of Hydrogen-Fueled Dual-Stage HVOF System. J Therm Spray Technol 2019;28:333–45. doi:10.1007/s11666-019-00826-8.

[77] Jadidi M, Moghtadernejad S, Dolatabadi A. Numerical Modeling of Suspension HVOF. J Therm Spray Technol 2016;25:451–64. doi:10.1007/s11666-015-0364-6.

[78] Chadha S, Hussain T. Effect of nozzle geometry on the gas dynamics and evaporation rates of Suspension High Velocity Oxy Fuel (SHVOF) thermal spray : A numerical investigation. Surf Coat Technol 2019;371:78–89. doi:10.1016/j.surfcoat.2018.10.085.

[79] Jadidi M, Moghtadernejad S, Dolatabadi A. A Comprehensive Review on Fluid Dynamics and

Transport of Suspension/Liquid Droplets and Particles in High-Velocity Oxygen-Fuel (HVOF) Thermal Spray. Coatings 2015;5:576–645. doi:10.3390/coatings5040576.

[80] Li M, Christofides PD. Modeling and Control of High-Velocity Oxygen-Fuel (HVOF) Thermal Spray: A Tutorial Review. J Therm Spray Technol 2009;18:753–68. doi:10.1007/s11666-009-9309-2.

[81] Li M, Christofides PD. Computational study of particle in-flight behavior in the HVOF thermal spray process. Chem Eng Sci 2006;61:6540–52. doi:10.1016/j.ces.2006.05.050.

[82] Cetegen BM, Basu S. Review of Modeling of Liquid Precursor Droplets and Particles Injected into Plasmas and High-Velocity Oxy-Fuel (HVOF) Flame Jets for Thermal Spray Deposition Applications. J Therm Spray Technol 2009;18:769–93. doi:10.1007/s11666-009-9365-7.

[83] Li M, Shi D, Christofides PD. Diamond Jet Hybrid HVOF Thermal Spray: Gas-Phase and Particle Behavior Modeling and Feedback Control Design. Ind Eng Chem Res 2004;43:3632–52. doi:10.1021/ie030559i.

[84] Heberlein JVR. Thermal Spray Fundamentals. 1st ed. London: Springer; 2014.

[85] Yang X, Eidelman S. Numerical Analysis of a High-Velocity Oxygen-Fuel Thermal Spray System. J Therm Spray Technol 1996;5:175–84.

[86] Li M, Shi D, Christofides PD. Diamond Jet hybrid HVOF thermal spray: Gas-phase and particle behavior modeling and feedback control design. Ind Eng Chem Res 2004;43:3632–52. doi:10.1021/ie030559i.

[87] Bolot R, Deng S, Cai Z, Liao H, Montavon G. A Coupled Model Between Robot Trajectories and Thermal History of the Workpiece During Thermal Spray Operation. J Therm Spray Technol 2014;23:296–303. doi:10.1007/s11666-013-0048-z.

[88] Candel A, Gadow R. Trajectory Generation and Coupled Numerical Simulation for Thermal

Spraying Applications on Complex Geometries. J Therm Spray Technol 2009;18:981–7. doi:10.1007/s11666-009-9338-x.

[89] Gadow R, Candel A, Floristán M. Optimized robot trajectory generation for thermal spraying operations and high quality coatings on free-form surfaces. Surf Coatings Technol 2010;205:1074–9. doi:10.1016/j.surfcoat.2010.08.121.

[90] Hegels D, Wiederkehr T, Müller H. Simulation based iterative post-optimization of paths of robot guided thermal spraying. Robot Comput Integr Manuf 2015;35:1–15. doi:10.1016/j.rcim.2015.02.002.

[91] Chen C, Xie Y, Verdy C, Liao H, Deng S. Modelling of coating thickness distribution and its application in offline programming software. Surf Coatings Technol 2017;318:315–25. doi:10.1016/j.surfcoat.2016.10.044.

[92] Zhang Y, Li W, Zhang C, Liao H, Zhang Y, Deng S. A spherical surface coating thickness model for a robotized thermal spray system. Robot Comput Integr Manuf 2019;59:297–304. doi:10.1016/j.rcim.2019.05.003.

[93] Wu H, Xie X, Liu M, Chen C, Liao H, Zhang Y, et al. A new approach to simulate coating thickness in cold spray. Surf Coatings Technol 2020;382:125151. doi:10.1016/j.surfcoat.2019.125151.

[94] Shi D, Li M, Christofides PD. Diamond Jet Hybrid HVOF Thermal Spray: Rule-Based Modeling of Coating Microstructure. Ind Eng Chem Res 2004;43:3653–65. doi:10.1021/ie030560h.

[95] Mostaghimi J, Chandra S, Ghafouri-Azar R, Dolatabadi A. Modeling thermal spray coating processes: A powerful tool in design and optimization. Surf Coatings Technol 2003;163–164:1–11. doi:10.1016/S0257-8972(02)00686-2.

[96] Nylén P, Edberg M. Robot trajectory generation and coating temperature prediction of plasma sprayed coatings. Materials Park, OH: ASM; 1997.

[97] Liu J, Bolot R, Costil S. Residual stresses and final deformation of an alumina coating: Modeling and measurement. Surf Coatings Technol 2015;268:241–6. doi:10.1016/j.surfcoat.2014.05.050.

[98] Abbasi R, Yanes AR, Villanuera EM, Ahmad R. Real-time Implementation of Digital Twin for Robot Based Production Line. SSRN Electron J 2021:4–6. doi:10.2139/ssrn.3860500.

[99] Sharif Ullah AMM. Modeling and simulation of complex manufacturing phenomena using sensor signals from the perspective of Industry 4.0. Adv Eng Informatics 2019;39:1–13. doi:10.1016/j.aei.2018.11.003.

[100] Grieves M, Vickers J. Digital Twin : Mitigating Unpredictable , Undesirable Emergent Behavior in Complex Systems 2017. doi:10.1007/978-3-319-38756-7.

[101] Lu Y, Xu X. Cloud-based manufacturing equipment and big data analytics to enable on-demand manufacturing services. Robot Comput Integr Manuf 2019;57:92–102. doi:10.1016/j.rcim.2018.11.006.

[102] Bolleddu V, Racherla V, Bandyopadhyay PP. Comparative study of air plasma sprayed and high velocity oxy-fuel sprayed nanostructured WC-17wt%Co coatings. Int J Adv Manuf Technol 2016;84:1601–13. doi:10.1007/s00170-015-7824-5.

[103] Lian FL, Moyne JR, Tilbury DM. Performance evaluation of control networks: Ethernet, ControlNet, and DeviceNet. IEEE Control Syst 2001;21:66–83. doi:10.1109/37.898793.

[104] Li L, Cheng Z, Lange CF. CFD-Based Optimization of Fluid Flow Product Aided by Artificial Intelligence and Design Space Validation. Math Probl Eng 2018;2018:1–14. doi:10.1155/2018/8465020.

[105] Almeida M, Erthal R, Padua E, Silveira L, Am L. Talanta Response surface methodology (RSM) as a tool for optimization in analytical chemistry 2008;76:965–77. doi:10.1016/j.talanta.2008.05.019.

[106] Chen G, Ma YS, Thimm G, Tang SH. Unified Feature Modeling Scheme for the Integration of CAD and CAx. Comput Aided Des Appl 2004;1:595–601. doi:10.1080/16864360.2004.10738303.

[107] Mostaghimi J, Chandra S, Dolatabadi A. Modeling thermal spray coating processes : a powerful tool in design and optimization. Surf Coat Technol 2003;164:1–11.

[108] Toparli M, Sen F, Culha O, Celik E. Thermal stress analysis of HVOF sprayed WC-Co/NiAl multilayer coatings on stainless steel substrate using finite element methods. J Mater Process Technol 2007;190:26–32. doi:10.1016/j.jmatprotec.2007.03.115.

[109] Ng HW, Gan Z. A finite element analysis technique for predicting as-sprayed residual stresses generated by the plasma spray coating process 2005;41:1235–54. doi:10.1016/j.finel.2005.02.002.

[110] Thorpe ML, Richter HJ. A Pragmatic Analysis and Comparison of HVOF Processes. J Therm Spray Technol 1992;1:169–78.

[111] Gadow R, Floristán M. Manufacturing engineering in thermal spraying by advanced robot systems and process kinematics. Futur. Dev. Therm. Spray Coatings, Elsevier; 2015, p. 259–80. doi:10.1016/B978-0-85709-769-9.00011-7.

[112] Cheng D, Xu Q, Trapaga G, Lavernia EJ, Introduction I. A Numerical Study of High-Velocity Oxygen Fuel Thermal Spraying Process. Part I : Gas Phase Dynamics. Metall Mater Trans A 2001;32A.

[113] Gordon S, McBride B. Computer Program for Calculation of Complex Chemical Equilibrium Compositions, Rocket Performance, Incident and Reflected Shocks and Chapman–Jouguet Detonations. Washington, D.C.: NASA Reference Publication; 1971.

[114] Huang F, Wang D, Li Z, Gao Z, Derksen JJ. Mixing process of two miscible fl uids in a lid-driven cavity. Chem Eng J 2019;362:229–42. doi:10.1016/j.cej.2019.01.024.

[115] Li L, Lange CF, Ma Y, Lange CF. Artificial intelligence aided CFD analysis regime validation and

selection in feature-based cyclic CAD / CFD interaction process. Comput Des &Applications 2018;15:1–10. doi:10.1080/16864360.2018.1441230.

[116] Rößger P, Richter A. Performance of different optimization concepts for reactive flow systems based on combined CFD and response surface methods. Comput Chem Eng 2018;108:232–9. doi:10.1016/j.compchemeng.2017.09.008.

[117] Song H, Dan J, Li J, Du J, Xiao J, Xu J. Experimental study on the cutting force during laser-assisted machining of fused silica based on the Taguchi method and response surface methodology. J Manuf Process 2019;38:9–20. doi:10.1016/j.jmapro.2018.12.038.

[118] Sobolev VV, Guilemany JM, Gramier JC, Calero JA. Modelling of particle movement and thermal behaviour during high velocity oxy-fuel spraying. Surf Coat Technol 1994;63:181–7.

[119] Kuhn M. Desirabiliy Function Optimization and Ranking n.d.

[120] Nelder JA, Mead R. A Simplex Method for Function Minimization. Comput J 1965;7:308–13. doi:10.1093/comjnl/7.4.308.

[121] Andulkar M V, Chiddarwar SS, Marathe AS, Cam CAD. Novel integrated offline trajectory generation approach for robot assisted spray painting operation. J Manuf Syst 2015;37:201–16. doi:10.1016/j.jmsy.2015.03.006.

[122] Cai Z, Deng S, Liao H, Zeng C, Montavon G. The Effect of Spray Distance and Scanning Step on the Coating Thickness Uniformity in Cold Spray Process. J Therm Spray Technol 2013;23:1–10. doi:10.1007/s11666-013-0002-0.

[123] Khan MN, Shah S, Shamim T. Investigation of operating parameters on high-velocity oxyfuel thermal spray coating quality for aerospace applications. Int J Adv Manuf Technol 2019;103:2677–90. doi:10.1007/s00170-019-03696-0.

[124] Fluent Inc (Theory 2001). Discrete Phase Modelling. ANSYS FLUENT User's Guid 2016:1–170.

[125] Bartuli C, Valente T, Cipri F, Bemporad E, Tului M. Parametric Study of an HVOF Process for the Deposition of Nanostructured WC-Co Coatings. J Therm Spray Technol 2005;14:187–95. doi:10.1361/10599630523746.

[126] Zhao L, Maurer M, Fischer F, Lugscheider E. Study of HVOF spraying of WC-CoCr using on-line particle monitoring. Surf Coatings Technol 2004;185:160–5. doi:10.1016/j.surfcoat.2003.12.024.

[127] William C. Hinds. Aerosol Technology: Properties, Behavior, and Measurement of Airborne Particles. 2nd ed. New York: Wiley; 1999.

[128] Ding X, Cheng X, Shi J, Li C, Yuan C, Ding Z-X. Influence of WC size and HVOF process on erosion wear performance of WC-10Co4Cr coatings. Int J Adv Manuf Technol 2018;96:1615–24. doi:10.1007/s00170-017-0795-y.

[129] Ren J, Zhang G, Rong Y, Ma Y. A feature-based model for optimizing HVOF process by combining numerical simulation with experimental verification. J Manuf Process 2021;64:224–38. doi:10.1016/j.jmapro.2021.01.017.

[130] Yang K, Liu M, Zhou K, Deng C. Recent Developments in the Research of Splat Formation Process in Thermal Spraying 2013;2013.

[131] Madejski J. Solidification of droplets on a cold surface. Int J Heat Mass Transf 1976;19:1009–13. doi:10.1016/0017-9310(76)90183-6.

[132] Zhao P, Hargrave GK, Versteeg HK, Garner CP, Reid BA, Long EJ, et al. The dynamics of droplet impact on a heated porous surface. Chem Eng Sci 2018;190:232–47. doi:10.1016/j.ces.2018.06.030.

[133] Tabbara H, Gu S. Numerical study of semi-molten droplet impingement. Appl Phys A 2011;104:1011–9. doi:10.1007/s00339-011-6510-1.

[134] Ren J, Rong Y, Ma Y. Comparison of the Renormalization Group and the Realizable k-ε Turbulence Models for Dynamic Performance of HVOF Process with a Coupled Two-Stage CAE Method.

Comput Aided Des Appl 2020;18:117–29. doi:10.14733/cadaps.2021.117-129.

[135] Fauchais P. Current status and future directions of thermal spray coatings and techniques. Elsevier Ltd.; 2015. doi:10.1016/B978-0-85709-769-9.00002-6.

[136] Tabbara H, Gu S. Computational simulation of liquid-fuelled HVOF thermal spraying. Surf Coat Technol 2009;204:676–84. doi:10.1016/j.surfcoat.2009.09.005.

[137] Deng S, Liang H, Cai Z, Liao H, Montavon G. Kinematic Optimization of Robot Trajectories for Thermal Spray Coating Application. J Therm Spray Technol 2014;23:1382–9. doi:10.1007/s11666-014-0137-7.

[138] Cai Z, Liang H, Quan S, Deng S, Zeng C, Zhang F. Computer-Aided Robot Trajectory Auto-generation Strategy in Thermal Spraying. J Therm Spray Technol 2015;24:1235–45. doi:10.1007/s11666-015-0282-7.

[139] Ren J, Ma Y. A Feature-based Physical-Geometric Model for Dynamic Effect in HVOF Thermal Spray Process. Comput Aided Des Appl 2019;17:561–74. doi:10.14733/cadaps.2020.561-574.

[140] Cao Y, Zhu S, Liang X, Wang W. Overlapping model of beads and curve fitting of bead section for rapid manufacturing by robotic MAG welding process. Robot Comput Integr Manuf 2011;27:641–5. doi:10.1016/j.rcim.2010.11.002.

[141] Inc. ANSYS. ANSYS FLUENT Theory Guide. Release 182 2017;15317:724–46. doi:10.1016/0140-3664(87)90311-2.

[142] Jabbari F, Jadidi M, Wuthrich R, Dolatabadi A. A Numerical Study of Suspension Injection in Plasma-Spraying Process. J Therm Spray Technol 2014;23:3–13. doi:10.1007/s11666-013-0030-9.

[143] Cai Z, Qi B, Tao C, Luo J, Chen Y, Xie C. A Robot Trajectory Optimization Approach for Thermal Barrier Coatings Used for Free-Form Components. J Therm Spray Technol 2017;26:1651–8. doi:10.1007/s11666-017-0601-2.

[144] Baik J-S, Park S-K, Kim Y-J. A Numerical Study on Gas Phase Dynamics of High-Velocity Oxygen Fuel Thermal Spray. Jpn J Appl Phys 2008;47:6907–9. doi:10.1143/JJAP.47.6907.

Appendix 1 Mathematical Representation of the HVOF Numerical Model

The flame flow in the HVOF process is a high-Reynolds-number turbulent compressible flow. The flame flow is solved by Reynolds-averaged ($\bar{\phi} = (1/\Delta t)\int_{t_1}^{t_0+\Delta t} \phi \mathrm{d}t$) and Favre-averaged ($\tilde{\phi} = \overline{\rho\phi}/\bar{\rho}$) governing equations as follows [72]:

$$\frac{\partial \bar{\rho}}{\partial t} + \frac{\partial}{\partial x_j}(\bar{\rho}\tilde{v}_j) = 0, \tag{A.1}$$

$$\frac{\partial}{\partial t}(\bar{\rho}\tilde{v}_i) + \frac{\partial}{\partial x_j}(\bar{\rho}\tilde{v}_i\tilde{v}_j) = -\frac{\partial \bar{p}}{\partial x_i} + \frac{\partial}{\partial x_j}\left[\mu\left(\frac{\partial \tilde{v}_i}{\partial x_j} + \frac{\partial \tilde{v}_j}{\partial x_i} - \frac{2}{3}\delta_{ij}\frac{\partial \tilde{v}_l}{\partial x_l}\right)\right] + \frac{\partial}{\partial x_j}(-\overline{\rho v_i'' v_j''}), i = 1, 2, 3, \tag{A.2}$$

where ρ is the density, p is the pressure, x is the coordinate, μ is the molecular viscosity, and δ_{ij} is the Kronecker delta. According to the Boussinesq hypothesis, the Reynolds stress term representing the effect of turbulence can be related to the mean velocity gradients:

$$-\overline{\rho v_i'' v_j''} = \mu_t\left(\frac{\partial \tilde{v}_i}{\partial x_j} + \frac{\partial \tilde{v}_j}{\partial x_i}\right) - \frac{2}{3}\left(\bar{\rho}k + \mu_t\frac{\partial \tilde{v}_l}{\partial x_l}\right)\delta_{ij}, \tag{A.3}$$

where μ_t is the turbulent viscosity and k is the turbulence kinetic energy, because of the supersonic flow and the large pressure gradients in the nozzle.

Here, the renormalization group turbulence model is used as the representative. The renormalization group (RNG) k-ε turbulence model is used to estimate the turbulent eddy viscosity with the non-equilibrium wall function treatment used to enhance the wall shear and heat transfer [72,112,144]:

$$\frac{\partial}{\partial t}(\bar{\rho}k) + \frac{\partial}{\partial x_i}(\bar{\rho}\tilde{v}_i k) = \frac{\partial}{\partial x_j}\left[\alpha_k(\mu + \mu_t)\frac{\partial k}{\partial x_j}\right] + G_k - \bar{\rho}\varepsilon - Y_M, \tag{A.4}$$

$$\frac{\partial}{\partial t}(\bar{\rho}\varepsilon) + \frac{\partial}{\partial x_i}(\bar{\rho}\tilde{v}_i \varepsilon) = \frac{\partial}{\partial x_j}\left[\alpha_\varepsilon(\mu + \mu_t)\frac{\partial \varepsilon}{\partial x_j}\right] + C_{1\varepsilon}\frac{\varepsilon}{k}G_k - C_{2\varepsilon}\bar{\rho}\frac{\varepsilon^2}{k} - R_\varepsilon, \tag{A.5}$$

where ε is the turbulence dissipation rate, G_k is the generation of turbulent kinetic energy arising from the mean velocity gradients, and Y_M is the contribution of the fluctuating dilatation in compressible turbulence to the overall dissipation rate. α_k and α_ε are inverse effective Prandtl numbers for the turbulent kinetic energy and its dissipation. R_ε is an additional term in the ε equation. $C_{1\varepsilon} = 1.42$, $C_{2\varepsilon} = 1.68$. Within the chemical reaction, the convection-diffusion equation governs the mass fraction of each species, Y_i [72]:

$$\frac{\partial}{\partial t}(\bar{\rho}Y_i) + \frac{\partial}{\partial x_j}(\bar{\rho}Y_i\tilde{v}_j) = \frac{\partial}{\partial x_j}(J_i) + R_i, \quad i = 1, \ldots, N-1, \tag{A.6}$$

where J_i is the diffusion flux of species i calculated by Maxwell-Stefan equations, R_i is the net rate of production of species i by chemical reaction, and N is the total number of species involved in the reaction. The energy conservation is represented by:

$$\frac{\partial}{\partial t}(\bar{\rho}H) + \frac{\partial}{\partial x_i}[\tilde{v}_i(\bar{\rho}H + \bar{p})] = \frac{\partial}{\partial x_j}\left[\alpha c_p(\mu + \mu_t)\frac{\partial T}{\partial x_j} + \tilde{v}_i(\mu + \mu_t)\left(\frac{\partial \tilde{v}_j}{\partial x_i} + \frac{\partial \tilde{v}_i}{\partial x_j} - \frac{2}{3}\delta_{ij}\frac{\partial \tilde{v}_l}{\partial x_l}\right) - \sum_{i=1}^{N} J_i H_i\right] + S_E, \tag{A.7}$$

where T is the temperature, H is the total enthalpy, and S_E is the source term.

The modeling of the particulate phase in the HVOF thermal spray is typically based on the Lagrangian approach. First, the average distance between individual particles in the HVOF thermal spray process can be estimated based on the analysis in the previous research works [68]. Specifically,

$$\frac{L_d}{d_p} = \left[\frac{\pi}{6}\frac{1+k}{k}\right]^{1/3}, \tag{A.8}$$

where L_d is the distance between two particles, d_p is particle diameter, and k is the particle/gas mass flow ratio divided by the particle/gas density ratio. Usually, the particle loading is about 4% and the density ratio is about 10^3 to 10^4, therefore L_d/d_p is about 20-50, which implied that the individual powder particles are isolated from each other[68,72]. Therefore, it is reasonable to assume that particle coagulation is negligible, and the powder size distribution does not change during the flight.

In typical HVOF thermal spray conditions, due to the supersonic flame and microparticles, the major force acting on a particle is the drag force, and other forces, such as gravitational force, thermophoresis force, etc., can be neglected. The motion of the particles is governed by Newton's law with the major drag force [6], which can be described as:

$$m_p \frac{dv_p}{dt} = \frac{1}{2} C_D \rho_g A_p (v_g - v_p)\left|v_g - v_p\right|, \tag{A.9}$$

where m_p and v_p are the mass and velocity of the particle, v_g and ρ_g are the velocity and density of the gas, A_p is the projected area of the particles on the plane perpendicular to the flow direction, and C_D is the drag coefficient representing the effect of the particle shape. With the assumption of negligible particle vaporization and heat transfer via radiation and oxidation, the energy equation for a single particle can be described as follows:

$$m_p c_{p_{\mathrm{p}}} \frac{dT_p}{dt} = hA'_p (T_g - T_p), \tag{A.10}$$

where m_p , T_p, A_p', and C_{pp} are the mass, temperature, surface area, and heat capacity of the particle, respectively. T_g is the temperature of the gas. The heat transfer coefficient h can be obtained by the Ranz-Marshall empirical equation [72].

Appendix 2 The full Set of Design Variables and Responses

Run	Coded Value					Particle (10 um WC-12CO) behavior		Equiv. ratio
	F	O	N	A	S	y_1 (Ptcl. Vel. (m/s))	y_2 (Ptcl. Temp.	
DP1	-1	-1	-1	-1	-1	575.492	1580.35	0.933
DP2	-1	-1	-1	-1	1	568.838	1519.04	0.933
DP3	-1	-1	-1	1	-1	581.464	1573.19	0.91
DP4	-1	-1	-1	1	1	576.441	1517.37	0.91
DP5	-1	-1	1	-1	-1	565.301	1482.1	0.933
DP6	-1	-1	1	-1	1	561.808	1437.23	0.933
DP7	-1	-1	1	1	-1	571.443	1472.55	0.91
DP8	-1	-1	1	1	1	568.35	1428.32	0.91
DP9	-1	1	-1	-1	-1	579.64	1621.14	0.88
DP10	-1	1	-1	-1	1	576.91	1538.03	0.88
DP11	-1	1	-1	1	-1	590.116	1569.96	0.859
DP12	-1	1	-1	1	1	585.741	1519.16	0.859
DP13	-1	1	1	-1	-1	571.887	1505.71	0.88
DP14	-1	1	1	-1	1	569.221	1416.93	0.88
DP15	-1	1	1	1	-1	580.123	1469.5	0.859
DP16	-1	1	1	1	1	576.271	1427.52	0.859
DP17	1	-1	-1	-1	-1	588.342	1551.3	1.238
DP18	1	-1	-1	-1	1	584.564	1501.46	1.238
DP19	1	-1	-1	1	-1	591.66	1533.71	1.207
DP20	1	-1	-1	1	1	588.504	1481.66	1.207
DP21	1	-1	1	-1	-1	584.65	1445.47	1.238
DP22	1	-1	1	-1	1	581.325	1404.17	1.238
DP23	1	-1	1	1	-1	582.546	1441.63	1.207
DP24	1	-1	1	1	1	579.207	1400.82	1.207
DP25	1	1	-1	-1	-1	607.875	1592.2	1.167
DP26	1	1	-1	-1	1	605.204	1545.41	1.167
DP27	1	1	-1	1	-1	608.647	1564.73	1.139
DP28	1	1	-1	1	1	605.753	1520.67	1.139
DP29	1	1	1	-1	-1	598.239	1502.06	1.167
DP30	1	1	1	-1	1	594.633	1455.71	1.167
DP31	1	1	1	1	-1	599.364	1477.68	1.139
DP32	1	1	1	1	1	596.318	1436.04	1.139
DP33	-	0	0	0	0	539.27	1403.19	0.694
DP34	2.3784	0	0	0	0	601.486	1470.91	1.387
DP35	0	-	0	0	0	566.102	1465.84	1.118
DP36	0	2.3784	0	0	0	609.031	1547.57	0.973
DP37	0	0	-	0	0	605.436	1679.27	1.041
DP38	0	0	2.3784	0	0	580.726	1426.99	1.041
DP39	0	0	0	-	0	581.277	1529.41	1.072
DP40	0	0	0	2.3784	0	593.917	1488.24	1.011
DP41	0	0	0	0	-2.3784	588.572	1553.4	1.041
DP42	0	0	0	0	2.3784	580.66	1431.7	1.041
DP43	0	0	0	0	0	589.776	1509.75	1.041
DP44	0	0	0	0	0	589.776	1509.75	1.041

Appendix 3 MATLAB code for discretizing the particle size distribution

```
clf
clear all
load('ParticleSize.mat');
intervno=30; % evenly divide the total length of the particle size into xx interval
stardia=ParticleSize(1); % stardia and endia are used for describing the length of the particle
enddia=ParticleSize(end-1);   % the unit here is um
interval=(enddia-stardia)/intervno; % the distance of each interval
interstar=zeros(intervno,1);
interstar(1)=stardia; % the starting point of the first interval is same as the starting point of the total length
interweight=zeros(intervno,1); % the volume weight of each interval
middia=zeros(intervno,1); % the diameter for representing each interval
countfreq=zeros(intervno,1); % a raw count number frequency of each interval
rescalfreq=zeros(intervno,1); % rescale the raw frequency so that the sum is 1
% Calculate distribution density
for i=1:intervno
   interweight(i)=myfun2(interstar(i)+interval)-myfun2(interstar(i)); % calculate the volume weight of each interval
   middia(i)=interstar(i)+0.95*interval;
   countfreq(i)=interweight(i)/((4/3)*pi*(middia(i)/2)^3);
```

```
    interstar(i+1)=interstar(i)+interval;

end

totalmass= ParticleSize(end); % total mass rate of the powder particle

intermass=totalmass*interweight; % mass rate per interval

% Scale frequency from 0 ~ 1

freqsum=sum(countfreq);

for i=1:intervno

    rescalfreq(i)=countfreq(i)/freqsum; % rescale the raw frequency so that the sum is 1

end

figure(1);

bar(middia,rescalfreq,1,'FaceColor',[1 1 1]);

xlabel('Particle diameter d_{i} (\mum)','FontSize',14,'FontName','Times New Roman');

ylabel('Count distribution n','FontSize',14,'FontName','Times New Roman');

set(gca,'FontSize',12);

% Compare cumulative plot

totalvol=0;

for i=1:intervno

    totalvol=totalvol+rescalfreq(i)*((4/3)*pi*(middia(i)/2)^3);

end

cumvol=zeros(intervno,1);

cumvolfrac=zeros(intervno,1);

for i=1:intervno

    cumvol(i+1)=cumvol(i)+rescalfreq(i)*((4/3)*pi*(middia(i)/2)^3);
```

```
    cumvolfrac(i)=cumvol(i+1)/totalvol;
end
experdiameter=stardia:0.0001:enddia;
expercumulative=myfun2(experdiameter);
dLaser=ParticleSize(1:end-1);
Rd=myfun2(dLaser);
figure(2);
plot(dLaser,Rd,'*','MarkerSize',10,'LineWidth',1.5);
hold on;
plot(middia,cumvolfrac,'o','MarkerSize',5);
hold on;
plot(experdiameter,expercumulative,'color','k','LineWidth',1.5);
xlim([5 50])
set(gca,'YTick',[0:0.1:1],'FontSize',12);
xlabel('Particle diameter d_{p} (\mum)','FontSize',14,'FontName','Times New Roman');
ylabel('Cumulative mass F_{mass}','FontSize',14,'FontName','Times New Roman');
legend({'Diameter by laser diffraction','Discretized particle group','Rosin-Rammler plot'},
'FontSize', 12, 'FontName','Times New Roman');
hold off;
% Estimate volume(mass) average diameter; dv_average is the estimated
% average
volfreq_sum=0;
for i=1:intervno
```

```
    % (4/3)*pi*(dv_average)^3=sum(rescalfreq*(4/3)*pi*(middia)^3)
    volfreq_sum=volfreq_sum+rescalfreq(i)*(4/3)*pi*(middia(i))^3;
end
% Assume the count number of minimal middia (countno(1)) is xx, then calculate the
% particle count number for each interval
countno=zeros(intervno,1);
countno(end)=1; % assume the count number of minimal middia is xx
for i=1:(intervno-1)
    countno(i)=round((countno(end)/rescalfreq(end))*rescalfreq(i));
end
countnomatrix=[middia,countno,intermass/2,rescalfreq];
save('countnomatrix.mat','countnomatrix');
figure(3);
bar(middia,countno);
dv_average=(volfreq_sum/((4/3)*pi))^(1/3) % mass(volume) averaging
function y=myfun2(x)
y=1-exp(-(x/33.1873).^4.9532); % Gaussian distribution of the particle size
end
```

Appendix 4 MATLAB code for automatically carrying out the coating thickness simulation

```
%% Particle group generation
clear all
load('countnomatrix.mat');
countnomatrix(:,3)=countnomatrix(:,3)*10^6;
for i=1:size(countnomatrix,1)
filename = sprintf('particlefile%d',i);
fid_write = fopen(filename,'w+');
fprintf(fid_write,'((injection-%d ((type . inert) (injection-type . surface) (cone-type . solid-cone) (numpts . 2) (dpm-fname . " ") (surfaces 35) (boundary -1) (stochastic-on . #t) (random-eddy-on . #f) (ntries . 2) (time-scale-constant . 0.15) (cloud-on . #f) (cloud-min-dia . 0.) (cloud-max-dia . 100000.) (material . wc-12co) (scale-by-area . #t) (use-face-normal . #t) (random-surface? . #f) (devolatilizing-species . #f) (evaporating-species . #f) (oxidizing-species . #f) (product-species . #f) (rr-distrib . #f) (rr-uniform-ln-d . #f) (evaporating-liquid-on . #f) (evaporating-material . #f) (liquid-fraction . 0.) (dpm-domain . none) (collision-partner . *dem-unknown*) (multiple-surface) (parcel-number . 500) (parcel-mass . 1e-09) (parcel-diameter . 1e-05) (parcel-model . 0) (drag-law . "spherical") (shape-factor . 1.) (cunningham-correction . 1.) (drag-fcn . "none") (brownian-motion . #f) (seco-breakup-on? . #t) (seco-breakup-tab? . #t) (seco-breakup-wave? . #f) (seco-breakup-khrt? . #f) (seco-breakup-ssd? . #f) (seco-breakup-madabhushi? . #f) (seco-breakup-tab-y0 . 0.) (number-tab-diameters . 2) (seco-breakup-wave-b1 . 1.73) (seco-breakup-wave-b0 . 0.61) (seco-breakup-khrt-cl . 5.7) (seco-breakup-khrt-ctau . 0.5) (seco-breakup-khrt-crt . 1.) (seco-breakup-ssd-we-cr . 6.) (seco-breakup-ssd-core-bu . 1.73) (seco-breakup-ssd-np-target . 1000.) (seco-
```

```
breakup-ssd-x-si . -0.1) (seco-breakup-madabhushi-jet-diameter . 0.001) (laws (law-1 . "Inert Heating") (law-2 . "Inactive") (law-3 . "Inactive") (law-4 . "Inactive") (law-5 . "Inactive") (law-6 . "Inactive") (law-7 . "Inactive") (law-8 . "Inactive") (law-9 . "Inactive") (law-10 . "Inactive") (switch . "Default")) (udf-inject-init . "none") (udf-heat-mass . none) (components) (volume-specification . zone) (volume-zones) (volume-bounding-shape circle 0 0 0 0 . 0) (volume-streams-spec . total-parcel-count) (volume-streams-total . 100) (volume-streams-per-cell . 2) (mass-input-on . #f) (rotation-on? . #f) (rot-drag-law . "none") (rot-lift-law . "none") (cone-type . "solid-cone") (uniform-mass-dist-on? . #f) (spatial-staggering/std-inj/on? . #f) (spatial-staggering/atomizer/on? . #t) (stagger-radius . 0.) (rough-wall-on? . #f) (cphase-domain . none) (x-pos . 0.) (x-pos2 . 0.) (y-pos . 0.) (y-pos2 . 0.) (z-pos . 0.) (z-pos2 . 0.) (ff-center-x . 0.) (ff-center-y . 0.) (ff-center-z . 0.) (ff-virtual-origin-x . 0.) (ff-virtual-origin-y . 0.) (ff-virtual-origin-z . 1.) (ff-normal-x . 1.) (ff-normal-y . 0.) (ff-normal-z . 0.) (x-vel . 0.) (x-vel2 . 0.) (y-vel . 0.) (y-vel2 . 0.) (z-vel . 0.) (z-vel2 . 0.) (x-ang-vel . 0.) (x-ang-vel2 . 0.) (y-ang-vel . 0.) (y-ang-vel2 . 0.) (z-ang-vel . 0.) (z-ang-vel2 . 0.) (atomizer-x-axis . 0.) (atomizer-y-axis . 0.) (atomizer-z-axis . 1.) (diameter . %fe-6) (diameter2 . 1e-06) (temperature . 300.) (temperature2 . 300.) (flow-rate . 1e-20) (flow-rate2 . 1e-20) (unsteady-start . 0.) (unsteady-stop . 0.) (unsteady-ca-start . 0.) (unsteady-ca-stop . 0.) (vapor-pressure . 10000.) (inner-diameter . 0.001) (outer-diameter . 0.005) (half-angle . 0.34906585) (plain-length . 0.001) (plain-corner-size . 1e-05) (plain-const-a . 4.9) (pswirl-inj-press . 1000000.) (airbl-rel-vel . 100.) (effer-quality . 0.08500000000000001) (effer-t-sat . 373.) (ff-orifice-width . 0.001) (phi-start . 0.) (phi-stop . 6.28318531) (sheet-const . 12.) (lig-const . 0.5) (effer-const . 0.33) (effer-half-angle-max . 0.261799388) (ff-sheet-const . 3.) (atomizer-disp-angle . 6.) (x-axis . 0.) (y-axis . 0.) (z-axis . 1.) (vel-mag . 0.01) (ang-vel-mag . 0.) (cone-angle . 0.) (inner-radius . 0.) (radius . 0.) (swirl-frac . 0.) (total-flow-rate . %fe-06) (total-mass . 1e-20) (rr-min . 1e-06) (rr-max . 0.0001) (rr-mean . 1e-
```

```
05) (rr-spread . 3.5) (rr-numdia . 10.) (x-posr . 0.) (y-posr . 0.) (z-posr . 0.) (x-posu . 0.) (y-posu .
0.) (z-posu . 0.))))', i,countnomatrix(i,1),countnomatrix(i,3));
fclose(fid_write);
end
%% fluent injection journal file generation
folderno=24;
particleno=30;
filename = sprintf('readinjection');
fid_write = fopen(filename,'w+');
fprintf(fid_write,'/file/set-tui-version "18.2"\n');
fprintf(fid_write,'(cx-gui-do cx-set-list-tree-selections "NavigationPane*List_Tree1" (list
"Setup|Models|Discrete Phase (Off)|Injections"))\n');
fprintf(fid_write,'(cx-gui-do cx-list-tree-right-click "NavigationPane*List_Tree1" )\n');
fprintf(fid_write,'(cx-gui-do cx-activate-item "MenuBar*PopupMenuTree-
Injections*Import...")\n');
fprintf(fid_write,'(cx-gui-do cx-set-file-dialog-entries "Select File"
"( "E:/Dropbox/PhD_Jiangzhuo Ren/Journal #3/Matlab/Single coating thickness
distribution/Particleinjection/%d/particlefile1") "Injection Files ()")\n',folderno);
for i=2:particleno
    fprintf(fid_write,'(cx-gui-do cx-set-list-tree-selections "NavigationPane*List_Tree1" (list
"Setup|Models|Discrete Phase (Off)|Injections"))\n');
    fprintf(fid_write,'(cx-gui-do cx-list-tree-right-click "NavigationPane*List_Tree1" )\n');
```

```
    fprintf(fid_write,'(cx-gui-do cx-activate-item "MenuBar*PopupMenuTree-Injections*Import...")\n');
    fprintf(fid_write,'(cx-gui-do cx-set-file-dialog-entries "Select File" "( "particlefile%d") "Injection Files ()")\n',i);
end
fprintf(fid_write,'(cx-gui-do cx-activate-item "MenuBar*WriteSubMenu*Stop Journal")\n');
fclose(fid_write);
```

Appendix 5 Pseudocode for the User-defined Boundary Condition

Algorithm: accumulative heat flux calculation with respect to nozzle trajectory, flame behavior, and thermal analysis between the coating layer and the substrate main()

```
Inputs:
    a1,b1,a2,b2,a3,b3                      heat flux function coefficients
    t                                      time sequence for the trajectory
    File "Trajectory"                      file contains position(x,y,z) and time(t) for the nozzle end
    t_step                                 fluent time step length
    fluxdur                                dissipation duration of heat flux by particle
    FILE "particle_heat_flux_Cof"          file contains particle heat flux coefficients
    PcofN                                  required particle coefficient numbers
    FILE "Cofile"                          file contains flame heat flux coefficients
    flow-time                              current dynamic flow time in ANSYS Fluent
    Nt_number                              number of points in the heat effect zone
    F_CENTROID(pos,f,t)                    current mesh element centroid position and time
#Define heat flux functions func1, func2, func3
    func1(a1,b1,t)=a1*exp(b1*t)
    func2(a2,b2,t)=a2*t+b2
    func3(a3,b3,t)=exp(b3*t)
#Get number of trajectory points
    initialize counter to 0
    open File "Trajectory"
```

```
  do while file ”Trajectory” has data
     add 1 to counter
     scan the next datum of the file
  end do
  close File “Trajectory”
  set variable trano to counter/4         #each point has 4 data, position(x,y,z) and time(t)
#Get particle flux iteration number
  set flutime to t_step                    #input fluent time step
  set PfluxDur to fluxdur                  #input dissipation duration of heat flux by particle
  set PfluIter to floor(PluxDur/flutime)   #round down (PluxDur/flutime) as flux iteration number
#Initilization of calculation variables
  initialize position pointer *xa,*ya,*za and time pointer *t  to NULL
  initialize heat flux function coefficient number pointer *c1,*c2,*c3 to NULL
  initialize effect zone pointers of position, radius, time, and heat flux to NULL
#Preprocessing, allocating dynamic memory to variables
  set xa, ya, za , ta memory space sized float*trano respectively
  set c1,c2,c3 memory space sized float*trano respectively
  set EffectZone_x, EffectZone_y, EffectZone_z, EffectZone_r, EffectZone_t, EffectZone_Heatflux
memory space sized float*PfluIter respectively
#Initialize x position as the original position
  while the x counter is less than PfluIter
     set current x position to -0.2        #The initial point’s position is (-0.2,0,0)
     add 1 to x counter
```

```
  end
#Read and store required particle heat flux coefficients
  initialize an array Pcof with the length of PcofN
  open File “particle_heat_flux_Cof”
  while Pcof counter is less than PcofN
    scan a datum from the file and store it to the current position of Pcof
    add 1 to Pcof
  end
  close File ”particle_heat_flux_Cof”
#Read and extract flame heat flux coefficients
  #Count number of coefficients
    set number counter to 0
    open File “Cofile”
    do while File “Cofile” has data
      add 1 to counter
      scan the next datum of the file
    end do
    close File “Cofile”
  #extract coefficients to three groups of Gussian term coefficients a,b, and c
    set cofno to counter/3
    initialize 3 arrays, a[cofno], b[cofno], c[cofno] to zero
    set coefficient number counter l to 0
    while l is less than cofno
```

```
    set group identifier m to 0
   while m is less than 3
       scan a datum (data) from the file
       if m equals to 0
           set a[l] to data
       if m equals to 1
           set b[l] to data
       if m equals to 2
           set c[l] to data
       add 1 to m
    end
  end
#Define heat flux and load as a boundary condition
  #Linear interpolation of the current position and time based on trajectory and flow time
    set ftime to flow-time
    while time counter k is less than trano-1 and current trajectory time ta is less than ftime
      set ft to (ftime-ta[k-1])/(ta[k]-ta[k-1])             #linear interpolation of current time
      set x_source to xa[k-1]+ft*(xa[k]-xa[k-1])         #linear interpolation of current x position
      set y_source to ya[k-1]+ft*(ya[k]-ya[k-1])         #linear interpolation of current y position
        set z_source to za[k-1]+ft*(za[k]-za[k-1])        #linear interpolation of current z position
        add 1 to k
    end
  #Dynamically update the effect zone position and time
```

```
  initialize time index number Nt_index to 0
  while Nt_index is less than Nt_number
    set EffectZone_x[Nt_index] to x_source
    set EffectZone_y[Nt_index] to y_source
    set EffectZone_z[Nt_index] to z_source
    set EffectZone_t[Nt_index] to ftime
    if Nt_index equals to (Nt_number-1)
      set Nt_index to 0            #A new round of Effect Zone update begins
    add 1 to Nt_index
  end
#Calculate accumulative flame heat flux
  begin_f_loop(f,t)            #begin the dynamic loop of mesh element and time
  F_CENTROID(pos,f,t)       #extract current centroid position and time of the mesh element
  set r to sqrt(pow((pos[0] - x_source), 2) + pow((pos[1] - y_source), 2) + pow((pos[2] - z_source), 2))           #Calculate the radius of the current mesh element centroid to source
  set flame heat flux coefficient counter j to 0
  set accumulative flame heat flux (Flame_heat_flux) to 0
  while j is less than cofno
    set FlameGaussian to (a[j])* exp(-(pow(((r - (b[j])) / c[j]), 2)))           #calculate current flame gaussian term
    add FlameGaussian to Flame_heat_flux                  #Add current term to the accumulative flame heat flux
  end
```

```
  #Calculate accumulative particle heat flux
    set particle heat flux iteration number m to 0
    set accumulative particle heat flux (Particle_heat_flux) to 0
    while m is less than PfluIter
      set c1[m] to func1(PCof[0], PCof[1], ftime - EffectZone_t[m])    #calculate coefficient c1
      set c2[m] to func2(PCof[2], PCof[3], ftime - EffectZone_t[m])    #calculate coefficient c2
      set c3[m] to func3(PCof[4], PCof[5], ftime - EffectZone_t[m])    #calculate coefficient c3
      set effect zone radius (EffectZone_r[m]) to sqrt(pow((pos[0] - EffectZone_x[m]), 2) + pow((pos[1] - EffectZone_y[m]), 2) + pow((pos[2] - EffectZone_z[m]), 2))  #calculate effect radius
      if EffectZone_r[m] is less than threshold 0.006m
        set effect zone heat flux Gaussian term(EffectZone_Heatflux[m]) to c1[m]*pow(EffectZone_r[m], 2) + c2[m] * EffectZone_r[m] + c3[m]    #calculate effect heat flux
      else
        set effect zone heat flux Gaussian term(EffectZone_Heatflux[m]) to 0    # if the distance is so far away, the heat flux will be neglected
    Add EffectZone_Heatflux[m] to Particle_heat_flux    #Add current term to the accumulative particle heat flux
    Add 1 to m
    end
#Calculate the accumulative heat flux in total (Flame+Particle)
     FPROFILE(f,t,i)=Flame_heat_flux+Particle_heat_flux    #set the boundary condition as the total accumulative heat flux
```

```
end_f_loop(f, t)        #end the dynamic loop of mesh element and time
```